REVIEW

Molecular reactivity of thiolate-protected noble metal nanoclusters: synthesis, self-assembly, and applications

Qiaofeng Yao, [ID] [a] Zhennan Wu,[a] Zhihe Liu,[ac] Yingzheng Lin,[ac] Xun Yuan [ID] *[b] and Jianping Xie [ID] *[ac]

Thiolate-protected noble metal (*e.g.*, Au and Ag) nanoclusters (NCs) are ultra-small particles with a core size of less than 3 nm. Due to the strong quantum confinement effects and diverse atomic packing modes in this ultra-small size regime, noble metal NCs exhibit numerous molecule-like optical, magnetic, and electronic properties, making them an emerging family of "metallic molecules". Based on such molecule-like structures and properties, an individual noble metal NC behaves as a molecular entity in many chemical reactions, and exhibits structurally sensitive molecular reactivity to various ions, molecules, and other metal NCs. Although this molecular reactivity determines the application of NCs in various fields such as sensors, biomedicine, and catalysis, there is still a lack of systematic summary of the molecular interaction/reaction fundamentals of noble metal NCs at the molecular and atomic levels in the current literature. Here, we discuss the latest progress in understanding and exploiting the molecular interactions/reactions of noble metal NCs in their synthesis, self-assembly and application scenarios, based on the typical M(0)@M(ɪ)−SR core−shell structure scheme, where M and SR are the metal atom and thiolate ligand, respectively. In particular, the continuous development of synthesis and characterization techniques has enabled noble metal NCs to be produced with molecular purity and atomically precise structural resolution. Such molecular purity and atomically precise structure, coupled with the great help of theoretical calculations, have revealed the active sites in various structural hierarchies of noble metal NCs (*e.g.*, M(0) core, M−S interface, and SR ligand) for their molecular interactions/reactions. The anatomy of such molecular interactions/reactions of noble metal NCs in synthesis, self-assembly, and applications (*e.g.*, sensors, biomedicine, and catalysis) constitutes another center of our discussion. The basis

[a]*Department of Chemical and Biomolecular Engineering, National University of Singapore, 4 Engineering Drive 4, Singapore 117585. E-mail: chexiej@nus.edu.sg*

[b]*College of Materials Science and Engineering, Qingdao University of Science and Technology, Qingdao, China 266042. E-mail: yuanxun@qust.edu.cn*

[c]*Joint School of National University of Singapore and Tianjin University, International Campus of Tianjin University, Binhai New City, Fuzhou, China 350207*

Qiaofeng Yao received his B.S. (2010) from the University of Science and Technology of China (USTC). He then earned his Ph.D. (2015) from the National University of Singapore (NUS), under the co-supervision of Prof. Jim Yang Lee and Prof. Jianping Xie. He is currently working as a research fellow with Prof. Jianping Xie at NUS. His current research interest focuses on developing total synthesis and self-assembly chemistry for atomically precise metal nanoclusters.

Zhennan Wu obtained his Ph.D. degree (2016) from the State Key Laboratory of Supramolecular Structure and Materials at Jilin University under the supervision of Prof. Hao Zhang. Thereafter, he joined the team of Prof. Osman M. Bakr in King Abdullah University of Science and Technology (KAUST) for post-doctoral research and has been working as a research fellow with Prof. Jianping Xie in NUS since 2018. His research interests are centered on the self-assembly chemistry and optical physics of ultrasmall metal nanoclusters.

and practicality of the molecular interactions/reactions of noble metal NCs exemplified in this *Review* may increase the acceptance of metal NCs in various fields.

1. Introduction

With the development of nanochemistry towards atomic precision, thiolate-protected noble metal (*e.g.*, Au and Ag) nanoclusters (NCs) have attracted great interest due to their atomically tunable structures and properties.[1–7] Thiolate-protected metal nanoclusters (NCs) are an emerging family of ultra-small particles (<3 nm) composed of several to several hundred metal atoms.[3–5,8] They can be well described by the molecular formula $[M_n(SR)_m]^q$, where n, m and q are the number of metal atoms (M = Au or Ag) and thiolate ligands (SR), and net charge, respectively. The remarkable achievements of X-ray crystallography in the past two decades suggest a universal core–shell structure scheme for $[M_n(SR)_m]^q$ NCs, in which an M(0) core is capped by a monolayer of M(I)–SR protecting motifs.[9–18] Based on this molecule-like structure and the strong quantum confinement effects in this ultra-small size regime, metal NCs exhibit many molecule-like properties, such as

HOMO–LUMO transition,[10,12,13,19] strong luminescence,[20–23] intrinsic chirality,[24] and good catalytic activity.[5,25–27] More intriguingly, almost all these molecule-like properties show an atomic-level dependency on the cluster structure. Such structural dependency not only provides a good means to diversify cluster properties for practical applications in various fields (*e.g.*, biomedicine,[28–34] green energy,[35–37] and catalysis),[38–41] but also offers an ideal platform for revealing the structure–property relationship of metal-based nanomaterials at the atomic level.[40,42,43]

In the past few decades, the development of synthetic chemistry has allowed atomically precise $[M_n(SR)_m]^q$ NCs to be widely used by the community as high-quality "metallic molecules", thus motivating various further developments of metal NCs such as self-assembly and practical application.[7,8] In these developments, an individual metal NC behaves like a molecular entity, and its practicality is inherently determined by its molecular interactions/reactions with ions, molecules, and other NCs. For example, extensive experimental and theoretical

Zhihe Liu received his B.S. (2015) from China University of Geosciences (CUG). Then, he obtained his M.S. (2018) from State Key Lab of Crystal Materials, Shandong University of China (SDU) under the supervision of Prof. Hong Liu. He is currently a Ph.D. student under the supervision of Prof. Jianping Xie at NUS. His research interest is in the development of conductive metal nanoclusters and their self-assembly in electrochemical applications.

Xun Yuan received his B.E. (2006) and M.E. (2009) degrees from Shandong University of Technology, China, and Ph.D. degree (2014) from NUS under the supervision of Prof. Jianping Xie. After 3 years of postdoctoral work at the Institute of Bioengineering and Nanotechnology (IBN), he joined Qingdao University of Science and Technology (QUST) as a professor in 2017. His research focuses on the synthesis and applications of metal nanoclusters.

Yingzheng Lin received her B.S. degree (2016) from Sun Yat-sen University, China, and M.E. degree (2019) from the Institute of Urban Environment, Chinese Academy of Sciences, China. After that, she joined Prof. Jianping Xie's group as a PhD student at the Department of Chemical and Biomolecular Engineering, NUS. She is interested in engineering metal nanoclusters for environmental applications.

Jianping Xie is currently a Dean's Chair Associate Professor at the Department of Chemical & Biomolecular Engineering, NUS. He received his B.S. and M.S. in Chemical Engineering from Tsinghua University, China, and his Ph.D. from the Singapore MIT Alliance (SMA) program. He joined NUS in 2010 and established the BioNanoMetals research group. His group is known for their work on engineering ultrasmall metal nanoclusters for biomedical and catalytic applications. His research interests include noble metal nanoclusters, nanomedicine, and cluster catalysis.

explorations have shown that the adsorption and subsequent activation of O_2 on the surface of metal NCs is crucial in the aerobic oxidation reaction catalysed by metal NCs,[40,43] and the development of sensors is highly dependent on chemical adsorption or reaction of analytes with metal NCs.[44–47] Recent mechanistic discoveries also suggest that the growth and functionalization of metal NCs depends on their molecular interactions/reactions with reactive molecular species, including reducing agents,[48–51] metal salts,[52,53] SR ligands,[54–57] M(I)–SR/M(II)–SR complexes,[58–62] and metal NCs.[63,64] Moreover, continuous developments in mass spectrometry, X-ray crystallography, X-ray absorption fine structure (XAFS) analysis, and theoretical simulations of noble metal NCs have enabled researchers to understand the pathways and dynamics of the above-mentioned reactions/interactions at the unprecedented molecular and atomic levels.[8,65–72]

Although in the past two decades, great efforts have been witnessed to establish the interaction/reaction chemistry of metal NCs, there is a lack of systematic summary and discussion on this topic in the current literature. Therefore, in this *Review*, we aim at discussing the latest developments in the basis and practicality of the molecular interactions/reactions between metal NCs and ions, molecules, and other NCs at the molecular and atomic levels. The discussion will be based on the aforementioned M(0)@M(I)–SR core–shell structure of metal NCs. The *Review* will start with a brief summary of the basic principles of molecular interactions/reactions between metal NCs and ions, molecules, and other NCs, focusing on the active sites of metal NCs for such interactions/reactions. Based on these fundamental insights, the use of molecular interactions/reactions of metal NCs in the synthetic chemistry (including bottom-up growth, alloying, and ligand exchange reactions) and post-synthesis development of metal NCs (including self-assembly, sensing, biomedical, and catalytic explorations) will be discussed in the following sections. This *Review* will be concluded with a concise summary of the main findings discussed above and our perspectives on the future development of interaction/reaction chemistry of noble metal NCs.

2. Molecular interaction/reaction fundamentals of metal NCs

The research on thiolate-protected noble metal NCs can be traced back to the 1990s, when pioneers worked together to establish the primary methods for the synthesis and characterization of sub-3 nm metal nanoparticles and NCs.[73–77] These metal NCs have shown additional charm since the first successful attempt in resolving their crystal structure by X-ray crystallography in 2007, where a racemic mixture of $Au_{102}(SR)_{44}$ was identified by Jadzinsky et al.[9] Another milestone achievement was then made independently by Heaven et al.[11] and Zhu et al.[10] in 2008, where the crystal structure of $[Au_{25}(SR)_{18}]^-$ was resolved. Such success in structure determination of Au NCs at the atomic resolution has also been propagated to Ag NCs, although Ag(0) is more susceptible to

oxidation than Au(0). For example, the crystal structure of $[Ag_{44}(SR)_{30}]^{4-}$ has been revealed separately by Desireddy et al.[12] and Yang et al.[13] in 2013, while a silver analogue of $[Au_{25}(SR)_{18}]^-$, i.e., $[Ag_{25}(SR)_{18}]^-$, was synthesized and structurally analysed by X-ray crystallography by Joshi et al. in 2015.[14] Based on the accumulated successes in the crystallization and structure determination of Au and Ag NCs, the crystal structures of numerous Au- or Ag-based alloy NCs have also been resolved with various heteroatoms of Au,[13,78] Ag,[79,80] Cu,[17,81] Pt,[82,83] Pd,[83,84] Hg,[85] and Cd.[53,58]

With the increasing accessibility to the crystal structures of metal NCs with various sizes, compositions, and spatial arrangements of metal atoms or SR ligands, it has become increasingly known that the expanding structural library of thiolate-protected noble metal NCs can be in general described by a core–shell scheme, in which the M(0) core is protected by a monolayer of M(I)–SR protecting motifs.[18] For example, $[Au_{25}(SR)_{18}]^-$ features a centred icosahedral Au_{13} core, which is further wrapped by six dimeric SR–$[Au(I)–SR]_2$ motifs,[10,11] while $Au_{38}(SR)_{24}$ possesses a bi-icosahedral Au_{23} core protected by three monomeric SR–Au(I)–SR motifs and six dimeric SR–$[Au(I)–SR]_2$ motifs.[86] It should be mentioned that such M(0)@M(I)–SR core–shell structural scheme remains valid even when the cluster size approaches the threshold value defining the molecular–metallic transition of metal nanomaterials. Recent transient and steady-state absorption spectroscopy analysis has identified $Au_{246}(SR)_{80}$ as the hitherto largest NC with a discrete and thus non-metallic electronic structure.[87,88] The X-ray crystallography analysis indicates that $Au_{246}(SR)_{80}$ has an Ino-decahedron-based Au_{206} core.[15] Depending on the varying
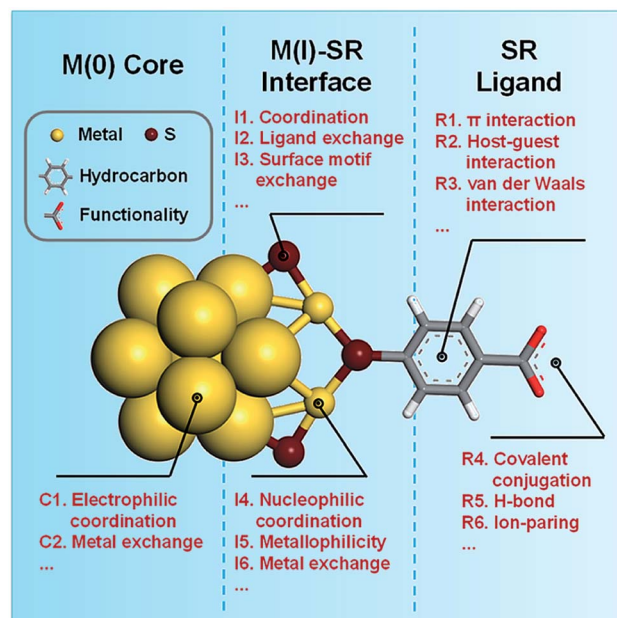

Fig. 1 Schematic illustration of the active sites of noble metal NCs for their interactions/reactions with ions, molecules, and other NCs. The crystal structure of $[Au_{25}(SR)_{18}]^-$ (SR = thiolate ligand) was redrawn as a demonstrative example based on the reported crystallography data,[10] in which only one SR–$[Au(I)–SR]_2$ motif is shown for clarity.

curvature on this huge Au_{206} core, $Au_{246}(SR)_{80}$ possesses diverse terminal SR ligands, monomeric SR–Au(I)–SR motifs, and dimeric SR–[Au(I)–SR]$_2$ motifs in its protecting shell. More interestingly, the mutual fit scheme of the Au(0) core and Au(I)–SR motifs not only leads to a high packing symmetry of the Au(0) core, but also results in an ordered arrangement pattern of SR ligands on the cluster surface, ultimately producing a structural complexity similar to that of proteins. The hierarchical protein-like structure of noble metal NCs indeed provides diverse active sites for their interactions/reactions with ions, molecules, and other NCs.[7] Therefore, the molecular interactions/reactions of metal NCs will be summarized in terms of their active sites deciphered based on the M(0)@M(I)–SR core–shell structural scheme, as illustrated in Fig. 1.

2.1. Molecular interactions/reactions based on the M(0) core

One of the most significant structural features of metal NCs is the diverse packing modes of their M(0) core, including icosahedron,[10–14] decahedron,[9] face-centred cubic (FCC),[89] and hexagonal close packed (HCP)[90] modes. The diverse structures of the M(0) core not only induce molecule-like electronic properties, but also provide various types of coordination-unsaturated M(0) sites for chemical or physical adsorption. In particular, due to the delocalization of valence electrons in the M(0) core, the M(0) core usually exhibits an electron-rich (electropositive) feature, which enhances its affinity to elements with high electronegativity (entry C1, Fig. 1). As a demonstrative example, $[Au_{25}(SR)_{18}]^-$ has a valence electron count of eight ($N = n - m - q = 25 - 18 - 1 = 8$), and these valence electrons are distributed in its Au_{13} core.[10] The electron-rich Au_{13} core adopts a centred-icosahedral morphology, in which twelve facets are capped by six dimeric SR–[Au(I)–SR]$_2$ motifs. This leaves eight uncapped triangular Au_3, which have been documented as active sites for activating the –C=O bond in the catalytic hydrogenation of ketones.[91,92] For example, Zhu et al. recorded

a nearly 100% stereo-selectivity of $Au_{25}(SR)_{18}$ toward the hydrogenation of bicyclic ketone 7-(phenylmethyl)-3-oxa-7-azabicyclo[3.3.1]nonan-9-one, exclusively producing the bicyclic alcohol with the as-formed –OH group adopting an equatorial orientation relative to the N-containing six-member ring (Fig. 2a).[91] The authors attributed this remarkable stereo-selectivity to the preferential coordination of –C=O with the electron-rich Au_{13} core of $Au_{25}(SR)_{18}$ NCs, followed by a partial electron transfer from the Au_{13} core to the O atom which activates the –C=O bond. A similar –C=O bond activation mechanism was also used to achieve 100% chemo-selectivity toward α,β-unsaturated alcohols in the hydrogenation reaction of α,β-unsaturated ketones or aldehydes catalysed by $[Au_{25}(SR)_{18}]^-$.[92]

In addition to ketones and aldehydes, the M(0) core of metal NCs may also exhibit reaction/interaction activity toward gas molecules such as CO and O_2. The exploration of the reactivity of atomically precise metal NCs toward O_2 was pioneered by Zhu et al. The authors reported the aerobic oxidation of the anionic $[Au_{25}(SR)_{18}]^-$ into the charge-neutral $Au_{25}(SR)_{18}$.[93] Based on the atomically precise structures revealed by X-ray crystallography or theoretical prediction, Lopez-Acevedo et al. carried out systematic density functional theory (DFT) calculations on a series of Au NCs (e.g., $Au_{11}(PH_3)_7Cl_3$, $[Au_{25}(SR)_{18}]^-$, $[Au_{39}(PH_3)_{14}Cl_6]^-$, $Au_{102}(SR)_{44}$, and $Au_{144}(SR)_{60}$, where PH_3 denotes phosphine), and studied the activation process of O_2 on Au NCs in a typical aerobic oxidation reaction of CO.[43] The authors found that after partial removal of the Cl ligands or Au(I)–SR motifs, the affinity (approximated by the binding energy) of these NCs with O_2 is different, which largely depends on their HOMO–LUMO gaps. As shown in Fig. 2b, removing one dimeric SR–[Au(I)–SR]$_2$ motif from the surface of $[Au_{25}(SR)_{18}]^-$ can not only return one valence electron to the Au_{13} core, but also create an open site on the Au_{13} core for O_2 adsorption. The additional valence electron occupies an electron state over the HOMO–LUMO gap of $[Au_{25}(SR)_{18}]^-$. The electron transferred
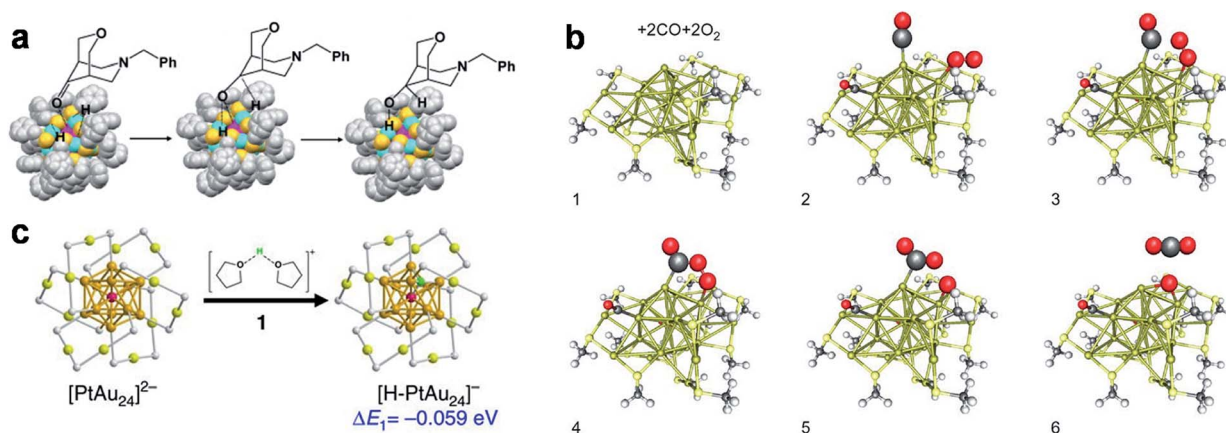

Fig. 2 Schematic illustration of adsorption and activation of (a) –C=O, (b) O_2, and (c) solvated H^+ on the Au_{13} core of $[Au_{25}(SR)_{18}]^-$ (a, b) or $Au_{12}Pt$ core of $[Au_{24}Pt(SR)_{18}]^{2-}$ (c). SR in (a) is –S-C_2H_4Ph (colour code: pink, core Au(0); blue, motif Au(I); golden, S; grey, C). SR in (b) is –S-CH_3; two SR–[Au(I)–SR]$_2$ motifs are removed for co-adsorption of O_2 and CO (colour code: golden, Au; yellow, S; grey, C; light grey, H; red, O). The solvent molecules in (c) are tetrahydrofuran (THF) (colour code: golden, Au; red, Pt; yellow, S; green, H; light grey, C). (a) is reproduced with permission from ref. 91. Copyright 2010, Elsevier. (b) is reproduced with permission from ref. 43. Copyright 2010, Springer Nature. (c) is reproduced with permission from ref. 97. Copyright 2017, the Authors, published by Springer Nature.

from such an electron state to one of the $2\pi^*$ orbitals of O_2 can activate O_2 to superoxo O_2^-. By removing another SR–[Au(I)–SR]$_2$ motif close to the superoxo species, a core Au site can be made available for CO adsorption. The subsequent reaction between the adsorbed CO and superoxo species provides a plausible mechanism for the aerobic oxidation of CO. In addition to the core Au site exposed by partial removal of M(I)–SR protecting motifs, the originally uncapped triangular Au$_3$ may also be the active site of [Au$_{25}$(SR)$_{18}$]$^-$ for CO and O$_2$ activation. In a recent contribution from Liu et al.,[94] a triangular Au$_3$ based self-promoting mechanism was proposed for the aerobic oxidation of CO, in which the co-adsorption of two CO and one O$_2$ on an open triangular Au$_3$ can facilitate the cleavage of O–O bonds conducive to the simultaneous formation of two CO$_2$.

In addition to partially removing SR ligands or M(I)–SR ligands, the molecular reactivity of the M(0) core can also be improved by doping heteroatoms in the M(0) core. Doping Au(0) or Ag(0) cores with heteroatoms has long been employed as an effective means to enhance the stability and catalytic activity of metal NC-based catalysts.[95,96] The heteroatoms usually have two functions: (1) manipulate the electronic structure of NCs, and (2) introduce additional active sites to chemically or physically adsorb substrate molecules. For example, Kwak et al. compared the electronic structure and electrocatalytic performance of [Au$_{25}$(S-C$_6$H$_{13}$)$_{18}$]$^-$ and Au$_{24}$Pt(S-C$_6$H$_{13}$)$_{18}$ through optical spectroscopy and voltammetry, where HS-C$_6$H$_{13}$ denotes 1-hexanethiol.[97] They concluded that embedding the dopant Pt in the centre of the icosahedral M$_{13}$ core would induce significant changes in the electron energy diagram and the redox potential of M$_{25}$(SR)$_{18}$ NCs. The superior electrocatalytic activity of Au$_{24}$Pt(SR)$_{18}$ for the hydrogen evolution reaction (HER) in tetrahydrofuran (THF) is attributed to the well-matched redox potential of [Au$_{24}$Pt(SR)$_{18}$]$^{-/2-}$ and the onset potential of the HER, indicating that Au$_{24}$Pt(SR)$_{18}$ can act as a charge-state-dependent electron mediator in the HER. The detailed DFT calculations by these authors further revealed that another equally important contributor to the enhanced HER catalytic activity is the preferential adsorption of H on the Pt heteroatom (Fig. 2c), although the Pt heteroatom is located at the centre of the icosahedral M$_{13}$ core. In a follow-up study, the authors found that the HER catalytic activity of Au$_{24}$Pt(SR)$_{18}$ can be further enhanced by incorporating a proton-relaying ligand (e.g., 3-mercapto-1-propanesulfonic acid) into its protecting shell.[98] It should be noted that in many other catalytic reaction systems, including oxidation[99] and C–C coupling[100] reactions, similar doping effects of M(0) have also been recorded.

In addition to the electropositive coordination sites, the M(0) core can also be the active site for the metal exchange reactions (entry C2, Fig. 1). For example, Wang et al. employed [Au$_{25}$(SR)$_{18}$]$^-$ as a template NC for the metal exchange reaction with Cu(I)–SR, Ag(I)–SR, Cd(II)–SR, and Hg(II)–SR complexes in toluene, generating [Au$_{25-x}$Cu$_x$(SR)$_{18}$]$^-$ (x = 0–2), [Au$_{25-x}$Ag$_x$(SR)$_{18}$]$^-$ (x = 0–4), Au$_{24}$Cd(SR)$_{18}$, and Au$_{24}$Hg(SR)$_{18}$, respectively.[58] The X-ray crystallography and DFT calculation from the same authors and other groups[53,79] revealed that such metal exchange reactions do not change the M$_{25}$S$_{18}$ framework of [Au$_{25}$(SR)$_{18}$]$^-$, in which the Cu, Ag, and Cd heteroatoms are consistently accommodated in the M$_{13}$ core. These data clearly suggest that the icosahedral Au$_{13}$ core of [Au$_{25}$(SR)$_{18}$]$^-$ provides active sites for the metal exchange reactions.

2.2. Molecular interactions/reactions at the M–SR interface

In sharp contrast to the electron-rich M(0) core, the M(I) atoms in the M(I)–SR protecting motifs are commonly electron-deficient (electronegative), owing to the electron withdrawing properties of the SR ligands coordinated to them. Such electronegative feature endows M(I) atoms with an increased affinity to electropositive molecules (entry I4, Fig. 1). For instance, in the aforementioned selective hydrogenation reaction of ketones or aldehydes catalysed by [Au$_{25}$(SR)$_{18}$]$^-$, the adsorption sites of the molecular H$_2$ are believed to be Au(I) in the SR–[Au(I)–SR]$_2$ motifs.[91,92] It has been well documented in the nanocatalysis literature that coordination-unsaturated Au atoms are active for adsorbing molecular H$_2$.[101,102] The subsequent dissociation of the molecular H$_2$ may result in two cleaved H atoms, whose reaction with the activated –C=O bond will eventually produce –CH–OH. In addition to the electron-deficiency, another important attribute that determines the reactivity of M(I) atoms in the M(I)–SR motifs is their improved accessibility compared to the core M(0) atoms. For example, Li et al. performed a detailed DFT calculation to reveal the basis of the interaction/reaction between the terminal alkynes (e.g., phenylacetylene) and [Au$_{25}$(SR)$_{18}$]$^-$.[103] The data suggest that the adsorption of phenylacetylene occurs on a triangular Au$_3$ facet composed of Au(I) atoms from three different dimeric SR–[Au(I)–SR]$_2$ motifs, because the triangular Au$_3$ facet is less blocked and it is more accessible to both the solvent and substrate molecules. It is believed that the adsorption and activation of –C≡CH in a similar manner can promote various reactions of –C≡CH (e.g., semi-hydrogenation,[104] carboxylation,[105] and Sonogashira cross-coupling[103]). It should also be noted that the motif-type Au$_3$ facet, together with three sulfur atoms coordinated to it and a core-type Au$_3$ facet underneath it, forms a "pocket-like cavity" on the surface of [Au$_{25}$(SR)$_{18}$]$^-$, which can provide heterogeneous active sites that can accommodate various catalytic reactions (vide infra).

In addition to the coordination-unsaturated metal centre, the M(I) in the M(I)–SR motifs of the metal NCs can also be active sites for metallophilicity (i.e., M(I)···M(I) interaction; entry I5, Fig. 1) and metal exchange reaction (entry I6, Fig. 1). For example, De Nardi et al. synthesized and crystallized Au$_{25}$(S-^{n}Bu)$_{18}$ NCs (HS-^{n}Bu denotes n-butanethiol).[106] The X-ray crystallography analysis suggests that the Au$_{25}$(S-^{n}Bu)$_{18}$ NCs align themselves into a one-dimensional (1D) polymeric chain, in which the adjacent NCs are connected by Au(I)···Au(I) interactions with a typical bond length of 3.15 Å (Fig. 3a). The formation of extensive Au(I)···Au(I) bonds should be attributed to the large content of Au(I) species in the protecting shell of Au$_{25}$(S-^{n}Bu)$_{18}$ NCs, as well as the appropriately flexible hydrocarbon chain of the –S-^{n}Bu ligand. Similar M(I)···M(I) interactions have been widely observed in aggregation-induced emission (AIE)-type metal NCs, offering an important mechanism for delivering enhanced luminescence.[108] The M(I) in the
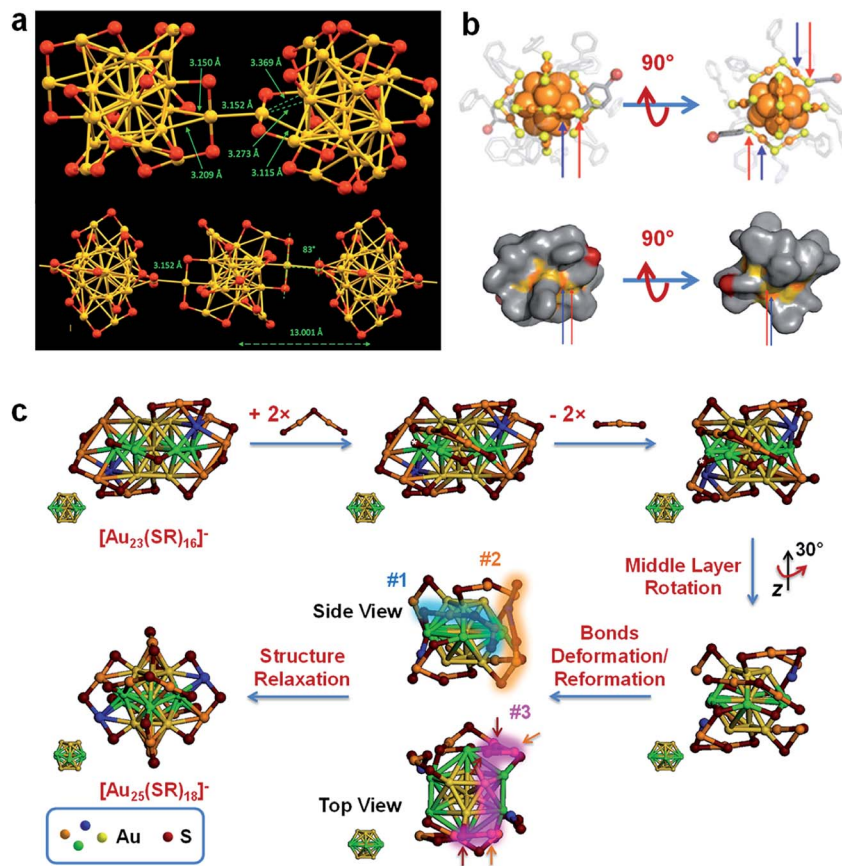
Fig. 3 Schematic illustration of (a) inter-cluster aurophilic interaction, (b) ligand exchange reaction, and (c) surface motif exchange reaction based on the Au−S interface of $Au_{25}(SR)_{18}$ (a), $[Au_{25}(SR)_{18}]^-$ (b), and $[Au_{23}(SR)_{16}]^-$ (c). (a) shows the formation of a 1D assembly by $Au_{25}(SR)_{18}$ based on the inter-cluster aurophilic interaction (colour code: golden, Au; red, S; reproduced with permission from ref. 106. Copyright 2014, American Chemical Society. (b) illustrates the preferential ligand exchange site on $[Au_{25}(S-C_2H_4Ph)_{18}]^-$ by HS-Ph-p-Br based on its crystal structure (top panel) and solvent-accessibility surface model (bottom panel), where blue arrows indicate the solvent-exposed Au and red arrows indicate the preferential ligand exchange site (colour code: orange, Au; yellow, S; grey, C; red, Br); reproduced with permission from ref. 107. Copyright 2014, American Chemical Society. (c) shows surface motif exchange induced size conversion from $[Au_{23}(SR)_{16}]^-$ to $[Au_{25}(SR)_{18}]^-$; the glowing belts #1–#3 indicate SR−[Au(I)−SR]$_2$ motifs formed in the size conversion process; reproduced with permission from ref. 61. Copyright 2018, the Authors, published by Springer Nature.

M(I)−SR motifs has also been identified as the active site for the metal exchange reaction (entry I6, Fig. 1). For example, Liao *et al.* performed a metal exchange reaction between $[Au_{25}(S-C_2H_4Ph)_{18}]^-$ and Hg^{2+} in the presence of excess 2-phenyl-ethanethiol (HS-C_2H_4Ph), leading to the formation of $Au_{24}Hg(S-C_2H_4Ph)_{18}$.[85] X-ray crystallography analysis showed that this metal exchange reaction occurred on the dimeric SR−[Au(I)−SR]$_2$ motifs, in which a Au atom in the protecting motif was replaced by the Hg heteroatom. It should be noted that in a very recent contribution, Fei *et al.* performed a comprehensive examination on the heteroatom doping site in $Au_{24}M(SR)_{18}$ NCs (M = Pt, Pd, Cd and Hg) by combining nuclear magnetic resonance (NMR), isotope labelling and X-ray crystallography, where the preferential doping site of Hg was identified as the vertex of the icosahedral Au_{13} core.[109] The different doping sites of Hg may be attributed to the dynamic diffusion of the Hg heteroatom in the frame of $Au_{24}Hg(SR)_{18}$.

Interestingly, recent progress in the experimental and theoretical catalysis of metal NCs suggests that the S atom of the SR ligand can also provide additional coordination sites for the substrate molecules in the catalytic reactions (entry I1, Fig. 1). For example, Kauffman *et al.* evaluated the electrocatalytic activity of $[Au_{25}(SR)_{18}]^q$ ($q = -1$, 0 and +1) for CO_2 reduction, CO oxidation, and O_2 reduction.[110] The DFT calculations indicate that the adsorption of CO_2 and CO may occur on the three S atoms in the pocket-like cavity of $[Au_{25}(SR)_{18}]^q$. The authors further pointed out that the charge state of $[Au_{25}(SR)_{18}]^q$ affected the adsorption energy of the reactants (*e.g.*, CO_2 and H^+ in CO_2 reduction, and CO and OH^- in CO oxidation) and products (*e.g.*, OH^- in O_2 reduction), which ultimately affected the catalytic activity of $[Au_{25}(SR)_{18}]^q$ in the above reactions.

Compared with the weak adsorption sites, the M−SR interface can mainly provide reactive sites for ligand exchange reactions (entry I2, Fig. 1), which have been widely used to customize the size, structure, surface chemistry and properties of metal NCs.[7,111-113] Ligand exchange reactions largely depend on the etching reaction of the foreign ligands on the existing M−SR interface of the metal NCs. As M(I)−SR motifs have been
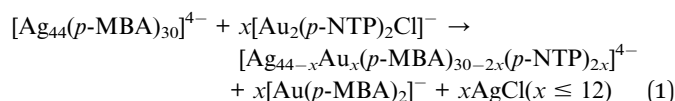
discovered with various structures and arrangement patterns on the surface of the M(0) core, the chemical environment of SR ligands can be diverse in the metal NCs.[114,115] Therefore, extensive research efforts have been made to determine the preferential reaction sites of ligand exchange reactions. For example, Heinecke *et al.* investigated the ligand exchange reaction of $Au_{102}(p\text{-MBA})_{40}$ (p-MBA = *para*-mercaptobenzoic acid or HS-Ph-p-COOH) with two molar equivalents of *para*-bromobenzene thiol (p-BBT or HS-Ph-p-Br), and successfully obtained single crystals of $Au_{102}(p\text{-MBA})_{40-x}(p\text{-BBT})_x$ with partial exchange of ligands (the average value of x, x_{ave} = 1.08).[116] The X-ray crystallography analysis showed that this ligand exchange reaction occurs preferentially on the Au(I) atoms in the two SR–Au(I)–SR motifs that are most accessible to the solvent. A similar observation was recorded by the same group in the ligand exchange reaction between $[Au_{25}(S\text{-}C_2H_4Ph)_{18}]^-$ and HS-Ph-p-Br, where the incoming HS-Ph-p-Br preferentially bonded to the Au(I) atoms in the protecting shell of $[Au_{25}(S\text{-}C_2H_4Ph)_{18}]^-$ that were most accessible to the solvent (Fig. 3b).[107] Considering that SR–$[Au(I)\text{–}SR]_2$ is an exclusive protecting motif in the protecting shell of $[Au_{25}(SR)_{18}]^-$, there exist one core-type (bonded to the Au(0) core) and one apex-type (not bonded to the Au(0) core) $-S\text{-}C_2H_4Ph$ ligands bonded to the Au(I) atom that is most accessible to the solvent. However, the X-ray crystallography data show that the core-type $-S\text{-}C_2H_4Ph$ ligand is more likely to be replaced by the incoming HS-Ph-p-Br ligand, with an occupancy of 74.6%. The authors attributed the preferential exchange of the core-type SR ligands by the incoming HS-Ph-p-Br ligand to the enhanced π–π interactions of the latter with the remaining $-S\text{-}C_2H_4Ph$ ligands.

Niihori *et al.* also observed a similar preferential exchange of the core-type $-S\text{-}C_2H_4Ph$ ligands in the reaction of $Au_{24}Pd(S\text{-}C_2H_4Ph)_{18}$ with 1-dodecanethiol (HS-$C_{12}H_{25}$).[117] The authors analysed the population distribution of the coordination isomers produced by the above ligand exchange reaction by reversed-phase high performance liquid chromatography (HPLC), and found that, at the early stage of the reaction (reaction time = 4 min), the abundance of the core-type exchanged $Au_{24}Pd(S\text{-}C_2H_4Ph)_{17}(SC_{12}H_{25})$ was 13 times higher than that of the apex-type exchanged one. In order to gain fundamental insights into the different reactivities of the core-type and apex-type SR ligands in the ligand exchange reactions, Pengo *et al.* monitored the ligand exchange kinetics of $[Au_{25}(S\text{-}C_2H_4Ph)_{18}]^-$ with various incoming thiols (including HS-Ph, HS-Ph-p-CH₃, and HS-Ph-p-OCH₃) by ^{1}H nuclear magnetic resonance (^{1}H-NMR) spectroscopy.[118] The most important finding is that the selectivity to the core-type exchanged product is highly dependent on the electronic structure of the incoming thiols, where thiols with an electron-donating substituent at the *para* position have lower selectivity for the core-type exchanged products. This conclusion is consistent with recent findings of Salassa *et al.*, where the result of the ligand exchange reaction of $[Au_{25}(SR)_{18}]^-$ is highly dependent on solution stability and intermolecular interaction of thiols, as well as their affinity to the Au frame.[119] In addition to ^{1}H NMR spectrometry, isothermal titration calorimetry (ITC) has also been introduced

by Baksi *et al.* to evaluate the reactivity of metal NCs with free thiols.[120]

Another important reaction that occurs at the M–S interface is the surface motif exchange reaction (SME; entry I3, Fig. 1). The significant difference from conventional ligand exchange reactions is that the exchange units in SME are M(I)–SR motifs/complexes, which should be inherently attributed to the dynamic nature of M(I)–SR motifs on the surface of the M(0) core.[112] In metal-*cum*-ligand exchange reaction, the discovery of M(I)–SR motifs/complexes as the exchanging units can be traced back to 2003, when both metal and ligand exchanges were observed in a two-phase reaction of hexanethiolate-protected Au NCs (~1.6 nm in the toluene phase) and tiopronin-protected Ag NCs (~1.6 nm in the aqueous phase).[62] Since the metal and ligand exchange reaction can be almost prohibited under a N_2 environment, the authors proposed a Au(I)–SR complex-assisted mechanism, in which the Au(I)–SR complexes formed by oxidative etching of Au NCs were identified as the "catalysts" that made possible simultaneous exchange of metal and ligand. This assertion is supported by a control experiment, which shows that adding a catalytic amount of Au(I)–SR complexes to the reaction system under N_2 can restore the exchange reactions. Yao *et al.* recently demonstrated the versatility of SME reaction in the cluster reactions based on extensive mass spectrometry analysis.[60] By monitoring the reaction between $[Ag_{44}(p\text{-MBA})_{30}]^{4-}$ and Au(I)–(p-NTP) complexes (p-NTP = *para*-nitrothiophenol or HS-Ph-p-NO₂) using electrospray ionization mass spectrometry (ESI-MS), the authors found that the exchange reaction mainly occurred through the following reaction (eqn (1)).

$$[Ag_{44}(p\text{-MBA})_{30}]^{4-} + x[Au_2(p\text{-NTP})_2Cl]^- \rightarrow$$
$$[Ag_{44-x}Au_x(p\text{-MBA})_{30-2x}(p\text{-NTP})_{2x}]^{4-}$$
$$+ x[Au(p\text{-MBA})_2]^- + xAgCl (x \leq 12) \quad (1)$$

It was also found that a similar SME reaction could effectively drive the size conversion reaction of Au NCs. An isoelectronic size conversion reaction of $[Au_{23}(SR)_{16}]^-$ to $[Au_{25}(SR)_{18}]^-$ was closely tracked by UV-vis absorption spectroscopy and ESI-MS, indicating that the isoelectronic size conversion reaction was based on the exchange of SR–$[Au(I)\text{–}SR]_2$ units.[61] Therefore, the reaction of the isoelectronic size conversion can be described by the following equation (eqn (2)).

$$[Au_{23}(SR)_{16}]^- + 2[Au_2(SR')_3]^- \rightarrow [Au_{25}(SR)_{12}(SR')_6]^-$$
$$+ 2[Au(SR)_2]^- \quad (2)$$
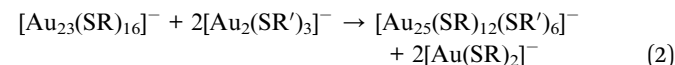
where SR′ denotes the incoming thiolate ligand that can be the same as or different from the original thiolate ligand SR. Tandem mass spectrometry was then used to study the structural relativity of $[Au_{23}(SR)_{16}]^-$ and $[Au_{25}(SR)_{18}]^-$, and an atomic-level mechanism of the symmetry-breaking core transformation induced by SME was proposed (Fig. 3c). Briefly, the adsorption of a SR′–$[Au(I)\text{–}SR']_2$ unit can induce cleavage of a SR–Au(I)–SR unit from the original SR–$[Au(I)\text{–}SR]_3$ motif on the surface of $[Au_{23}(SR)_{16}]^-$. Such cleavage of two SR–$[Au(I)\text{–}SR]_3$ motifs at the symmetric sites of $[Au_{23}(SR)_{16}]^-$ will cause a structural

transformation of the Au_{13} core from a cuboctahedron to an icosahedron, finally producing $[Au_{25}(SR)_{18}]^-$.

2.3. Molecular interactions/reactions on SR ligands

Because SR ligands constitute the outermost layer of metal NCs, they largely determine the recognition chemistry and surface reaction of metal NCs. Due to the size, structure, and function diversity of the hydrocarbon tails of SR ligands, they can adapt to various covalent and non-covalent interactions/reactions.

Covalent conjugation is commonly used to introduce additional functions into metal NCs for biomedical applications.[121–126] Among the various covalent conjugation strategies documented in biomedical and organic chemistry, the amination reaction based on 1-ethyl-3-(3-dimethylaminopropyl) carbodiimide (EDC) is the most widely used method for surface modification of metal NCs (entry R4, Fig. 1), due to its mild operation conditions as well as abundant carboxyl or amine groups on the surface of water-soluble metal NCs.[121,122,124,125] For example, Pyo et al. used EDC chemistry to conjugate folic acid (FA) with $Au_{22}(SG)_{18}$ (H-SG or GSH = glutathione, Fig. 4a),[122] where the latter is the first atomically precise Au NC with strong red emission (emission wavelength, $\lambda_{em} = 665$ nm; excitation wavelength, $\lambda_{ex} = 520$ nm).[42] It is worth noting that, in order to effectively inhibit the inter-particle coupling of SG ligands through $-NH_2$ and $-COOH$, the authors protected the $-NH_2$ groups with benzyl chloroformate (CBz) before EDC coupling. In a separate study, Vankayala et al. made full use of EDC chemistry to activate the carboxyl group of 11-mercaptoundecanoic acid (MUA), and conjugated a nucleus-

targeting peptide (TAT, peptide sequence: N-GRKKRRQRRR-C) to the Au NCs protected by MUA.[127] Such conjugation allows Au NCs to have a high nucleus targeting efficacy in HeLa cells, while keeping the emission intensity of Au NCs unaffected. In addition, the chemically conjugated TAT peptide can change the zeta potential of Au NCs from negative to positive, making them also useful for gene delivery.

In addition to covalent conjugations, a large number of non-covalent interactions/reactions have also been documented based on the SR groups for surface modification or self-assembly of metal NCs. The carboxyl, amine or hydroxyl groups of the SR ligands are the ideal sites for the H-bonds on the surface of metal NCs (entry R5, Fig. 1). The directional H-bond not only plays a key role in determining the solvation behaviour of metal NCs, but is also effective in controlling the self-assembly and/or crystallization behaviour of metal NCs. For example, based on the well-known Brust–Schiffrin method, Desireddy et al. designed an efficient protocol to synthesize molecularly pure $[Ag_{44}(p\text{-MBA})_{30}]^{4-}$ on a large scale, followed by its crystallization in a dimethylformamide (DMF) solution in its fully protonated form.[12] The X-ray crystallography examination of the obtained single crystals showed that a strong network of H-bonds may be formed between the p-MBA ligands of adjacent NCs. Extensive H-bonds have also been found in the assemblies or supercrystals of other metal NCs protected by p-MBA ligands, among which $Au_{102}(p\text{-MBA})_{44}$ is a good example.[128] In sharp contrast, after deprotonation, the carboxyl group can be turned into an active site for electrostatic interaction (entry R6, Fig. 1). For example, Yao et al. designed a phase-transfer-driven ion-
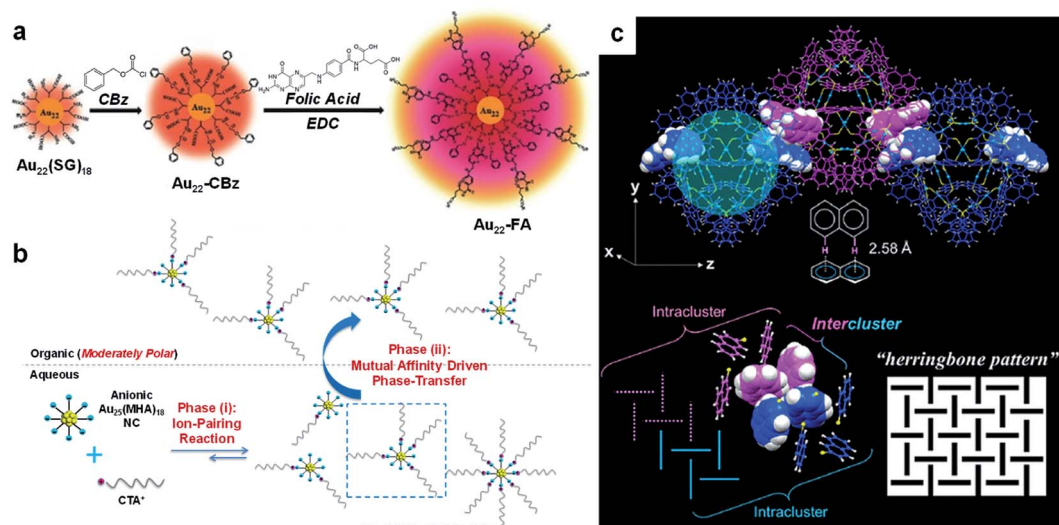

Fig. 4 Schematic illustration of (a) 1-ethyl-3-(3-dimethylaminopropyl)carbodiimide (EDC) conjugation reaction, (b) ion-pairing reaction, and (c) CH−π interaction occurring on the SR ligands of metal NCs. (a) illustrates the EDC conjugation between folic acid (FA) and $Au_{22}(SG)_{18}$ (SG = glutathione ligand), where the $-NH_2$ groups of SG ligands are protected by benzyl chloroformate (CBz) prior to the EDC reaction; reproduced with permission from ref. 122. Copyright 2017, Wiley-VCH. (b) illustrates the production of amphiphilic $Au_{25}(MHA)_{18}@xCTA$ NCs (x = 6−9) by the phase-transfer-driven ion-pairing reaction, where MHA denotes 6-mercaptohexanoic acid and CTA denotes cetyltrimethylammonium; reproduced with permission from ref. 129. Copyright 2015, American Chemical Society. (c) exhibits inter-cluster CH−π interactions (top panel) and the "herringbone pattern" of −S-Nap ligands in the supercrystals of $Au_{103}S_2(S\text{-Nap})_{41}$ NCs, where HS-Nap denotes 2-naphthalenethiol (colour code: light blue, motif Au(ι); yellow, S; light grey, H; blue/magenta, C); reproduced with permission from ref. 55. Copyright 2017, American Chemical Society.

pairing reaction for facile preparation of amphiphilic metal NCs (Fig. 4b).[129] The ion-pairing reaction is based on the electrostatic interaction between the –COO[−] group of $Au_{25}(MHA)_{18}$ (MHA = 6-mercaptohexanoic acid) and hydrophobic cations such as CTA[+] (CTA[+] = cetyltrimethylammonium cation). Considering the dynamics of the ion-paring reaction in the aqueous phase, different numbers of CTA[+] species can be patched on the hydrophilic surface of $Au_{25}(MHA)_{18}$. A mixture of toluene and ethanol was then introduced as the organic phase, and amphiphilic $Au_{25}(MHA)_{18}@xCTA$ ($x = 6$–9) NCs were selectively extracted from the aqueous phase. The equilibrium of the ion-pairing reaction can effectively regenerate the extracted $Au_{25}(MHA)_{18}@xCTA$ species in the aqueous phase, constituting a sustained mechanism for the production of amphiphilic Au NCs.

The obvious difference from the prosperity of electrostatic interactions in the water phase is that organic-soluble metal NCs usually lack surface charges, so electrostatic interactions are less efficient in directing the self-assembly and application of metal NCs. However, because aromatic thiols are widely used in the synthesis of metal NCs in the organic phase, π interactions (e.g., π–π and CH–π interactions) have become the dominant factor in controlling the self-assembly of NCs and their applications in the organic phase (entry R1, Fig. 1). For example, Higaki et al. recently produced molecularly pure $Au_{103}S_2(S\text{-}Nap)_{41}$ NCs (HS-Nap = 2-naphthalenethiol) through a ligand exchange reaction between $Au_{99}(S\text{-}Ph)_{42}$ and HS-Nap.[55] The obtained $Au_{103}S_2(S\text{-}Nap)_{41}$ NCs were crystallized into a monoclinic lattice by a typical vapour diffusion method. Of particular interest, the $Au_{103}S_2(S\text{-}Nap)_{41}$ NCs in the supercrystals are packed through hierarchical CH–π interactions (Fig. 4c). At the intra-cluster level, the –S-Nap ligands can first form dimers through T-shaped CH–π interactions (which may also be regarded as T-shaped π–π interactions). Through similar T-shaped CH–π interactions, two pairs of such dimers can form a cyclic tetramer. The lateral C–H and naphthalene ring in the formed tetramers provide active sites for the CH–π interaction between the clusters, which binds the two tetramers from adjacent NCs together, resulting in a herringbone-like arrangement of naphthalene rings across intra- and inter-cluster levels. In addition to the CH–π interaction, it has also been found that the inter-cluster π–π interactions are important to determine the assembly behaviour of metal NCs. For example, Hossain et al. obtained single crystals of five different $Au_4Pt_2(SR)_8$ NCs with different SR ligands, namely isopropanethiol (HS-CH(CH$_3$)$_2$), 2,4,6-trimethylbenzylmercaptane (HS-CH$_2$Ph(CH$_3$)$_3$), 4-tert-butylbenzylmercaptane (HS-CH$_2$-Ph^{t}Bu), and HS-C$_2$H$_4$Ph, respectively.[130] Interestingly, only $Au_4Pt_2(S\text{-}CH_2Ph^tBu)_8$ and $Au_4Pt_2(S\text{-}C_2H_4Ph)_8$ NCs can organize themselves into a 1D structure in their supercrystals, and the Au–Au distance between clusters is short, within 3.08 Å. The preferential 1D assembly is attributed to the strong π–π interactions and appropriately weak steric repulsion of –S-CH$_2$Ph^{t}Bu or –S-C$_2$H$_4$Ph ligands, thereby enabling extensive aurophilic interactions along the longitudinal orientation of the 1D structure. It should be noted that van der Waals interactions are also commonly observed in the metal NCs protected by alkyl

and aryl ligands (entry R3, Fig. 1), which can facilitate their self-assembly into hierarchical architectures (see more details in Section 4.1).[15,131]

Host–guest interaction is an important type of supramolecular interaction, finding increasing acceptance in molecular recognition and self-assembly chemistry.[132–134] A useful host–guest interaction can be established on the surface of metal NCs through an appropriate surface engineering strategy (entry R2, Fig. 1). For example, Mathew et al. demonstrated that a host–guest interaction can be established between β-cyclodextrin (CD) and the 4-tert-butylbenzenethiolate (–S-Ph-p-^{t}Bu) ligand of $Au_{25}(S\text{-}Ph\text{-}p\text{-}^tBu)_{18}$ NCs.[135] In this way, the authors can anchor β-CD on the surface of $Au_{25}(S\text{-}Ph\text{-}p\text{-}^tBu)_{18}$, producing $Au_{25}(S\text{-}Ph\text{-}p\text{-}^tBu)_{18}@CD_x$ ($x = 1$–4). It has been demonstrated that the β-CD modification on the surface of $Au_{25}(S\text{-}Ph\text{-}p\text{-}^tBu)_{18}$ can not only enhance its stability against Cu^{2+} etching, but also change its absorption and emission spectra, providing a useful mechanism for sensing applications. Recently, similar host–guest interactions have been used to decorate the $Au_{40}(S\text{-}Adm)_{22}$ (HS-Adm = adamantanethiol) with metal organic frameworks (MOFs) constructed by γ-CD and K^{+} (γ-CD-MOFs).[136] The as-produced $Au_{40}(S\text{-}Adm)_{22}@\gamma\text{-}CD\text{-}MOF$ exhibits enhanced water solubility and improved catalytic activity for H_2O_2 reduction. In addition to modifying CDs on the surface of metal NCs, thiolated CDs can also be used as thiolate ligands in the synthesis of metal NCs. For example, per-6-thio-β-cyclodextrin (HS-β-CD) was mixed with HAuCl$_4$, followed by NaBH$_4$ reduction to synthesize Au NCs@β-CD.[137] As evidenced by transmission electron microscopy (TEM) images, the core size of the as-synthesized Au NCs@β-CD is less than 3 nm. After being immobilized on the surface of TiO$_2$, the TiO$_2$–Au NCs@β-CD nanocomposite has a 2-fold enhanced photocatalytic activity (compared with pure TiO$_2$) for the degradation of a model pollutant, methyl orange (MO), which should be attributed to the host–guest interactions between β-CD and MO molecules.

Other than CD, another marked host–guest interaction between metal NCs and fullerenes has been documented.[138–140] For example, Chakraborty et al. mixed a toluene solution of C$_{60}$ with a DMF solution of $[Ag_{29}(BDT)_{12}]^{3-}$ NCs (BDT = 1,3-benzenedithiol), forming $[Ag_{29}(BDT)_{12}@(C_{60})_x]^{3-}$ ($x = 1$–9) adducts.[139] DFT calculations suggest that the C$_{60}$ is preferentially tethered in the cavity formed by the arrangement of BDT ligands, and the π–π interaction between the BDT ligand and C$_{60}$ is identified as the predominant driving force for this complexation event. Very recently, the authors demonstrated that similar host–guest interactions can easily be established between C$_{60}$ and $[Ag_{25}(DMBT)_{18}]^-$ or $[Au_{25}(S\text{-}C_2H_4Ph)_{18}]^-$ NCs (DMBT = 2,4-dimethylbenzenethiol), providing an easy way to assemble clusters into dendritic networks.[140] More interestingly, by virtue of the supramolecular interaction between crown ethers and aromatic protecting ligands, co-crystallization of dibenzo-18-crown-6 and $[Ag_{29}(BDT)_{12}(PPh_3)_x]^{3-}$ NCs (PPh$_3$ = triphenylphosphine) can also be achieved.[141] This chemistry should be useful in engineering both physicochemical properties and self-assembly behaviour of metal NCs.

3. Molecular interactions/reactions in synthesis of metal NCs

With the continuous development of synthetic chemistry, several efficient strategies have been devised to produce atomically precise metal NCs with customizable size, composition, and structure. These methods include bottom-up growth,[48,49,51] ligand exchange,[111] and heteroatom alloying.[142] These approaches inevitably involve the reaction of metal NCs with redox species, SR ligands, metal ions, M(I)–SR/M(II)–SR complexes, and other NCs. In this section, we will briefly discuss the molecular interactions/reactions that control the synthesis of thiolate-protected noble metal NCs.

3.1. Molecular interactions/reactions in bottom-up growth of metal NCs

In a typical bottom-up growth method, metal salts are mixed with thiol ligands to generate M(I)–SR complexes, followed by a reduction-induced growth of the M(0) core.[73,76] A balance between the reduction-induced growth and the SR/M(I)–SR passivation of the M(0) core leads to the formation of stable metal NCs. Therefore, the bottom-up growth of metal NCs is largely determined by the reaction of growing NCs with the reductive species, M(I)–SR complexes, or intermediate NC species.

Due to its mild reduction kinetics, CO has been widely used as a reducing agent for the production of a variety of Au NCs, including $Au_{15}(SR)_{13}$,[143] $Au_{18}(SR)_{14}$,[143] $Au_{22}(SR)_{18}$,[42] $[Au_{25}(SR)_{18}]^-$,[143] $Au_{29}(SR)_{20}$,[144] $Au_{38}(SR)_{24}$[49] and $[Au_{44}(SR)_{26}]^{2-}$.[49] The mild and easily quenched reduction kinetics of CO can not only maintain a well-controlled environment to produce atomically precise metal NCs with desired sizes, but also provide a good means for capturing important intermediates along the growth path of metal NCs. For example, Luo et al. fine-tuned the reducing capability of CO at the optimal pH (= 11.6) for synthesis of $[Au_{25}(S\text{-}Ph\text{-}m\text{-}COOH)_{18}]^-$ (HS-Ph-m-COOH = meta-mercaptobenzoic acid), in an appropriately slow manner (reaction time = 72 h).[48] Such a slow size evolution process allows the authors to monitor the size growth reaction of $[Au_{25}(S\text{-}Ph\text{-}m\text{-}COOH)_{18}]^-$ by UV-vis absorption spectroscopy and ESI-MS. Through this method, the authors identified a total of 29 Au(I)–SR complex/NC species during the entire growth process of $[Au_{25}(S\text{-}Ph\text{-}m\text{-}COOH)_{18}]^-$. All these species have an even number of valence electrons (N), which indicates that the growth reaction of $[Au_{25}(SR)_{18}]^-$ features a step-wise 2-electron $(2e^-)$ hopping mechanism. The $2e^-$ hopping mechanism is indeed fuelled by the reactions of CO, initially with the Au(I)–SR complexes and subsequently with the intermediate Au NC species. Based on the time-dependent abundance of individual Au(I)–SR complex/NC species, the authors can also propose detailed formation and consumption reactions for individual NC species, thus constituting a step-by-step growth pathway for $[Au_{25}(SR)_{18}]^-$. For example, the formation of an important intermediate, $Au_{18}(SR)_{14}$, powered by CO reduction can be made possible by the following reaction (eqn (3)).

$$Au_{15}(SR)_{13} + Au_3(SR)_3 + CO + 4OH^- \rightarrow Au_{18}(SR)_{14} + 2[SR]^- + CO_3^{2-} + 2H_2O \quad (3)$$
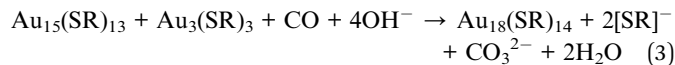
where the $Au_{15}(SR)_{13}$ was formed by CO reduction of Au(I)–SR complexes in the previous step.

The molecular reaction between Au NCs and CO was further investigated by Yao et al. in seed-mediated growth of $[Au_{25}(SR)_{18}]^-$ to form $[Au_{44}(SR)_{26}]^{2-}$.[49] As shown in Fig. 5a, the molecularly pure $[Au_{25}(p\text{-}MBA)_{18}]^-$ NCs were allowed to react with Au(I)-(p-MBA) complexes and CO in an aqueous solution under highly alkaline conditions (pH = 13.0), generating atomically precise $[Au_{44}(p\text{-}MBA)_{26}]^{2-}$. This seed-mediated growth reaction was carefully tracked by time-course UV-vis absorption spectroscopy and ESI-MS. By systematically analysing the time-dependent abundance of a total of 35 Au(I)–SR complex/NC species in the seed-mediated growth reaction, the authors identified two different size-growth pathways for $[Au_{44}(SR)_{26}]^{2-}$: monotonic LaMer growth and volcano-shaped aggregative growth. Although the size evolution patterns can be diverse, the valence electrons of Au NCs evolve by following the universal $2e^-$ hopping mechanism, which is in good agreement with the previous report.[48] More importantly, the authors succeeded in capturing an important reaction intermediate, $[Au_{25}(p\text{-}MBA)_{18}CO]^-$, in an aqueous solution of $[Au_{25}(p\text{-}MBA)_{18}]^-$ saturated by CO (Fig. 5b). These data clearly suggest that the size growth based on the stable cluster size can be initiated by adsorbing reductive substances (e.g., CO) on the growing NC, where $[Au_{25}(SR)_{18}]^-$ is a good example. The CO adsorption site is likely to be the pocket-like cavity on the surface of $[Au_{25}(SR)_{18}]^-$, as discussed in the previous section.

Compared with the growth reaction promoted by CO, the molecular-level fundamentals of the $NaBH_4$-driven size growth reaction of metal NCs are less investigated, although $NaBH_4$ is widely used as a versatile reducing agent in the Brust–Schiffrin synthesis of metal NCs. Specifically, although several remarkable achievements have been made in the past decade regarding the chemical states of Au precursors prior to $NaBH_4$ reduction in the typical Brust–Schiffrin method,[145-147] little is known about the size-growth pathway of metal NCs after addition of $NaBH_4$. This is probably due to the strong reducing ability of $NaBH_4$, which usually provides a fast and less-controllable reduction kinetics in the size growth reaction of metal NCs. This technical challenge has been recently addressed by Chen et al.[51] In contrast to feeding a large excess of $NaBH_4$ (>10 molar equivalent of Au) into the reaction mixture in the typical Brust–Schiffrin methods, the authors significantly reduced the feeding amount of $NaBH_4$ to the stoichiometric value according to eqn (4).

$$32/x \, [Au(SR)]_x + 8e^- = [Au_{25}(SR)_{18}]^- + 7[Au(SR)_2]^- \quad (4)$$
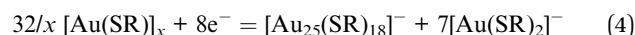
The low dose of $NaBH_4$ maintains an appropriately slow reduction kinetics, so that ESI-MS can track the growth reaction of $[Au_{25}(SR)_{18}]^-$. Therefore, real-time ESI-MS was used to monitor the size growth reaction powered by $NaBH_4$, showing a $2e^-$ hopping mechanism similar to that observed in CO reduction fuelled size growth. Given the ubiquitous observation
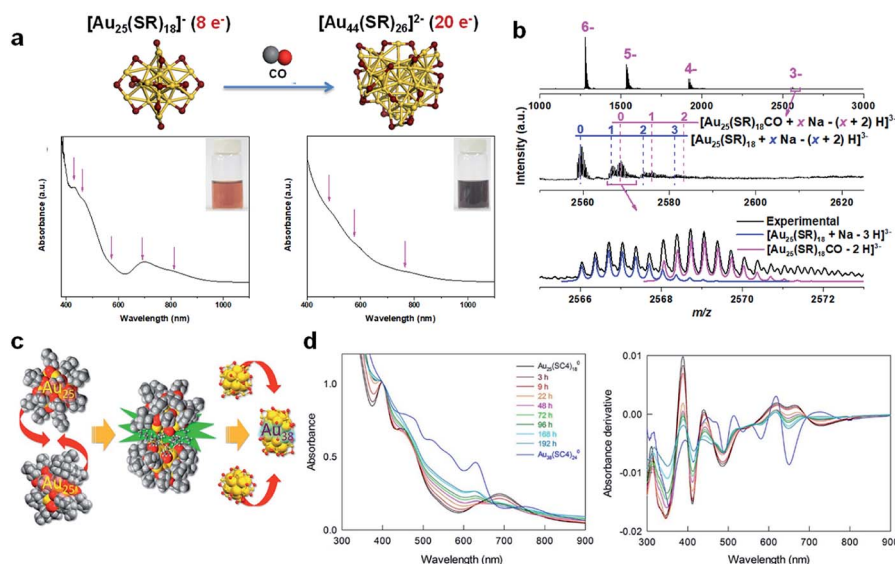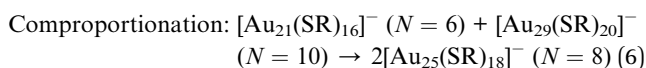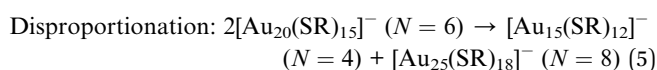
Fig. 5 (a) Schematic illustration (top panel) and UV–vis absorption spectra (bottom panel) of size growth from $[Au_{25}(SR)_{18}]^-$ to $[Au_{44}(SR)_{26}]^{2-}$ via the CO-reduction method, where magenta arrows indicate the characteristic absorption of $[Au_{25}(SR)_{18}]^-$ and $[Au_{44}(SR)_{26}]^{2-}$ (colour code: golden, Au; purple, S). (b) ESI-MS spectra of $[Au_{25}(SR)_{18}CO]^-$ adducts identified in the $[Au_{25}(SR)_{18}]^-$ solution saturated by CO. (a) and (b) are reproduced with permission from ref. 49. Copyright 2017, the Authors, published by Springer Nature. (c) Schematic illustration of the formation of $Au_{38}(SR)_{24}$ by the fusion of two $Au_{25}(SR)_{18}$ NCs. (d) Time-dependent UV–vis absorption and the corresponding absorption-derivative spectra of the size growth of $Au_{38}(SR)_{24}$ by the fusion of two $Au_{25}(SR)_{18}$ NCs. (c) and (d) are reproduced with permission from ref. 148. Copyright 2018, American Chemical Society.

of the $2e^-$ hopping mechanism in various reducing systems, the root cause of this $2e^-$ growth in Au NCs may be the inherent stability of Au NCs with even valence electrons.

In addition to reductive species prompted size growth, the size evolution of metal NCs can also be accomplished by many other cluster reactions, including inter-cluster reactions (e.g., disproportionation and comproportionation reactions) and cluster reactions with Au(I)–SR complexes (e.g., isoelectronic addition reactions). It should be mentioned that all these reactions have been observed in the size growth pathways of Au NCs induced by CO or $NaBH_4$ reduction.[48,49] For example, it is suggested that $8e^-$ $[Au_{25}(SR)_{18}]^-$ can be formed through the disproportionation reaction of $6e^-$ $[Au_{20}(SR)_{15}]^-$ (eqn (5)) or the comproportionation reaction between $6e^-$ $[Au_{21}(SR)_{16}]^-$ and $10e^-$ $[Au_{29}(SR)_{20}]^-$ (eqn (6)).[48]

Disproportionation: $2[Au_{20}(SR)_{15}]^- (N = 6) \rightarrow [Au_{15}(SR)_{12}]^-$
$(N = 4) + [Au_{25}(SR)_{18}]^- (N = 8)$ (5)

Comproportionation: $[Au_{21}(SR)_{16}]^- (N = 6) + [Au_{29}(SR)_{20}]^-$
$(N = 10) \rightarrow 2[Au_{25}(SR)_{18}]^- (N = 8)$ (6)

In a recent contribution, Dainese et al. reported that the $14e^-$ $Au_{38}(SR)_{24}$ was produced through comproportionation of two $7e^-$ $Au_{25}(SR)_{18}$ NCs, in which the incubation of neutral $Au_{25}(SR)_{18}$ in toluene at 65 °C for 10–14 days can complete the size conversion (Fig. 5c).[148] The slow reaction kinetics and distinctly different electronic structures of the precursor and product NCs facilitate monitoring the entire size conversion reaction by UV–vis absorption spectroscopy (Fig. 5d) and differential pulse voltammetry (DPV), which suggests a second-order rate law for such comproportionation reaction. The

authors further found that the neutral core charge and paramagnetic nature of $Au_{25}(SR)_{18}$ are essential for the size conversion, which indicates that the size conversion is most likely to be accomplished by the collision and fusion of two $Au_{25}(SR)_{18}$ NCs following eqn (7).

$$2Au_{25}(SR)_{18} (N = 7) \rightarrow Au_{38}(SR)_{24} (N = 14) + 12Au(SR) \quad (7)$$
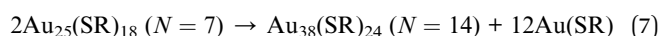
More recently, Suyama et al. reported a comproportionation reaction between $6e^-$ $Au_{24}Pt(SR)_{18}$ and $8e^-$ $[Au_{24}Pt(SR)_{18}]^{2-}$, yielding $7e^-$ $[Au_{24}Pt(SR)_{18}]^-$ (eqn (8)) with its structure unambiguously resolved by X-ray crystallography.[149] It is interesting to note that this is a comproportionation reaction that changes the valence electron count while keeping the cluster size unchanged. The formation of open-shell $7e^-$ $[Au_{24}Pt(SR)_{18}]^-$ is attributed to the superior adiabatic electron affinity of Au_{24}-$Pt(SR)_{18}$ (3.32 eV) to that of $[Au_{24}Pt(SR)_{18}]^-$ (2.47 eV). The authors further proposed a dimerization mechanism assisted by the inter-cluster aurophilic interaction for this comproportionation reaction.

$$Au_{24}Pt(SR)_{18} (N = 6) + [Au_{24}Pt(SR)_{18}]^{2-} (N = 8) \rightarrow$$
$$2 [Au_{24}Pt(SR)_{18}]^- (N = 7) \quad (8)$$
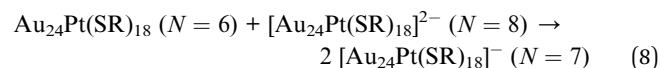
In addition to disproportionation and comproportionation reactions that change the valence electrons of metal NCs, the size growth of metal NCs can also be achieved through isoelectronic addition reactions without changing the valence electron count. Isoelectronic addition reaction refers to the size growth reaction by adding $0e^-$ M(I)–SR complexes to the pre-formed metal NCs, and a good example is to convert $[Au_{23}(SR)_{16}]^- (N = 8)$ to $[Au_{25}(SR)_{18}]^- (N = 8)$.[61] The molecular-

level stoichiometry (eqn (2)) and atomic-level mechanism (Fig. 3c) of this reaction have been discussed in detail in Section 2.2.

Intrinsic chirality has become one of the most attractive properties in cluster research, which should be attributed to the increasing recognition of the importance of cluster chirality in determining the biomedical and catalytic applications of metal NCs.[24,150,151] The unique interactions/reactions of chiral metal NCs with chiral counterions have therefore been used for the enantioselective separation or synthesis of metal NCs. For example, Yao *et al.* originally developed a phase transfer method based on chiral counterions to enhance the enantiomeric excess of Au NCs protected by penicillamine.[152] The Au NCs protected by racemic penicillamine (*rac*-Pen) were electrostatically paired with a chiral cation, (1*R*,2*S*)-*N*-dodecyl-*N*-methylephedrinium (DME$^+$), completely transferring the *rac*-Pen-protected Au NCs from the aqueous phase into the chloroform phase. The phase-transferred Au NCs show circular dichroism (CD) signals in the wavelength window of 300–700 nm, while the original Au NCs in the aqueous phase are optically inactive. These data suggest that DME$^+$ has a favourable interaction with one specific enantiomer of penicillamine-protected Au NCs, preferentially making it stable and enriched in the chloroform phase. Knoppe *et al.* used a similar chiral phase transfer method, and performed a DME$^+$-induced phase transfer for the racemic mixture of Au$_{102}$(SR)$_{44}$.[153] It should be recalled that the chirality of Au$_{102}$(SR)$_{44}$ intrinsically originates from the mirror arrangement of Au(I)–SR motifs on the Au$_{79}$ core with a capped Marks-decahedron (MD) structure. In this way, the partial phase transfer of Au$_{102}$(SR)$_{44}$ NCs can produce opposite CD responses in the aqueous and organic (chloroform) phases, which clearly indicates a preferential binding habit of DME$^+$ to one specific enantiomer of Au$_{102}$(SR)$_{44}$.

Yan *et al.* have also used the enantioselective ion pairing between metal NCs and chiral counterions in a single phase system to separate a racemic mixture of metal NCs.[151] *N*-Benzylcinchonidinium (BCD$^+$) and *N*-benzylcinchoninium (BCN$^+$) were used as chiral cations to react with a racemic mixture of [Ag$_{28}$Cu$_{12}$(SR)$_{24}$]$^{4-}$, whose chirality originated from the asymmetric packing of both the Ag$_{28}$ core and Cu$_3$(SR)$_6$ motifs. It has been shown that incubating racemic [Ag$_{28}$Cu$_{12}$(SR)$_{24}$]$^{4-}$ with BCD$^+$ or BCN$^+$ can selectively impart a specific enantiomer (the *R* enantiomer for BCD$^+$ and the *L* one for BCN$^+$) with a higher solution durability. Based on this knowledge, the authors directly synthesized [Ag$_{28}$Cu$_{12}$(SR)$_{24}$]$^{4-}$ in the presence of BCD$^+$ or BCN$^+$, which led to the formation of a large number of optically active enantiomers. These data indicate the usefulness of the enantioselective ion-pairing reaction in the asymmetric synthesis of metal NCs.

3.2. Molecular interactions/reactions in alloying of metal NCs

It has been demonstrated that alloying can effectively enhance the stability and materials performance (*e.g.*, luminescence[154] and catalytic activity[99,105,155]) of metal NCs. In addition to the well-known co-reduction method, the alloying can be achieved

at atomic precision through reactions of the preformed metal NCs with various heteroatom sources, including metal cations,[53] M(I)–SR/M(II)–SR complexes, metal NCs, and metal surfaces. Based on the various sources of heteroatoms, the molecular interactions/reactions of metal NCs that control the alloying process are diverse.

Inspired by the co-reduction method, where different metal salts are used to generate alloy NCs, metal salts or metal cations have long been used as sources of heteroatoms to react with the preformed metal NCs (*i.e.*, parent metal NCs), aiming at producing alloy NCs while keeping the size monodispersity of the parent NCs uncompromised. The reactions between metal cations and the parent metal NCs can be accomplished by a conventional galvanic reaction. For example, several galvanic reactions have been conducted based on atomically precise [Ag$_{25}$(SR)$_{18}$]$^-$.[78,157] A galvanic reaction between [Ag$_{25}$(SR)$_{18}$]$^-$ and Au$^+$ or Au^{3+} usually produces [AuAg$_{24}$(SR)$_{18}$]$^-$, where the Au heteroatom is located at the centre of the icosahedral M$_{13}$ core as revealed by X-ray crystallography analysis.[78,157] In sharp contrast, the galvanic reaction between Pd^{2+} and [Ag$_{25}$(SR)$_{18}$]$^-$ can produce Ag$_4$Pd$_4$(SR)$_8$ with a completely different M–S framework from the parent metal NCs, while a similar reaction of [Ag$_{25}$(SR)$_{18}$]$^-$ with Pt^{2+} can only result in large-sized nanoparticles with a diameter of ~5 nm.[157] These results highlight the decisive role of metal cations in the reaction with metal NCs.

In addition to the conventional galvanic reaction, the alloying reaction can also occur through the anti-galvanic mechanism, where a more reactive metal cation can be reduced by a less reactive M(0) core of the corresponding metal NCs. For example, by reacting [Au$_{25}$(SR)$_{18}$]$^-$ with Ag$^+$, Hg^{2+}, and Cd^{2+}, a variety of bimetallic NCs, *i.e.*, [Au$_{25-x}$Ag$_x$(SR)$_{18}$]^{q},[158] Au$_{24}$-Hg(SR)$_{18}$,[85] and Au$_{24}$Cd(SR)$_{18}$,[53] respectively, can be produced without changing the M–S framework of the parent metal NCs. In contrast, the reaction of Au$_{44}$(SR)$_{28}$ with Cd^{2+} generates Au$_{47}$Cd$_2$(SR)$_{31}$, whose M–S framework is completely different from that of the parent NCs.[159] It is worth noting that by deliberately controlling the solvent and time of the reaction between [Au$_{25}$(SR)$_{18}$]$^-$ and Ag$^+$, Yao *et al.* were also able to deposit two additional Ag heteroatoms on the surface of [Au$_{25}$(SR)$_{18}$]$^-$ to produce Au$_{25}$Ag$_2$(SR)$_{18}$, which showed improved catalytic activity for the hydrolysis of 1,3-diphenylprop-2-ynyl acetate (Fig. 6a).[156] Dou *et al.* also adopted a similar surface addition strategy to enhance the luminescence of water-soluble Au$_{18}$(SR)$_{14}$ NCs.[160] In this study, foreign Ag$^+$ was introduced to bridge the Au(I)–SR motifs in the protecting shell of Au$_{18}$(SR)$_{14}$, leading to the formation of AuAg NCs with strong emission at 667 nm (λ_{ex} = 520 nm; quantum yield, QY = ~6.8%) *via* aggregation-induced emission (AIE).

Because M(I)–SR or M(II)–SR complexes have good stability and easy accessibility, they have attracted increasing interest as a source of heteroatoms for alloying NCs. Similar to metal cations, the reaction of M(I)–SR or M(II)–SR complexes with the parent metal NCs can produce a variety of alloy NCs, regardless of whether the original M–SR framework of the parent NCs is changed. For example, Wang *et al.* reported the reactions of [Au$_{25}$(SR)$_{18}$]$^-$ with Ag(I)–SR, Cu(I)–SR, Cd(II)–SR, and Hg(II)–SR complexes, to produce the alloys [Au$_{25-x}$Ag$_x$(SR)$_{18}$]$^-$,

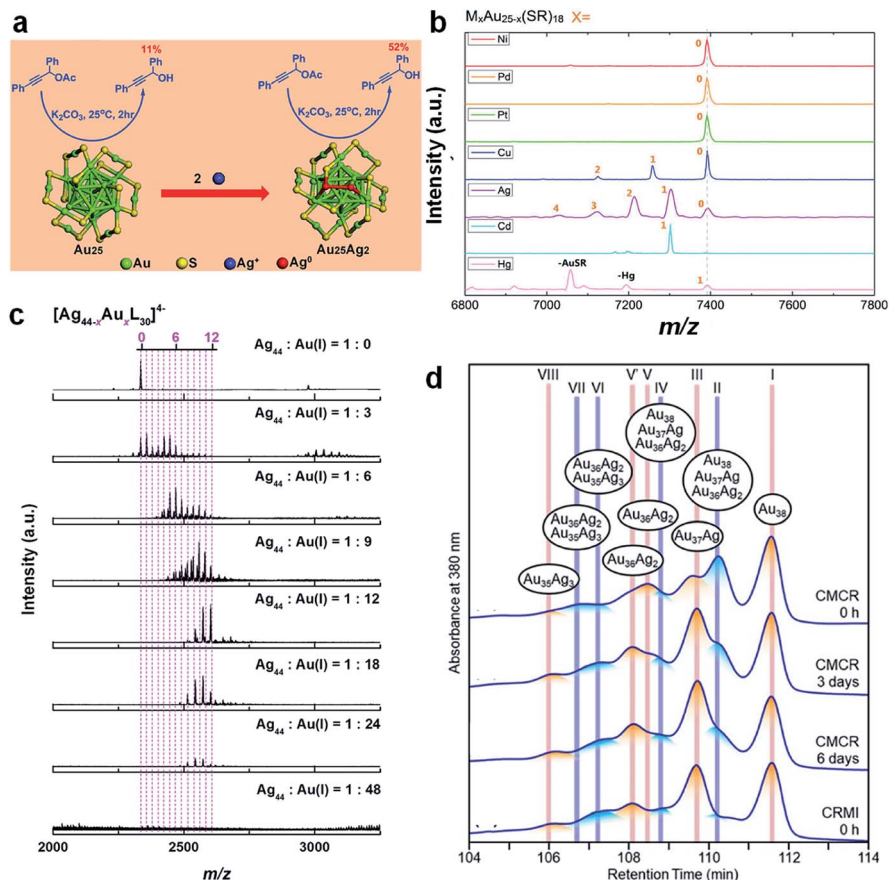**Fig. 6** (a) Schematic illustration of the formation of $Au_{25}Ag_2(SR)_{18}$ by adding two additional Ag atoms to $[Au_{25}(SR)_{18}]^-$; reproduced with permission from ref. 156. Copyright 2015, American Chemical Society. (b) ESI-MS spectra of $Au_{25-x}M_x(SR)_{18}$ formed by reacting $[Au_{25}(SR)_{18}]^-$ with the corresponding $M(I)-SR/M(II)-SR$ complexes (M = Ni, Pd, Pt, Cu, Ag, Cd, and Hg); reproduced with permission from ref. 58. Copyright 2015, American Chemical Society. (c) ESI-MS spectra of $[Ag_{44}(p\text{-MBA})_{30}]^{4-}$ reacted with $Au(I)-(p\text{-MBA})$ at different feeding ratios of $Ag_{44} : Au(I)$; L denotes the protecting ligand; reproduced with permission from ref. 60. Copyright 2017, the Authors, published by Springer Nature. (d) HPLC spectra of $Au_{38-x}Ag_x(SR)_{24}$ formed by cluster-metal complex reaction (CMCR) and co-reduction of metal ions (CRMI) at different reaction times; reproduced with permission from ref. 59. Copyright 2019, American Chemical Society.

$[Au_{25-x}Cu_x(SR)_{18}]^-$, $Au_{24}Cd(SR)_{18}$, and $Au_{24}Hg(SR)_{18}$, respectively (Fig. 6b).[58] In sharp contrast, the reaction of $[Au_{23}(SR)_{16}]^-$ with Ag(I)–SR and Cd(II)–SR complexes can initiate alloying and size growth reactions on the parent NCs, producing $[Au_{25-x}Ag_x(SR)_{18}]^-$ (ref. 161) and $Au_{20}Cd_4(SH)$ $(SR)_{19}$,[162] respectively. Due to its increasing importance in the synthetic chemistry of metal NCs, the underlying chemistry of the reaction between metal NCs and M(I)–SR or M(II)–SR complexes has been intensely pursued in the past few years. By comparing the reactions of $[Au_{25}(S\text{-}C_2H_4Ph)_{18}]^-$ with four different types of Ag(I) sources (i.e., $AgNO_3$, Ag(I)–EDTA, Ag(I)–(S-C_2H_4Ph), and Ag(I)–DTZ complexes, where EDTA and DTZ are ethyl-enediaminetetraacetic acid and dithizone, respectively), Tian et al. found that the composition and population of the product alloy NCs were highly dependent on the chelating environment of the incoming heteroatoms.[52] Yao et al. conducted detailed ESI-MS and tandem MS analysis on the reaction of $[Ag_{44}(SR)_{30}]^{4-}$ with Au(I)–SR under different feeding ratios of Ag_{44} to Au (Fig. 6c).[60] The authors revealed that up to 12 Au heteroatoms can be incorporated into the $M_{44}S_{30}$ framework through the SME mechanism described in eqn (1). More

interestingly, Zheng et al. observed the dynamic diffusion of a heteroatom (i.e., Au) inside the parent $[Ag_{25}(MHA)_{18}]^-$ at the intra-cluster level by using real-time ESI-MS and tandem MS.[163] The authors demonstrated that $[Ag_{25}(MHA)_{18}]^-$ shows considerable reactivity to Au(I)–(MHA) complexes, thus producing molecularly pure $[Ag_{24}Au(MHA)_{18}]^-$ based on a SR–Au(I)–SR unit assisted quasi-SME mechanism. By tracking the position of the Au heteroatom in $[Ag_{24}Au(MHA)_{18}]^-$ using real-time tandem MS, the authors unambiguously proved the heteroatom dynamics in the alloy NCs. Specifically, after being incorporated into the protecting motif of $[Ag_{24}Au(MHA)_{18}]^-$, the Au heteroatom will diffuse inward through the outer layer and eventually diffuse to the centre of the icosahedral M_{13} core. Such dynamics of metal atoms in the metal NCs should be taken into consideration in the further design of metal NC-based nanomaterials.

The inter-cluster reaction is a recent discovery, which provides another mechanism for the alloying of metal NCs.[65] For example, Krishnadas et al. demonstrated the inter-cluster reaction between $[Au_{25}(SR)_{18}]^-$ and $[Ag_{44}(SR)_{30}]^{4-}$ in dichloromethane (DCM), which led to the formation of both $[Au_{25-x}Ag(SR)_{18}]^-$ and $[Ag_{44-x}Au_x(SR)_{30}]^{4-}$ NCs.[64,164] The alloying

content (*i.e.*, x value) of both $[Au_{25-x}Ag(SR)_{18}]^-$ and $[Ag_{44-x}Au_x(SR)_{30}]^{4-}$ has been demonstrated to be highly dependent on the feeding ratio of $[Au_{25}(SR)_{18}]^-$ and $[Ag_{44}(SR)_{30}]^{4-}$, and nearly molecularly pure $[Ag_{32}Au_{12}(SR)_{30}]^{4-}$ can be produced by implementing an appropriate excess of $[Ag_{44}(SR)_{30}]^{4-}$ in the inter-cluster reaction. In a follow-up contribution, Baksi *et al.* investigated the kinetics of this inter-cluster reaction by time-dependent ESI-MS, mapping out the relative abundance of the individual $[Ag_{44-x}Au_x(SR)_{30}]^{4-}$ product ($x = 1–12$) in a range of m/z and reaction time.[165] More intriguingly, by using trapped ion mobility mass spectrometry (TIMS), the authors also deliberately monitored the collision cross-section change of individual $[Ag_{44-x}Au_x(SR)_{30}]^{4-}$ during the inter-cluster reaction. The TIMS results suggest that the Au heteroatom diffused from $M_2(SR)_5$ motifs all the way into the icosahedral M_{12} core of $[Ag_{44-x}Au_x(SR)_{30}]^{4-}$ after the inter-cluster collision. These findings also highlight the usefulness of mass spectrometry in revealing the reaction kinetics and dynamics of inter-cluster reactions.[166]

A similar inter-cluster reaction can also occur between $[Au_{25}(SR)_{18}]^-$ and $[Ag_{25}(SR)_{18}]^-$ to produce $[Au_{25-x}Ag_x(SR)_{18}]^-$, where the value of x can be continuously varied from 1 to 24 simply by altering the feeding ratio of parent NCs.[63] ESI-MS successfully captured an important intermediate, $[Au_{25}Ag_{25}(SR)_{36}]^{2-}$, which indicates that the inter-cluster reaction is likely to occur through a dimerization mechanism. Combined molecular docking and DFT calculations elucidate that the dimerization is made possible most likely by an inter-cluster Ag–S bond. This mechanism is also in line with the observation of Zhang *et al.*, where the inter-cluster reaction between $Au_{38}(SR)_{24}$ and $Au_{38-x}Ag_x(SR)_{24}$ can be completely terminated through physical separation of these two NCs by a dialysis membrane (molecular weight cut-off, MWCO = 1000 Da).[167] Recently, Niihori *et al.* showed that the inter-cluster reaction might occur among a mixture of $Au_{38-x}Ag_x(SR)_{24}$ NCs ($x = 0–3$), even after the apparent abundance of $Au_{38-x}Ag_x(SR)_{24}$ NCs remained stable in the ESI-MS spectra.[59] The authors prepared $Au_{38-x}Ag_x(SR)_{24}$ ($x = 0–3$) NCs by mixing $Au_{38}(SR)_{24}$ with Ag(I)–SR complexes in DCM for 1 min. ESI-MS analysis showed that the population abundance of $Au_{38-x}Ag_x(SR)_{24}$ ($x = 0–3$) remained unchanged within 6 days after synthesis. However, when these ESI-MS identical samples were checked by HPLC, they showed different retention profiles, which largely depended on the incubation time after synthesis (Fig. 6d). This discrepancy is attributed to the inter-cluster reaction between the newly formed $Au_{38-x}Ag_x(SR)_{24}$ ($x = 0–3$) NCs. This reaction can generate not only composition isomers, but also structural isomers in the elution column of HPLC.

In addition to the inter-cluster reaction, alloy NCs can also be produced by reacting metal NCs with bulk metals. For example, Kazan *et al.* obtained alloy $[Au_{25-x}Ag_x(SR)_{18}]^-$, $[Au_{25-x}Cu_x(SR)_{18}]^-$, and $Au_{24}Cd(SR)_{18}$ by incubating $[Au_{25}(SR)_{18}]^-$ in the presence of bulk Ag, Cu, and Cd foil, respectively.[168] The similar reaction of $Au_{38}(SR)_{24}$ with Ag and Cu foil can produce $Au_{38-x}Ag(SR)_{24}$ and $Au_{38}Cu(SR)_{24}$, respectively, while incubating $Au_{38}(SR)_{24}$ with Cd foil cannot induce any alloying reaction.[168]

High quality bimetallic NCs fabricated by the delicate chemistry discussed above can also be employed as parent NCs for controlled production of trimetallic and tetrametallic NCs.[169,170] Bootharaju *et al.* reacted bimetallic $[Ag_{24}Pt(SR)18]^{2-}$ with Au^+, giving rise to $[Ag_{24-x}PtAu_x(SR)_{18}]^{2-}$ ($x = 1–2$).[171] However, a similar reaction between $[Ag_{24}Pd(SR)_{18}]^{2-}$ and Au^+ could only lead to the formation of intermediate $[Ag_{24-x}PdAu_x(SR)_{18}]^{2-}$ ($x = 1–2$) with a limited lifetime, which was ultimately transformed into stable $[Ag_{25-x}Au_x(SR)_{18}]^{2-}$.[171] Mixing $Au_{24}M(SR)_{18}$ (M = Hg/Pd) and Ag(I)–SR complexes can inevitably produce $Au_{24-x}MAg_x(SR)_{18}$.[172,173] The crystal structure of $Au_{24-x}HgAg_x(SR)_{18}$ has been resolved, showing that the Ag heteroatoms prefer the vertex sites of the icosahedral M_{13} core.[172] Moreover, the as-produced trimetallic $Au_{24-x}PdAg_x(SR)_{18}$ has also been utilized as a starting cluster, and its reaction with Cu–SR complexes was used to synthesize tetrametallic $Au_{24-x-y}PdAg_xCu_y(SR)_{18}$.[173] In a recent contribution, Khatun *et al.* demonstrated inter-cluster reaction as another feasible approach for the production of trimetallic metal NCs, where the reaction between $[Ag_{28}M(BDT)_{12}(PPh_3)_4]^{4-}$ (M = Ni, Pd and Pt) and $[Au_{25}(S-C_2H_4Ph)_{18}]^-$ resulted in a mixture of $[Ag_{28-x}MAg_x(BDT)_{12}(PPh_3)_4]^{4-}$ ($x = 1–12$) and $[Au_{25-x}Ag_x(S-C_2H_4Ph)_{18}]^-$ ($x = 1–7$).[174] It is worth noting that the central M atom and protecting ligands of $[Ag_{28}M(BDT)_{12}(PPh_3)_4]^{4-}$ remain unchanged throughout the inter-cluster reaction, highlighting the decisive impact of the central M atom and BDT ligand on the cluster stability of $[Ag_{28}M(BDT)_{12}(PPh_3)_4]^{4-}$.

3.3. Molecular interactions/reactions in ligand exchange of metal NCs

The ligand exchange of metal NCs represents one of the most intensively studied reactions in cluster chemistry.[3,4,111,175] The ligand exchange reaction is usually induced by introducing a designed amount of foreign thiols (HSR′) into the parent $[M_n(SR)_m]^q$ NCs, and recent progress in the surface engineering of metal NCs suggests that the source of foreign thiol ligands can be diverse (*e.g.*, M(I)–SR′ complexes or $[M_n(SR′)_m]^q$ NCs). Owing to the well-controlled kinetics and thermodynamics through a proper selection of the original SR and the incoming SR′ ligands, ligand exchange reactions have been widely used to fine-tune the surface chemistry of metal NCs, and they can also adjust the size and atom packing patterns of metal NCs.[111]

As a rule of thumb, at low doses, reacting $[M_n(SR)_m]^q$ NCs with the foreign HSR′ with a structure similar to that of SR tends to produce metal NCs protected by mixed ligands without changing the M–S framework of the parent NCs. For example, Murray and co-workers performed ligand exchange reactions on $[Au_{25}(S-C_2H_4Ph)_{18}]^-$ with different incoming thiol ligands, including HS-$(CH_2CH_2O)_5CH_3$, HS-$(CH_2CH_2O)CH_3$, HS-$(CH_2)_5CH_3$, and toluene-3,4-dithiol $((SH)_2PhCH_3)$, leading to the formation of mixed-ligand-protected Au_{25} NCs.[176,177] Although the tested monodentate ligands showed very little preference for the exchange sites of the thermodynamic products (obtained at prolonged reaction time), the bidentate $(SH)_2PhCH_3$ showed preference for bridging Au(I) atoms from the adjacent SR–[Au(I)–SR]$_2$ motifs. Similarly, monodentate (*e.g.*, HS-Ph) and bidentate

(*e.g.*, 1,1′-binaphthyl-2,2′-dithiol or BINAS) thiols have also been used as foreign ligands to react with $Au_{38}(S-C_2H_4Ph)_{24}$, generating inhomogeneity in the protecting shell of Au_{38} NCs.[57] In addition to the above-mentioned partial ligand exchange scenarios, the ligand exchange reaction can also be carried out on the surface of metal NCs till completion. The complete ligand exchange reaction usually involves native SR and incoming HSR′, which differ greatly in structure and solubility. For example, AbdulHalim *et al.* designed a simple method to engineer the surface properties of $[Ag_{44}(SR)_{30}]^{4-}$ NCs based on a complete ligand exchange reaction.[178] $[Ag_{44}(MNBA)_{30}]^{4-}$ (MNBA = 5-mercapto-2-nitrobenzoic acid) was synthesized in an aqueous solution, followed by introduction of a DCM/ethanol (1/1 vol/vol) solution of the desired aryl thiols (*e.g.*, HS-Ph-*p*-F, HS-Ph-*p*-NO_2, and 2-naphthalenethiol). In this two-phase setup, the ligand exchange reaction can be completed within 30 s, accompanied by the total phase transfer of Ag_{44} NCs from the aqueous phase to the organic phase. A similar phase-transfer-assisted complete ligand exchange was also reported on $Au_{18}(SR)_{14}$ NCs, in which a complete ligand exchange from GSH to cyclohexanethiol (HS-*c*-C_6H_{11}) was observed.[90]

Another attractive feature of the ligand exchange reaction is its ability to change the M–S framework of metal NCs. By conducting ligand exchange reaction with a structurally and electronically different incoming thiol ligand at an elevated temperature, the size and structure transformation of metal NCs are likely to be evoked. In the past two decades, this ligand exchange induced size/structure transformation (LEIST) strategy has achieved great success in the synthetic chemistry of metal NCs.[3,111] For example, Zeng *et al.* treated $[Au_{25}(S-C_2H_4Ph)_{18}]^-$ with HS-Ph-*p*-^tBu at 80 °C for 2 h, which converted the icosahedral Au_{13} core based $[Au_{25}(S-C_2H_4Ph)_{18}]^-$ into the FCC Au_{20} core based $Au_{28}(S-Ph-p-^tBu)_{20}$.[179] Eswaramoorthy *et al.* synthesized $Au_{279}(S-Ph-p-^tBu)_{84}$ by reacting $Au_{329}(S-C_2H_4Ph)_{84}$ with excess HS-Ph-*p*-^tBu at 80 °C for 6 days.[180] Time-course ESI-MS analysis suggests that this LEIST reaction occurs by following a three-stage mechanism: initial ligand exchange → core size conversion → complete ligand exchange. This three-stage LEIST mechanism is completely consistent with previous observations in the size transformation reaction from $Au_{38}(S-C_2H_4Ph)_{24}$ to $Au_{36}(S-Ph-p-^tBu)_{24}$.[66] It is worth noting that the LEIST reaction can be reversible since the size of the stable clusters is closely related to the structure of SR ligands. For example, Bootharaju *et al.* demonstrated a reversible size conversion between $[Ag_{44}(p-MBA)_{30}]^{4-}$ and $[Ag_{25}(S-PhMe_2)_{18}]^-$ (HS-$PhMe_2$ = 2,4-dimethylbenzenethiol) by a LEIST reaction in a two phase system (water/DCM), while a similar LEIST reaction can be performed in a one phase system (DCM) for inter-conversion between $[Ag_{44}(S-Ph-p-F)_{30}]^{4-}$ and $[Ag_{25}(S-PhMe_2)_{18}]^-$.[67] Similar ligand exchange induced reversible size conversions have also been reported on $[Ag_{44}(S-Ph-p-F)_{30}]^{4-}$/$Ag_{35}(SG)_{18}$ (ref. 181) and $Au_{30}(S-^tBu)_{18}$/$Au_{36}(S-Ph-p-X)_{24}$ (X = H or ^tBu).[182]

In addition to the size-*cum*-structure transition discussed above, ligand exchange may also induce a quasi-isomerization reaction, in which the cluster size (*i.e.*, the value of *n* and *m* in $[M_n(SR)_m]^q$) remains unchanged, while the atomic packing pattern varies. For example, Chen *et al.* obtained $Au_{28}(S-c-C_6H_{11})_{20}$ by thermal treatment (at 80 °C) of $Au_{28}(S-Ph-p-^tBu)_{20}$ in the presence of excess HS-*c*-C_6H_{11}.[183] These two $Au_{28}(SR)_{20}$ NCs have a similar FCC Au_{20} core capped by eight bridging SR ligands. However, the Au(I)–SR motifs are different in these two quasi-isomers. $Au_{28}(S-c-C_6H_{11})_{20}$ has two trimeric SR–[Au(I)–SR]$_3$ and two monomeric SR–Au(I)–SR motifs, while $Au_{28}(S-Ph-p-^tBu)_{20}$ has four dimeric SR–[Au(I)–SR]$_2$ motifs. More interestingly, $Au_{28}(S-c-C_6H_{11})_{20}$ can be converted back to $Au_{28}(S-Ph-p-^tBu)_{20}$ by a similar ligand exchange process under thermal treatment (at 80 °C).[183] DFT calculations suggest that the driving force for this reversible quasi-isomerization reaction is the balance between DFT energy and van der Waals contribution.

Due to the limited content, many noteworthy achievements on this topic cannot be included in this *Review*. We apologize for this and would like to refer interested readers to several well-written reviews published elsewhere.[3,111,184,185]

4. Molecular interactions/reactions in post-synthesis development of metal NCs

In the past two decades, the prosperity and development of synthetic chemistry has enabled a great variety of atomically precise metal NCs with customizable size, composition, structure, and surface chemistry, forming a library of functional building blocks for self-assembly and practical application exploration.[3–5,7,8] The self-assembly and practical application exploration of metal NCs also highly depends on the interactions/reactions of metal NCs with ions, molecules, and other metal NCs, which will be discussed in this section.

4.1. Molecular interactions/reactions in self-assembly of metal NCs

Self-assembly provides an alternative method to customize or enhance the materials properties and performance of metal NCs through the collective and synergistic effects of adjacent NCs in the assembly, which can be fabricated in different sizes, morphologies, symmetries, and orders.[106,108,128–131,186] Since the self-assembly process of metal NCs is mainly governed by either the inter-cluster interactions/reactions or clusters' interactions/reactions with the cross-linker ions/molecules, superstructures with 1D, 2D and 3D configurations have been constructed based on metal NCs by deliberately controlling such interactions/reactions.

Oligomerization can be considered as the 1D self-assembly of metal NCs. For example, Pradeep and co-workers captured a dimer of $[Au_{25}(S-C_2H_4Ph)_{18}]^-$ and $[Ag_{25}(S-PhMe_2)_{18}]^-$ as the intermediate of inter-cluster reaction between these two NCs.[63] Their computational calculations suggest that this dimerization is achieved likely through the interdigitation (*e.g.*, van der Waals interactions) of ligands and inter-cluster Ag–S bonds. Very recently, foreign Ag^+ has also been employed as a cross-linker to combine two isolated $[Au_{25}(S-C_2H_4Ph)_{18}]^-$ together and produces atomically precise $Ag_2Au_{50}(S-C_2H_4Ph)_{36}$ (Fig. 7a), where a single Ag is accommodated in the pocket-like cavity of
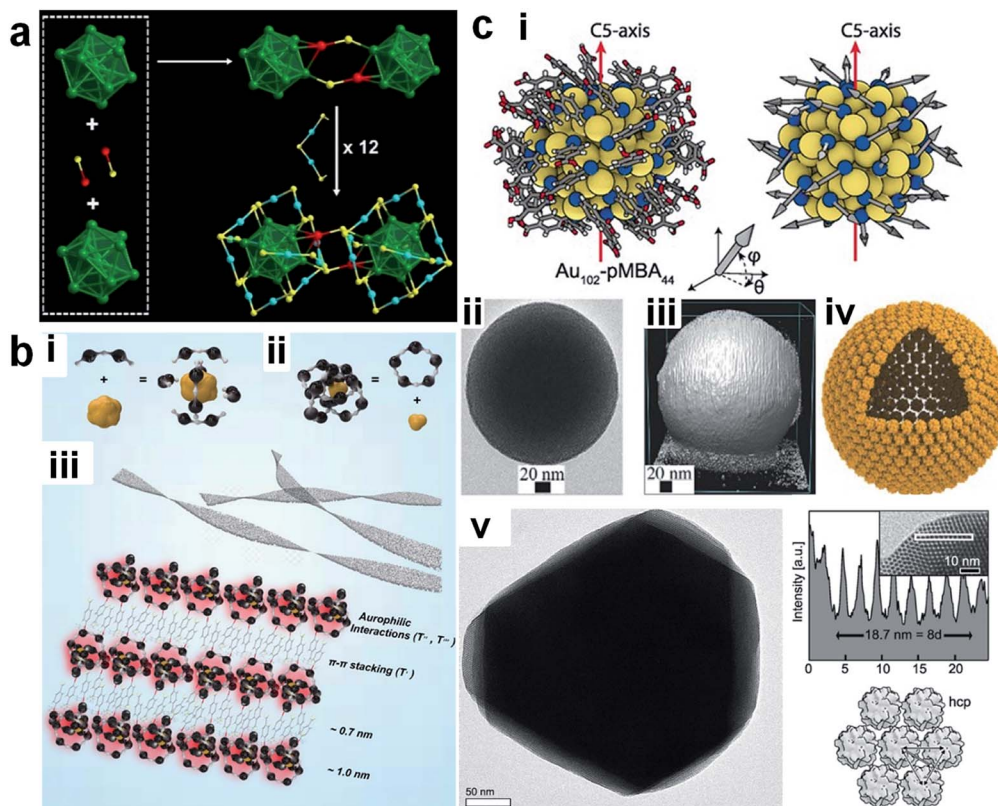
Fig. 7 (a) Schematic illustration of the dimerization of $[Au_{25}(SR)_{18}]^-$ through bridging Ag atoms to form $Ag_2Au_{50}(SR)_{36}$ (colour code: green, core Au(0); cyan, motif Au(I); yellow, S; red, Ag); reproduced with permission from ref. 187. Copyright 2020, Wiley-VCH. (b) Schematic illustration of the formation of nanoribbons by inter-cluster aurophilic interactions between Au NCs: structural anatomy of $[Au_{25}(SR)_{18}]^-$ (i), smaller-sized Au NCs formed by surface rearrangement of $[Au_{25}(SR)_{18}]^-$ (ii) and their self-assembly into nanoribbons (iii) (colour code: golden, core Au(0); black, motif Au(I); light grey, S; reproduced with permission from ref. 108. Copyright 2019, Wiley-VCH. (c) Structural model of partially protonated $Au_{102}(p\text{-}MBA)_{44}$ (i); TEM image (ii), electron tomographic model (iii), and cartoon structural model (iv) of spherical capsids formed by $Au_{102}(p\text{-}MBA)_{44}$; TEM image of hexagonal close packed (HCP) layered architectures formed by $Au_{102}(p\text{-}MBA)_{44}$ (v); the arrows in (i) indicate the orientations of p-MBA ligands; the insets of (v) are the high resolution TEM image (top panel) and packing model (bottom panel) of HCP layered architectures; reproduced with permission from ref. 128 and 189. Copyright 2016 and 2017, respectively, Wiley-VCH.

$[Au_{25}(S\text{-}C_2H_4Ph)_{18}]^-$, forming a Ag–S bond with another NC.[187] In addition to M–S bonds, dimerization and trimerization can also be achieved by introducing dithiolate ligands as cross-linkers.[188] For example, Lahtinen *et al.* carried out a ligand exchange of $Au_{102}(p\text{-}MBA)_{44}$ with bidentate biphenyl-4,4′-dithiols (SH–Ph–Ph–SH), which covalently linked Au_{102} NCs into dimers or trimers.[188]

In addition to the aforementioned covalent bonds, metal-lophilic interactions have also been proven to be effective in controlling the self-assembly of metal NCs into 1D architectures. As shown in Fig. 3a, $Au_{25}(S\text{-}^nBu)_{18}$ NCs can be organized into 1D nanowires in their single crystals, through inter-cluster aurophilic interactions.[106] This 1D configuration also changed their magnetic response from paramagnetic (in the isolated state) to antiferromagnetic (in the assembled state). Wu *et al.* also demonstrated the effectiveness of aurophilic interactions in directing the 1D self-assembly of Au NCs.[108] $[Au_{25}(p\text{-}MBA)_{18}]^-$ NCs were subjected to a cyclic dialysis treatment in water, which slightly disturbed the surface structure of NCs and enriched long Au(I)–SR motifs in their protecting shell. The abundant Au(I) sites and enhanced

flexibility of such long Au(I)–SR motifs form the structural basis for the anisotropic aurophilic interactions between adjacent NCs, thereby promoting their assembly into 1D nanoribbons (Fig. 7b). It is worth noting that the extensive inter-cluster aurophilic interactions in the generated nanoribbons also provide additional radiative relaxation pathways for excited electrons, which contributes to the two-orders-of-magnitude improvement in the cluster emission. A similar aurophilic interaction is also observed in the 1D self-assembly of $Au_4Pt_2(SR)_8$.[130] It should be mentioned that the regular 1D arrangement is a complex undertaking, typically involving more than one type of inter-cluster interaction. For example, through the above success, the close contact between the component NCs required by significant aurophilic interactions (<3.6 Å) is made possible by anisotropic rearrangement of the hydrocarbon tails of the SR ligands, manifesting van der Waals interactions, π–π interactions, and dipole–dipole interactions among the component NCs.[106,108,130]

Metal NCs have also been arranged into 2D architectures by amphiphilicity,[129] van der Waals interactions,[131] and H-bonds.[128,189] As discussed in a previous section, amphiphilicity can be

introduced into $Au_{25}(MHA)_{18}$ NCs through a phase-transfer-driven ion-pairing reaction with CTA^+ (Fig. 4b).[129] The as-produced amphiphilic $Au_{25}(MHA)_{18}@xCTA$ ($x = 6–9$) NCs are able to organize themselves into regularly stacked bilayers at the air–liquid interface, which is reminiscent of the formation of a lyotropic liquid crystalline phase by molecular amphiphiles. Au_{15} NCs protected by $–S-C_{12}H_{25}$ have also been assembled into mono-, few- and multi-layered 2D superstructures in both mono-solvent (e.g., dibenzyl ether)[131] and dual-solvent (e.g., dibenzyl ether/liquid paraffin, 1/7.5 vol/vol)[192] systems, largely leveraging on the van der Waals interactions of $–S-C_{12}H_{25}$ ligands between adjacent NCs. Rival et al. developed a light-triggered strategy for stacking thiolated azobenzene-protected Au_{25} NCs into disk-like superstructures, where light-switchable dipole–dipole interactions of azobenzene govern the self-assembly behaviour of NCs.[193] Moreover, H-bonds have also been employed by Nonappa et al. for packing $Au_{102}(p\text{-MBA})_{44}$ into 2D nanosheets, which can be further bent into spherical capsids or stacked into faceted multi-layers (Fig. 7c).[128] By directly adding an aqueous solution of $Au_{102}(p\text{-MBA})_{44}$ into methanol, the $–COO^-$ group of the p-MBA ligand can be partially protonated. This partial protonation will further induce preferential inter-cluster H-bonds within the equatorial plane of NCs according to the anisotropic distribution of p-MBA ligands on the surface of $Au_{102}(p\text{-MBA})_{44}$ (panel (i), Fig. 7c), leading to the formation of spherical capsids with a monolayer of NCs as the shell. By changing the way of introducing the bad solvent (i.e., methanol) from direct mixing to controlled dialysis, the authors were also able to obtain regularly stacked HCP layers of $Au_{102}(p\text{-MBA})_{44}$, reminiscent of the layered structure of graphite.

In addition to the 2D architectures, 3D supercrystals can also be produced based on the extensive H-bonds among the component metal NCs.[12,190] For example, the fully protonated $[Ag_{44}(p\text{-MBA})_{30}]^{4-}$ NCs have been crystallized into a triclinic superlattice in DMF solution (Fig. 8a).[12] X-ray crystallography examination suggests that the protonated p-MBA ligands were bundled together into two different patterns, namely a double-bundle containing two p-MBA ligands and a triple-bundle involving three p-MBA ligands (Fig. 8b).[12,190] These different bundle patterns of p-MBA ligands determine the inter-cluster H-bonding within and between the crystalline layers. As illustrated in Fig. 8b, NCs in the same crystalline layer are connected by the double-bundles and those in adjacent crystalline layers are connected by the triple-bundles. In this way, an individual NC is connected to other NCs through 60 H-bonds (each p-MBA contributes 2 H-bonds), thus forming a cohesive H-bond network within the NC supercrystals. More interestingly, this cohesive H-bond network endows NC supercrystals with a unique mechanical response, in which NCs in adjacent crystalline layers can rotate in opposite directions upon compression (Fig. 8c). Given that the triclinic supercrystals of $[Ag_{44}(p\text{-MBA})_{30}]^{4-}$ are dominated by H-bonds, Yao et al. envisioned that the crystallization behaviour of $[Ag_{44}(p\text{-MBA})_{30}]^{4-}$ might be changed by removing the directional H-bonds.[191] The authors thereby deprotonated the p-MBA ligands by CsOH in a mixture of dimethyl sulfoxide (DMSO) and water, and crystallized $[Ag_{44}(p\text{-MBA})_{30}]^{4-}$ into FCC supercrystals with well-defined octahedral morphology by entropy effects. More importantly,

by changing the ionic strength and solvent polarity in the dual-solvent crystallization system, the authors were able to fine-tune the crystallization kinetics of $[Ag_{44}(p\text{-MBA})_{30}]^{4-}$ and shape the obtained supercrystals from an octahedron to a concave octahedron (Fig. 8d).

Besides H-bonds and entropy effects, π interactions (e.g., $\pi–\pi$ and $CH–\pi$ interactions) are another type of interaction most involved in metal NC crystallization research. This is most probably due to their effectiveness in inducing aesthetic and hierarchical molecular packing patterns at the intra- and inter-cluster levels, which helps to maximize the inter-cluster bindings among the supercrystals.[9,15,17,55] A good example of this aesthetic and hierarchical arrangement of SR ligands is the herringbone-like arrangement of naphthalene rings through $CH–\pi$ or $\pi–\pi$ interactions in the supercrystals of $Au_{103}S_2(S\text{-Nap})_{41}$ NCs (Fig. 4c), which has been detailed in Section 2.3.[55] In addition to $Au_{103}S_2(S\text{-Nap})_{41}$ NCs, similar highly symmetric and aesthetic ligand patterns packed by $CH–\pi$ and/or $\pi–\pi$ interactions have been increasingly observed in large-sized metal NCs, including $Au_{52}Cu_{72}(S\text{-Ph-}p\text{-CH}_3)_{55}$ (ref. 17) and $Au_{246}(S\text{-Ph-}p\text{-CH}_3)_{80}$.[15] As shown in Fig. 8e, in the triclinic supercrystal of $Au_{52}Cu_{72}(S\text{-Ph-}p\text{-CH}_3)_{55}$ NCs, a triangular mosaic pattern of $HS\text{-Ph-}p\text{-CH}_3$ packed through the intra- and inter-cluster $CH–\pi$ interactions (blue and yellow dashed lines, respectively) has been identified. More interestingly, the intra-cluster $CH–\pi$ interactions all come from methyl H, while the inter-cluster ones are uniformly composed of phenyl ring H. It should be noted that besides $CH–\pi$ and $\pi–\pi$ interactions, the inter-cluster van der Waals interactions also help to stabilize the supercrystals of metal NCs.[15] Similar to the DNA-assisted crystallization of metal nanoparticles,[194–196] the crystallization of thiolate-protected noble metal NCs seems to occur via maximizing the attractive ligand interactions (e.g., van der Waals, $CH–\pi$, and $\pi–\pi$ interactions) between adjacent NCs.[15]

Other than the template-free self-assembly, the arrangement of metal NCs can also be templated by larger-sized nano-materials. For example, Chakraborty et al. assembled $[Ag_{44}(p\text{-MBA})_{30}]^{4-}$ around p-MBA protected Au nanorods (Au NRs) with a length of ~30 nm and a width of ~10 nm.[186] The preferential anchoring of $[Ag_{44}(p\text{-MBA})_{30}]^{4-}$ on the <110> facets of Au NRs via H-bonds was suggested to trigger the self-assembly of $[Ag_{44}(p\text{-MBA})_{30}]^{4-}$, ultimately giving rise to a core-in-cage octahedral architecture of $Au NR@Ag_{44}$ NCs. In sharp contrast to Au NR directed self-assembly of $[Ag_{44}(p\text{-MBA})_{30}]^{4-}$ NCs, the self-assembly behaviour of Te nanowires (NWs) can be modulated by $[Ag_{44}(p\text{-MBA})_{30}]^{4-}$ NCs.[197] By modifying the surface of Te NWs with an optimized amount of $[Ag_{44}(p\text{-MBA})_{30}]^{4-}$ NCs, Te NWs could be packed into 81°-crossed bilayers. As indicated by the authors' computational study, the near-orthogonal bilayer arrangement of Te NWs is driven by maximizing H-bonds of $[Ag_{44}(p\text{-MBA})_{30}]^{4-}$ NCs from the neighbouring Te NWs.

4.2. Molecular interactions/reactions in sensing applications of metal NCs

Due to their unique molecular structures and environmentally sensitive physicochemical properties (e.g., strong
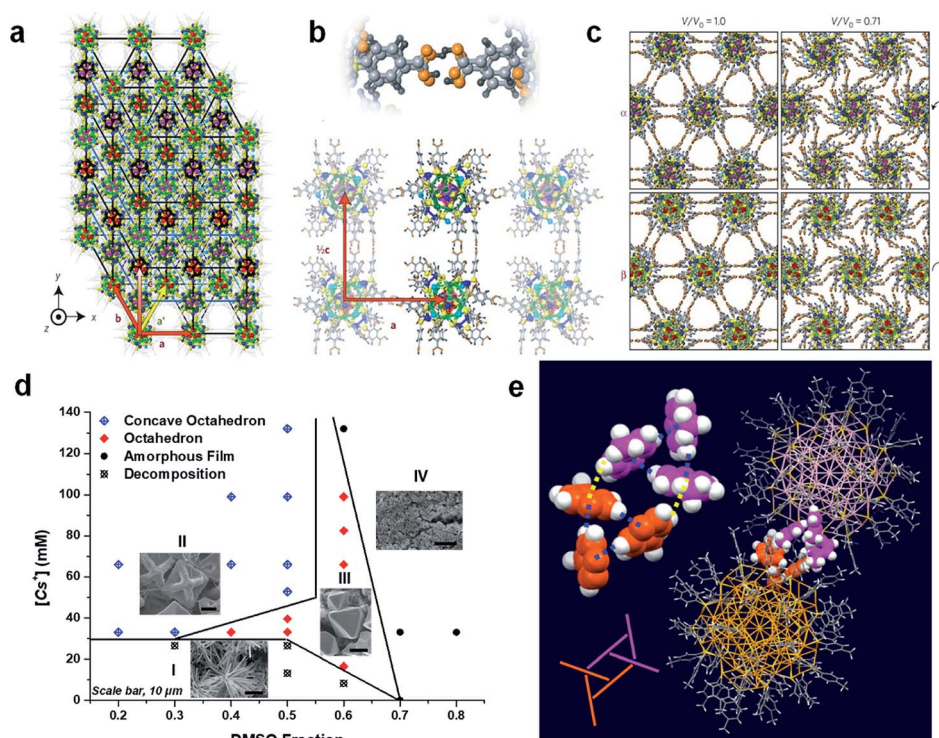
Fig. 8 (a) Packing structure, (b) H-bonds, and (c) mechanical response of protonated $[Ag_{44}(p\text{-MBA})_{30}]^{4-}$ in its triclinic supercrystals; the top panel in (b) illustrates H-bonds in a typical double-bundle of p-MBA ligands, while the bottom panel exhibits H-bonds within (horizontal direction) and between (vertical direction) the crystalline layers; V and V_0 in (c) are the volume and initial volume of supercrystals, respectively; (a)–(c) are reproduced with permission from ref. 190. Copyright 2014, Springer Nature. (d) Formation diagram of the octahedral and concave-octahedral supercrystals by deprotonated $[Ag_{44}(p\text{-MBA})_{30}]^{4-}$ in a range of Cs^+ concentrations and dimethyl sulfoxide (DMSO) fractions in the crystallization solution; reproduced with permission from ref. 191. Copyright 2015, Wiley-VCH. (e) Schematic illustration of intra- (blue dashed lines) and inter-cluster (yellow dashed lines) CH−π interactions between two $[Au_{52}Cu_{72}(S\text{-Ph-}p\text{-CH}_3)_{55}]^+$ NCs approaching in an edge-to-edge fashion in their supercrystals, where a triangular mosaic pattern of −S-Ph-p-CH$_3$ ligands can be identified (colour code: pink/golden, Au/Cu; yellow, S; grey/magenta/orange, C; light grey, H); reproduced with permission from ref. 17. Copyright 2020, the Authors, published by Springer Nature.

luminescence), metal NCs have gained marked acceptance in sensing applications.[30,198] The development of sensors relies heavily on the interactions/reactions of analytes with the metal NCs, which may cause measurable changes in the properties of the clusters. Based on the reactivity of metal NCs to selected ions, small molecules, and biomolecules, metal NCs have long been used as active probes for detecting and monitoring these species in the biomedical and environmental fields.[30,199]

By using metal NCs as optical probes, various cations (e.g., Ag^+,[200] Hg^{2+},[46,47,201,202] Cu^{2+},[203–206] Pb^{2+},[202,207–209] Pt^{2+},[208,210] Au^{3+},[208,211] Al^{3+},[212] and As^{3+})[213] and anions (e.g., CN^- (ref. 45) and S^{2-})[214] can be detected. Among the above-mentioned metal cations, Hg^{2+} has attracted great attention due to its high toxicity and diverse interactions with metal NCs. For example, Xie et al. first demonstrated the metallophilic interactions between Hg^{2+} and Au(ɪ) in a red-emitting Au NC protected by bovine serum albumin (BSA), and developed a luminescent "turn-off" sensor for Hg^{2+} detection.[46] The strong and unique $Hg^{2+}\cdots$Au(ɪ) interactions make the Au NC-based luminescent probes highly selective (against 15 other cations, including Cd^{2+}, Pb^{2+}, and Fe^{3+}) and sensitive (with a limit of detection (LOD) of 0.5 nM). Similar metallophilic interactions have also been documented between Hg^{2+} and Ag(ɪ) provided by

$Ag_{12}(SG)_{10}$ (Fig. 9a–c), whose blue emission centred at 435 nm ($\lambda_{ex} = 350$ nm) can be sensitively quenched by Hg^{2+}.[47] By using $Ag_{12}(SG)_{10}$ at a concentration of 1 nM, it can provide a LOD of 0.1 nM with a good selectivity against interfering cations (e.g., Cd^{2+}, Pb^{2+}, and Fe^{3+}) (Fig. 9d). In addition to the metallophilic interaction with M(ɪ), Hg^{2+} can also be detected by forming Hg–S bonds and ion pairs with the SR ligands of metal NCs.[208,215]

Besides the above-mentioned interactions, another notable reaction that can be used for cation detection is the redox reaction between metal NCs and cations. For example, Wu et al. found that an aqueous solution of $[Au_{25}(SG)_{18}]^-$ had an increase in luminescence of 3.4 fold ($\lambda_{em} = 670$ nm; $\lambda_{ex} = 514$ nm) upon the addition of Ag^+. This luminescence enhancement is mainly attributed to the oxidation of $[Au_{25}(SG)_{18}]^-$ by Ag^+.[200] A prototype "turn-on" luminescent sensor for Ag^+ detection can be developed based on this mechanism, delivering a LOD of 200 nM and good selectivity against 19 other cations, including Cd^{2+}, Hg^{2+}, and Cu^{2+}. It should be mentioned that redox reaction could also occur between $[Au_{25}(SG)_{18}]^-$ and Au^{3+}, leading to decomposition of the former into Au(ɪ)–SG complexes.[211] The fast decomposition kinetics (within minutes) may provide a good means for Au^{3+} detection. Similarly, chemical reduction of Cu^{2+} by $Au_{15}(SG)_{13}$ has been registered by George et al., based on which
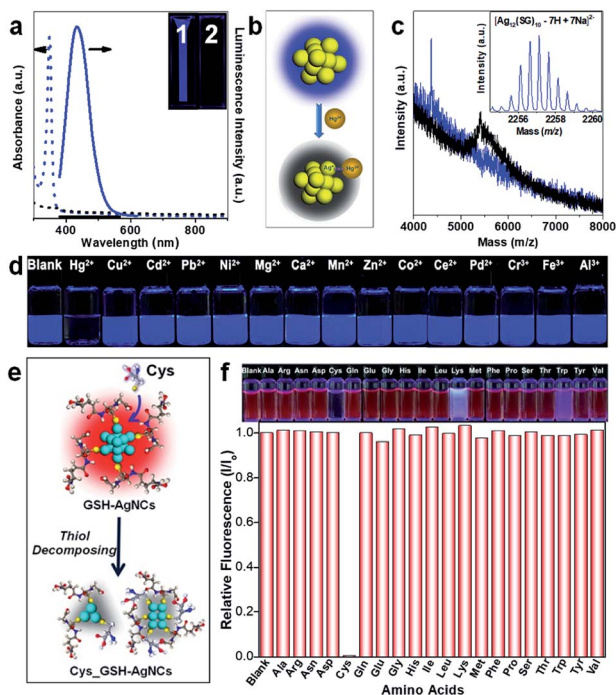
Fig. 9 (a) UV-vis absorption (dotted lines) and emission (solid lines, λ_{ex} = 350 nm) spectra of $Ag_{12}(SG)_{10}$ in the presence (black lines) and absence (blue lines) of Hg^{2+}; insets are digital photos of $Ag_{12}(SG)_{10}$ in the presence (#2) and absence (#1) of Hg^{2+} under UV light; (b) schematic illustration of the metallophilic interaction between Hg^{2+} and $Ag_{12}(SG)_{10}$ that can quench cluster luminescence; (c) matrix-assisted laser desorption/ionization (MALDI) mass spectra of $Ag_{12}(SG)_{10}$ in the presence (black line) and absence (blue line) of Hg^{2+}; (d) digital photos of $Ag_{12}(SG)_{10}$ in the presence of varied metal cations under UV light (365 nm); (a)–(d) are reproduced with permission from ref. 47. Copyright 2012, Royal Society of Chemistry. (e) Schematic illustration of the detection mechanism of cysteine (Cys) by $Ag_{16}(SG)_9$ NCs; (f) relative emission intensity and digital photos of $Ag_{16}(SG)_9$ NCs in the presence of 20 natural amino acids; reproduced with permission from ref. 216. Copyright 2012, American Chemical Society.

the authors devised a free-standing $Au_{15}(SG)_{13}$-coated chitosan film for sensitive Cu^{2+} detection.[209]

In contrast to the diverse interactions/reactions suitable for cation detection, the documented successes of anion detection mainly depend on the core etching reaction of the metal NCs induced by the reactive anions. For example, CN^- can exert a strong etching effect on the Au(0) core of Au NCs through the well-known Elsner reaction (eqn (9)).

$$4Au + 8CN^- + 2H_2O + O_2 \rightarrow 4[Au(CN)_2]^- + 4OH^- \quad (9)$$
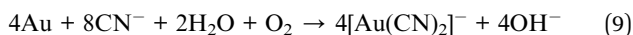
Based on this reaction, Lu et al. developed a luminescent sensor using BSA-protected Au NCs, which emit bright red light at 640 nm (λ_{ex} not specified).[45] After adding CN^-, this red emission can be quickly and effectively quenched at the optimized pH of 12.0. A reliable selectivity was demonstrated against 15 interfering anions (e.g., SCN^-, $EDTA^{2-}$, and F^-) and 16 cations (e.g., Mg^{2+}, Ba^{2+}, and Al^{3+}), while the LOD was determined to be 200 nM. A similar strong core etching effect has been documented for S^{2-} toward Ag NCs, based on which

a "turn-off" luminescent sensor has been developed by using $Ag_{12}(SG)_{10}$ as a luminescent probe.[214]

In addition to anions, the core etching reaction can also be induced by small molecules such as thiols. For example, Yuan et al. developed a "turn-off" luminescent sensor for sensitive detection of cysteine (Cys), which is a naturally occurring thiol-containing amino acid.[216] The metal NCs used are mainly $Ag_{16}(SG)_9$ NCs, which emit strong red light at 647 nm (λ_{ex} = 489 nm). Upon reacting with Cys (Fig. 9e), $Ag_{16}(SG)_9$ NCs decomposed into smaller NCs or Ag(I)–SR complexes such as $Ag_8(SG)_4(Cys)_2$, $Ag_6(SG)_3(Cys)_3$, $Ag_3(SG)_2(Cys)_1$, and $Ag_3(SG)_3$, thereby reducing red emission and delivering a LOD of 3 nM. Due to the lack of thiol group in the other 19 naturally occurring amino acids, a good selectivity of Cys has been achieved (Fig. 9f). The most interesting finding is the good selectivity of Cys against the thiol-containing tri-peptide GSH. This should be attributed to the size effects of the analytes, where the large GSH cannot penetrate the protecting shell of $Ag_{16}(SG)_9$, thus inhibiting its etching reaction with the Ag(0) core. Other than the core etching reaction, the detection of small molecules can also be achieved by the redox reaction with metal NCs. H_2O_2 is a common oxidative molecular species detected by this method. For example, Guan et al. developed a $Zn(OH)_2$-assisted co-precipitation method to separate BSA-protected Au NCs from free BSA and other interfering impurities.[217] The isolated Au NCs feature an enhanced emission at 615 nm (λ_{ex} not specified), and the oxidative quenching of this emission provides a good mechanism for H_2O_2 detection. Very recently, Chen et al. reported the protic-solvent-sensitive emission in 3D superatom complex inorganic frameworks (SCIFs), which are periodically cross-linked $[Au_1Ag_{22}(S\text{-}Adm)_{12}]^{3+}$ by SbF_6^-.[218] It was found that these SCIFs show a switchable emission at ~650 nm (λ_{ex} = 365 nm), which can be "turned on" or "turned off" in the presence or absence of protic solvents (e.g., water, methanol, and ethanol), respectively. This protic solvent selectivity is attributed to the coordination of solvent molecules with Au/Ag atoms or the formation of H-bonds between F atoms and solvent molecules. It should be noted that a similar solvent- or gas-molecule-sensitive luminescence has been widely recorded in Ag(I) NC-based metal–organic frameworks (MOFs), which are usually bridged by N-containing heterocyclic cross-linkers.[219–221]

The detection of large biomolecules (e.g., proteins) is another important topic in the sensor development of metal NCs. This detection largely depends on the specific bio-recognition and bio-conjugation interactions.[222,223] For example, Chen et al. designed a luminescent probe for glutathione S-transferase (GST)-tagged protein based on a specific GSH–GST interaction.[222] GSH-protected Au NCs with orange emission at 610 nm (λ_{ex} = 395 nm) were used as luminescent probes, which can specifically bind to GST or GST-tagged proteins (e.g., clumping factor A or ClfA for short). It is worth noting that this binding between the GSH ligand and GST can induce negligible changes in cluster luminescence, thus providing a convenient method to stain GST or GST-tagged ClfA. In this way, GST or GST-tagged ClfA can be identified by the naked eye in a mixture of proteins or in cell lysates. In addition to directly using SR ligands as recognition moieties, foreign recognition moieties

can also be conjugated to metal NCs to facilitate the selective detection of target biomolecules. For example, Kurdekar *et al.* recently developed an immunoassay based on luminescent Au NCs for sensitive detection of human immunodeficiency virus (HIV)-1 p24 antigen, which is an important biomarker for the early stage of HIV infection.[223] Streptavidin was conjugated to GSH-protected Au NCs (λ_{em} = 615 nm; λ_{ex} = 365 nm) by EDC chemistry. Then, the specific interaction between biotin and streptavidin was used to further couple biotinylated antibodies on the surface of Au NCs, thereby providing specific binding sites to HIV-1 p24 antigen. By forming an antibody–antigen–antibody sandwich complex with the capture antibody, the luminescent Au NCs can be immobilized in the immunoassay wells, thereby providing a means for quantitative detection of HIV-1 p24 antigen. The established immunoassay can deliver a LOD of 5 pg mL^{-1}, which is 3-fold higher than that of the traditional enzyme-linked immunoassay. In addition, this assay has a good selectivity against hepatitis B virus (HBV)-positive and hepatitis C virus (HCV)-positive plasma samples.

4.3. Molecular interactions/reactions in biomedical applications of metal NCs

Due to their small size, strong luminescence, good biocompatibility and efficient renal clearance, metal NCs have potential applications in diverse sectors of biomedicine, like bioimaging,[224,225] cancer therapy[226] and antimicrobial activity.[126,227] The most commonly used molecular reaction of metal NCs in these biomedical applications is covalent conjugation reaction that confers additional functional moieties to NCs, including active targeting moieties[122,124,228,229] and therapeutic moieties.[125,126,229] For example, since the overexpression of folate receptors has been observed on the surface of many cancer cells, Pyo *et al.* conjugated folic acid (FA) to $Au_{22}(SG)_{18}$ NCs through EDC chemistry, which can enhance the luminescence of Au NCs (QY = 42%, ~6.5-fold higher than that of the original $Au_{22}(SG)_{18}$) and improve the targeting efficacy toward folate-receptor positive KB and HeLa cells.[122] Similarly, by using EDC chemistry, Chen *et al.* co-conjugated FA and $Au_{29-43}(SG)_{27-37}$ to a pH-responsive amphiphilic copolymer, poly(DBAM-*co*-NAS-*co*-HEMA) or PDNH for short, where DBAM, NAS, and HEMA denote 4-*n*-dodecyloxybenzalacetal, *N*-succinimidylmethacrylate, and 2-hydroxyethyl methacrylate, respectively. After loading the anti-cancer drug paclitaxel (PTX), the Au NC-PDNH composite can simultaneously provide active targeting ability, luminescent imaging activity, and therapeutic effect in female athymic nude mice bearing HeLa tumors.[229] In addition to FA, peptides and proteins have also been conjugated to luminescent Au NCs, thereby enhancing their ability to target cancer cells for both imaging and killing purposes.[124,127] For example, streptavidin was conjugated to GSH-protected Au_{23} NCs, which emitted strong red light (λ_{em} = 685 nm), *via* EDC chemistry.[124] The as-obtained Au_{23} NC–streptavidin conjugate exhibits enhanced activity for imaging biotin-rich human hepatoma (HepG2) cells, by virtue of the specific streptavidin–biotin interaction.

Chemical and physical antimicrobial components have also been conjugated to Au or Ag NCs to evoke collective and synergistic antimicrobial mechanisms.[125,126] For example, with good awareness of the bactericidal activity of Ag-based nanomaterials, Zheng *et al.* combined $Ag_{16}(SG)_9$ NCs with a commercial antibiotic, daptomycin, through EDC chemistry.[125] The resulting composite (D-Ag NCs for short) appears in the form of a conjugated network of daptomycin and Ag NCs, with a typical hydrodynamic diameter of about 200 nm. It is further evident that such a conjugated network can provide a high localized concentration of both Ag NCs and daptomycin, which synergistically causes more serious damage to the membrane of bacterial cells. The damaged cell membrane in turn enhances the uptake of D-Ag NCs by bacteria, where Ag NCs can induce a high localized concentration of reactive oxygen species (ROS). Such a high concentration of ROS has been proved to be effective at destroying DNA, contributing to the enhanced antibacterial activity against Gram-positive model bacteria *Staphylococcus aureus* (*S. aureus*). In a follow-up study, the authors conjugated $[Au_{25}(Cystm)_x(MHA)_{18-x}]^-$ NCs (Cystm = cysteamine; x = 1–4) with Ho^{3+}-decorated graphene oxides (Ho-GOs) by a similar EDC approach.[126] Au NCs are an emerging family of nanoscale bactericides,[230] while Ho-GOs can serve as sharp edges with their orientation controllable by an external magnetic field. The aligned high density of sharp edges provides a physical means to destroy the bacterial membrane, which combined with the high oxidative stress induced by Au NCs can provide a synergistic mechanism to kill both Gram-positive (*e.g.*, *S. aureus*) and Gram-negative (*e.g.*, *Escherichia coli* or *E. coli* for short) bacteria. In addition to Au NCs, luminescent Ag NCs have also been conjugated to graphene sheets, which could be potentially used as antimicrobial and bioimaging agents.[231]

4.4. Molecular interactions/reactions in catalytic application of metal NCs

Due to the protein-like hierarchical structure, thiolate-protected noble metal NCs can provide a variety of coordination sites and a well-structured reaction environment for substrate molecules, thereby sustaining remarkable catalytic activity and selectivity toward various reactions, including oxidation, hydrogenation, and C–C coupling reactions.[5,7,26,232–237] Unlike their larger counterparts, metal nanoparticles (>3 nm), metal NCs can be synthesized with molecular purity and their structures can be probed at the unprecedented Å resolution.[8] The molecular level monodispersity and atomically precise structure make metal NCs particularly suitable for use as model catalysts, thus revealing the fundamentals of nanocatalysis at the molecular and atomic levels.

Among the various oxidation reactions, the aerobic oxidation of CO has received special attention due to its fundamental and practical importance.[238,239] From DFT calculations on three thiolate-protected (*i.e.*, $[Au_{25}(SR)_{18}]^-$, $Au_{102}(SR)_{44}$, and $Au_{144}(SR)_{60}$) and two phosphine-protected (*i.e.*, $Au_{11}(PH_3)_7Cl_3$ and $[Au_{39}(PH_3)_{14}Cl_6]^-$) Au NCs, Lopez-Acevedo *et al.* found that O_2 and CO can be co-adsorbed on the exposed Au(0) sites after the partial removal of the protecting ligands or motifs.[43] Afterwards, the activated O_2 can react with CO *via* a Langmuir–

Hinshelwood (LH) mechanism to generate CO_2 through a peroxyformate intermediate. Interestingly, Liu *et al.* also performed DFT calculations on a series of Au_n NCs ($n = 8$–34) and identified a triangular Au_3 facet as the active site for aerobic CO oxidation.[94] The authors proposed a novel tri-molecular LH mechanism, in which co-adsorption of one O_2 molecule and two CO molecules on the Au_3 facet facilitates the cleavage of the O–O bond through an OCOO* intermediate. It should be noted that adsorption of up to three molecules of O_2 by a single $[Au_{25}(SR)_{18}]^-$ has been experimentally evidenced by Bhat *et al.* based on ESI-MS analysis, strongly corroborating the ability of $[Au_{25}(SR)_{18}]^-$ to adsorb and activate molecular O_2 in various aerobic oxidation reactions including CO oxidation.[240] Since metal NCs are usually immobilized on the oxide supports in practical applications, the support effects have also been intensely evaluated. For example, Wu *et al.* proved the Mars and van Krevelen (MvK) mechanism for CO oxidation by the ^{18}O isotope labelling experiments, in which the lattice O atoms of the CeO_2 support also participated in the aerobic oxidation of CO catalysed by CeO_2-supported $[Au_{25}(S-C_2H_4Ph)_{18}]^-$.[241] The authors also found that the partial removal of SR ligands at the interface of $[Au_{25}(SR)_{18}]^-$ and CeO_2 is beneficial to increase the catalytic activity, thus confirming the theoretical prediction of Lopez-Acevedo *et al.*[43] In addition to support effects, in terms of the catalytic activity of metal NCs in the aerobic oxidation of CO, their size,[43,242] heteroatom doping,[155] ligand,[241] and pre-treatment[243] effects have been well studied.

Selective alkene oxidation is another oxidation reaction of current interest. For example, Zhu *et al.* reported a selective oxidation of styrene to benzaldehyde over styrene epoxide and acetophenone in the presence of supported (on SiO_2 or $Ca_{10}(PO_4)_6(OH)_2$) or unsupported $[Au_{25}(S-C_2H_4Ph)_{18}]^-$, $Au_{38}(S-C_2H_4Ph)_{24}$, and $Au_{144}(S-C_2H_4Ph)_{60}$, where the activation of O_2 is considered to be the key step.[244] This finding was further supported by the distinctly improved conversion of styrene (up to ~10-fold increase) when the more reactive *tert*-butyl hydroperoxide (BuOOH) was used as the oxidant or co-oxidant. A detailed mechanism of selective oxidation of styrene has been proposed based on the known crystal structure of $[Au_{25}(S-C_2H_4Ph)_{18}]^-$ (Fig. 10), in which O_2 is adsorbed on the electropositive Au_{13} core while the activation of the C=C bond occurs on the electronegative Au(I) in the protecting shell. Then, the oxidation proceeds through a cyclic transition state F (Fig. 10), where the preferential dissociation pathway of this transition state contributes to the selectivity of the overall oxidation reaction. In order to correlate the electronic structure of Au_{25} with catalytic selectivity, Liu *et al.* performed XAFS and ultraviolet photoemission spectroscopy analysis on $[Au_{25}(S-C_2H_4Ph)_{18}]^-$ and $[Au_{25}(PPh_3)_{10}(S-C_{12}H_{25})_5Cl_2]^{2+}$.[245] It was found that $[Au_{25}(PPh_3)_{10}(S-C_{12}H_{25})_5Cl_2]^{2+}$ has a more electropositive Au core, which yields a higher selectivity for more oxidized products (*i.e.*, benzaldehyde). It should be pointed out that based on DFT calculations, a slightly different mechanism has been proposed for the selective production of benzaldehyde, which involves a metastable four-membered ring CCOO* intermediate.[246] In addition to Au NCs, Ag NCs and alloy NCs have also been used as catalysts for the selective oxidation of styrene, where both catalytic activity and selectivity are proven to be tunable through size and composition engineering of metal NCs.[247]

Other than oxidation reactions, metal NCs also show good catalytic activity and selectivity to reduction and hydrogenation reactions. For example, Zhu *et al.* measured the effectiveness of
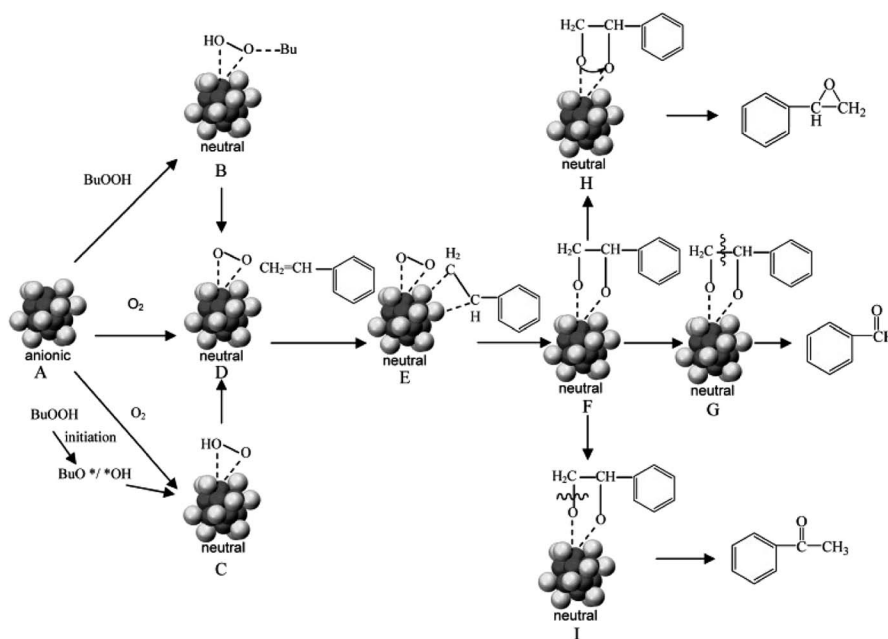

Fig. 10 Proposed catalytic mechanism of styrene oxidation by $[Au_{25}(SR)_{18}]^-$ in the presence of varied oxidants: BuOOH, O_2, and a mixture of them. Colour code: grey, core Au(0); light grey, motif Au(I); SR ligands are omitted for clarity. Reproduced with permission from ref. 244. Copyright 2010, Wiley-VCH.

both supported (on Fe_2O_3, TiO_2, and SiO_2) and unsupported $[Au_{25}(S\text{-}C_2H_4Ph)_{18}]^-$ in the selective hydrogenation of α,β-unsaturated ketones, where the hydrogenation of benzalacetone under one atmosphere of H_2 at 273 K can provide 100% selectivity to the unsaturated alcohols.[92] The authors attributed the extremely high selectivity to the unique activation pathway of H_2 and –C=O group determined by the Au(0)@Au(I)–SR core–shell structure of $[Au_{25}(S\text{-}C_2H_4Ph)_{18}]^-$. It is suggested that –C=O adsorption occurs in the pocket-like cavity of $[Au_{25}(S\text{-}C_2H_4Ph)_{18}]^-$, where the electronegative O is coordinated to the electropositive Au_{13} core. The electronegative Au(I) in the protecting shell of $[Au_{25}(S\text{-}C_2H_4Ph)_{18}]^-$ is considered to be the adsorption site of H_2. Afterwards, the addition reaction between the activated –C=O and H–H can generate α,β-unsaturated alcohols. In a separate study, Ouyang et al. carried out insightful DFT calculations for the selective hydrogenation of benzalacetone, and mapped out the reaction pathways at the atomic level.[248] The authors proposed a mechanism for H_2 activation assisted by α,β-unsaturated ketones, in which benzalacetone is co-adsorbed in the pocket-like cavity of $[Au_{25}(SR)_{18}]^-$ to facilitate the heterolytic cleavage of H_2. Through the transition state $Au^{\delta+}\cdots H^{\delta-}\cdots H^{\delta+}\cdots O^{\delta-}=C^{\delta+}$, this heterolytic cleavage can occur preferentially on the –C=O group, which is beneficial to the high selectivity of the unsaturated alcohol products.

Considering the unsatisfactory conversion of aldehydes (e.g., 4-nitrobenzaldehyde) by the supported $[Au_{25}(S\text{-}C_2H_4Ph)_{18}]^-$ in their hydrogenation reaction at low temperature (e.g., 13.4% at 323 K), Li et al. introduced transition metal cations (e.g., Cu^+, Cu^{2+}, Co^{2+}, and Cr^{3+}) as promoters to increase the catalytic activity of $[Au_{25}(S\text{-}C_2H_4Ph)_{18}]^-$ in the presence of a base (e.g., ammonia and pyridine).[249] It has been proved that the addition of metal cations can effectively increase the conversion of 4-nitrobenzaldehyde to 90.8% (using Co^{2+} as a promoter), while the 100% selectivity to 4-nitrobenzyl alcohol remains unchanged. Based on the results of matrix-assisted laser desorption/ionization (MALDI) MS, ESI-MS, and DFT calculations, the authors proposed a partial decomposition mechanism for the activation of H_2, in which [Au–SR]$_x$ modules ($x = 1$–4) dissociated from $[Au_{25}(S\text{-}C_2H_4Ph)_{18}]^-$ to provide active sites for the adsorption and activation of H_2.

The aforementioned partial decomposition mechanism well corroborates the hydride-assisted Au(I)–SR motif desorption–re-adsorption mechanism for the hydrogenation of 4-nitrophenol.[250] Nasarudin et al. used UV-vis absorption spectroscopy and ESI-MS to track the $NaBH_4$ hydrogenation of 4-nitrophenol in the presence of $[Au_{25}(p\text{-MBA})_{18}]^-$.[250] It was found that the addition of $NaBH_4$ to the reaction mixture may cause partial desorption of the SR ligands or SR–[Au(I)–SR]$_x$ motifs from $[Au_{25}(p\text{-MBA})_{18}]^-$, resulting in a series of smaller-sized Au NCs, among which $[Au_{23}(p\text{-MBA})_{16}]^-$ is the most abundant. Since the adsorption of hydrides on cluster species was widely observed in the early stage of the catalytic reaction, the authors concluded that hydride adsorption might promote the partial desorption of SR or SR–[Au(I)–SR]$_x$, which provided additional active sites for the hydrogenation reaction of 4-nitrophenol. More interestingly, the smaller-sized Au NCs (e.g., $[Au_{23}(p\text{-MBA})_{16}]^-$) can grow back to larger ones (e.g.,

$Au_{26}(p\text{-MBA})_{19}$) by re-adsorbing SR or SR–[Au(I)–SR]$_x$ in the final stage of the catalytic reaction, constituting a desorption–re-adsorption mechanism for the selective hydrogenation reaction of 4-nitrophenol. In another contribution, the authors also found that the hydrogenation pathway of 4-nitrophenol could be tunable based on the hierarchical structure of $[Au_{25}(p\text{-MBA})_{18}]^-$.[251] Leveraging on time-dependent UV-vis absorption spectroscopy, ESI-MS, and DFT calculations, the authors constructed a tri-molecular LH mechanism for semi-hydrogenation of 4-nitrophenol to 4,4′-dihydroxyazobenzene. The co-adsorption of two molecules of 4-nitrophenol and one molecule of BH_4^- in the pocket-like cavity of $[Au_{25}(p\text{-MBA})_{18}]^-$ facilitates the hydrogenation and subsequent coupling of 4-nitrophenol, giving rise to 4,4′-dihydroxyazobenzene particularly in its cis configuration. The formation of the semi-hydrogenation product 4,4′-dihydroxyazobenzene is in sharp contrast to the exclusive production of 4-aminophenol by conventional nano-gold catalysts.

Additionally, the molecular purity of metal NCs may provide unprecedented opportunities to understand the kinetics of catalytic reduction at the molecular and single-cluster level. For example, Zhang et al. were able to monitor the catalytic reduction kinetics of different-sized Au NCs in real time through single-molecule fluorescence microscopy.[252] The model reaction used in this study is the catalytic reduction of non-fluorescent resazurin to fluorescent resorufin through hydroxylamine, which makes possible a precise tracking of the formation and desorption of the reduction products on a single cluster by single-molecule fluorescence microscopy. The systematic kinetics analysis performed in this way shows that the catalytic reactions on $[Au_{25}(MPA)_{18}]^-$ and $Au_{18}(MPA)_{14}$ follow a non-competitive LH mechanism, where MPA denotes 3-mercapto-propionic acid. In contrast, the catalytic reduction on $Au_{15}(MPA)_{13}$ occurs through a competitive LH mechanism. This apparent difference in the catalytic mechanism of Au NCs with different sizes is attributed to the size-sensitive electronic structure of Au NCs, which determines their affinity to substrate and product molecules.

The diverse and delicate molecular interactions/reactions of metal NCs also make them useful for catalysing C–C coupling reactions. It is well known that the coupling reaction between p-iodoanisole (p-MeOPhI) and phenylacetylene (PhC≡CH) can occur through either cross-coupling or homo-coupling pathways, resulting in three different products, namely diphenyldiacetylene, 4,4′-dimethoxy-1,1′-biphenyl (DMBP), and 1-methoxy-4-(2-phenylethynyl)benzene (MPEB). Interestingly, by doping various heteroatoms (e.g., Ag, Au, and Pt) in $[Au_{25}(S\text{-}C_2H_4Ph)_{18}]^-$, the obtained alloy NCs (supported on TiO_2) showed distinctly different catalytic selectivity to the aforementioned three coupling products.[100] Specifically, $[Au_{25-x}Cu_x(S\text{-}C_2H_4Ph)_{18}]^-$ ($x = 0$–6) has high selectivity to DMBP (Ullmann homo-coupling product), while $[Au_{25}(S\text{-}C_2H_4Ph)_{18}]^-$ and $Au_{24}Pt(S\text{-}C_2H_4Ph)_{18}$ tend to form MPEB (Sonogashira cross-coupling product). In contrast, $[Au_{25-x}Ag_x(S\text{-}C_2H_4Ph)_{18}]^-$ ($x = 0$–5) shows comparable selectivity to MPEB (55.4%) and DMBP (44.6%). With the help of DFT calculations, the authors elucidate that two substrate molecules (i.e., p-MeOPhI or PhC≡CH)

can be co-adsorbed on the motif-type Au_3 facet of the pocket-like cavity of $Au_{25-x}M_x(SR)_{18}$ NCs, while the core composition of $Au_{25-x}M_x(SR)_{18}$ NCs determines the selective adsorption of p-MeOPhI/PhC≡CH or p-MeOPhI/p-MeOPhI, which ultimately dictates the pathway and final product of the C–C coupling reactions. Besides doping effects, the same group has also evaluated the ligand effects of $[Au_{25}(SR)_{18}]^-$ on the selectivity and activity of Ullmann coupling reaction.[253] In addition to Ullmann and Sonogashira coupling, metal NCs have also been shown to be active in catalysing the Suzuki cross-coupling reaction.[254] In particular, Abroshan *et al.* reported the high catalytic activity of TiO_2-supported $[Au_{25}(S-C_2H_4Ph)_{18}]^-$ in Suzuki cross-coupling reaction in the presence of an imidazolium-based ionic liquid.[254] The conversion of iodoanisole could be varied from 4% to 90% (or even higher) in its cross-coupling reaction with phenylboronic acid, when an optimized amount of BMIM·X (BMIM = 1-butyl-3-methylimidazolium; X = Br, Cl or BF_4) was introduced into the reaction system. The combined results of MALDI-MS and theoretical simulation show that the adsorption of $BMIM^+$ cations on the SR–Au(I)–SR$_2$ motifs of $[Au_{25}(S-C_2H_4Ph)_{18}]^-$ may lead to a successive dissociation of Au–SR modules, generating active sites on the remaining $[Au_{25-x}(S-C_2H_4Ph)_{18-x}]^-$ ($x = 1–4$) NCs to activate iodoanisole.

5.   Conclusions

In summary, owing to their protein-like hierarchical structure, thiolate-protected noble metal NCs possess a great diversity of active sites, making possible their interactions with ions, molecules, and other metal NCs. Such interactions include physical/chemical adsorption, metallophilicity, van der Waals interactions, π interactions, host–guest interactions, electrostatic interactions, H-bonds, and covalent bonds, depending on the chemical nature of the incoming species and their interacting sites on metal NCs. The fundamentals of the above interactions inherently determine the reactivity and selectivity of metal NCs in their formation (*e.g.*, size growth, metal exchange, ligand exchange, and motif exchange), self-assembly (*e.g.*, 1D, 2D, and 3D self-assembly) and applications (*e.g.*, sensors, biomedicine, and catalysis). It is well known that the remarkable reactivity and selectivity of metal NCs are a combined result of their well-organized atomic or molecular patterns at different hierarchical levels, of which the most notable example is the pocket-like cavity of $[Au_{25}(SR)_{18}]^-$ consisting of the core Au(0), motif Au(I) atoms, and SR ligands. In return, the atomically precise structure and structure-sensitive properties of metal NCs provide a good platform to probe and understand their molecular interactions/reactions with ions, molecules, and other metal NCs at the molecular and atomic levels. In the past two decades, remarkable achievements have been made in this regard through a combination of experimental and theoretical studies.

Although exciting achievements have been documented in understanding and implementing the molecular interactions/reactions of metal NCs, there are still challenges that require collaborative efforts of experimental and theoretical chemists.

For example, customizing the composition and structure of metal NCs atom by atom is a necessary prerequisite for atomic-level control of their molecular reactivity. Although many effective methods have been developed to customize the cluster size while keeping their size monodispersity unaffected, a similar atomically precise control of the alloying/ligand-exchange sites of noble metal NCs still remains a grand synthetic challenge.[7,8,142,170] In addition, the increasingly known dynamics of metal atoms and/or SR ligands in each NC imposes additional difficulties to precisely control the alloying/ligand-exchange sites in metal NCs.[163,255–257] It should be noted that similar metal and ligand dynamics have also been demonstrated at the inter-cluster level,[59,249,250] which suggests that the stability and integrity of noble metal NCs in practical applications should be carefully evaluated in the corresponding surroundings.

In addition to thiolates, many other organic ligands have been exploited to synthesize atomically precise metal NCs, due to their diverse binding modes and binding strength with metal centres. Such organic ligands of current interest include phosphines,[258–260] hydrides,[261–264] alkynyls,[265–268] N-heterocyclic carbenes,[269–271] carboxylates,[219,272,273] and solvent molecules.[219,272–275] In particular, recent findings have shown that organic ligands with relatively low binding affinity to Ag (*e.g.*, CF_3COO^- and CH_3CN) can be replaced by bridging ligands (*e.g.*, 4,4′-bypyridine), further cross-linking mixed-ligand-protected Ag NCs into a 3D network reminiscent of MOF structures.[219] Such Ag NC-based MOFs have enhanced stability and unique interactions with various gas and/or solvent molecules, making them particularly useful in sensing applications. This readily suggests that customizing organic ligands is an effective method that can not only tailor the metal–ligand interface, but also adjust the packing patterns of metal NCs in their assemblies. Therefore, continuous efforts should be devoted to engineering the metal–ligand interface by discovering and customizing organic ligands for metal NC fabrication.

In addition to the structure and composition customization at the intra-cluster level, engineering the packing patterns and symmetry of the metal NCs in their assemblies or supercrystals is an equally important means to regulate the molecular interactions/reactions of metal NCs. As discussed in Section 4.1, metal NCs have been assembled into 1D, 2D, and 3D superstructures with different orders, symmetries, and morphologies. However, due to its relatively short development history and sensitive dependence on high-quality building blocks, the self-assembly study (especially the exploration of crystallization) of noble metal NCs is still in its infancy. In particular, the governing principles are less well established for the self-assembly or crystallization chemistry of noble metal NCs, compared with those for the self-assembly or crystallization studies of molecular compounds or larger nanoparticles.[276–278] Such knowledge gap should be narrowed or eliminated in the near future.

To sum up, we have discussed recent progress in understanding the fundamentals and practicality of the interactions/reactions of metal NCs with ions, molecules, and other NCs. Since the synthesis, self-assembly, and practical application of

metal NCs are inherently determined by their molecular reactivity, the underlying and applied chemistry discussed in this *Review* can not only provide guiding principles for the synthesis of atomically precise noble metal NCs, but can also increase their acceptance in diverse sectors of post-synthesis developments (*e.g.*, self-assembly and practical application).

Conflicts of interest

There are no conflicts to declare.

Acknowledgements

References

1 M.-C. Daniel and D. Astruc, *Chem. Rev.*, 2003, **104**, 293–346.

2 P.-C. Chen, M. Liu, J. S. Du, B. Meckes, S. Wang, H. Lin, V. P. Dravid, C. Wolverton and C. A. Mirkin, *Science*, 2019, **363**, 959–964.

3 R. Jin, C. Zeng, M. Zhou and Y. Chen, *Chem. Rev.*, 2016, **116**, 10346–10413.

4 I. Chakraborty and T. Pradeep, *Chem. Rev.*, 2017, **117**, 8208–8271.

5 Y. Du, H. Sheng, D. Astruc and M. Zhu, *Chem. Rev.*, 2019, **120**, 526–622.

6 A. Fernando, K. L. D. M. Weerawardene, N. V. Karimova and C. M. Aikens, *Chem. Rev.*, 2015, **115**, 6112–6216.

7 Q. Yao, X. Yuan, T. Chen, D. T. Leong and J. Xie, *Adv. Mater.*, 2018, **30**, 1802751.

8 Q. Yao, T. Chen, X. Yuan and J. Xie, *Acc. Chem. Res.*, 2018, **51**, 1338–1348.

9 P. D. Jadzinsky, G. Calero, C. J. Ackerson, D. A. Bushnell and R. D. Kornberg, *Science*, 2007, **318**, 430–433.

10 M. Zhu, C. M. Aikens, F. J. Hollander, G. C. Schatz and R. Jin, *J. Am. Chem. Soc.*, 2008, **130**, 5883–5885.

11 M. W. Heaven, A. Dass, P. S. White, K. M. Holt and R. W. Murray, *J. Am. Chem. Soc.*, 2008, **130**, 3754–3755.

12 A. Desireddy, B. E. Conn, J. Guo, B. Yoon, R. N. Barnett, B. M. Monahan, K. Kirschbaum, W. P. Griffith, R. L. Whetten, U. Landman and T. P. Bigioni, *Nature*, 2013, **501**, 399–402.

13 H. Yang, Y. Wang, H. Huang, L. Gell, L. Lehtovaara, S. Malola, H. Häkkinen and N. Zheng, *Nat. Commun.*, 2013, **4**, 2422.

14 C. P. Joshi, M. S. Bootharaju, M. J. Alhilaly and O. M. Bakr, *J. Am. Chem. Soc.*, 2015, **137**, 11578–11581.

15 C. Zeng, Y. Chen, K. Kirschbaum, K. J. Lambright and R. Jin, *Science*, 2016, **354**, 1580–1584.

16 H. Yang, Y. Wang, X. Chen, X. Zhao, L. Gu, H. Huang, J. Yan, C. Xu, G. Li, J. Wu, A. J. Edwards, B. Dittrich, Z. Tang,

D. Wang, L. Lehtovaara, H. Häkkinen and N. Zheng, *Nat. Commun.*, 2016, **7**, 12809.

17 Y. Song, Y. Li, H. Li, F. Ke, J. Xiang, C. Zhou, P. Li, M. Zhu and R. Jin, *Nat. Commun.*, 2020, **11**, 478.

18 H. Häkkinen, M. Walter and H. Grönbeck, *J. Phys. Chem. B*, 2006, **110**, 9927–9931.

19 S. Chen, R. S. Ingram, M. J. Hostetler, J. J. Pietron, R. W. Murray, T. G. Schaaff, J. T. Khoury, M. M. Alvarez and R. L. Whetten, *Science*, 1998, **280**, 2098–2101.

20 Z. Wu, Q. Yao, O. J. H. Chai, N. Ding, W. Xu, S. Zang and J. Xie, *Angew. Chem., Int. Ed.*, 2020, **59**, 9934–9939.

21 K. Pyo, V. D. Thanthirige, K. Kwak, P. Pandurangan, G. Ramakrishna and D. Lee, *J. Am. Chem. Soc.*, 2015, **137**, 8244–8250.

22 T. Wang, D. Wang, J. W. Padelford, J. Jiang and G. Wang, *J. Am. Chem. Soc.*, 2016, **138**, 6380–6383.

23 S. Choi, R. M. Dickson and J. Yu, *Chem. Soc. Rev.*, 2012, **41**, 1867–1891.

24 S. Knoppe and T. Bürgi, *Acc. Chem. Res.*, 2014, **47**, 1318–1326.

25 S. Yamazoe, K. Koyasu and T. Tsukuda, *Acc. Chem. Res.*, 2013, **47**, 816–824.

26 T. Higaki, Y. Li, S. Zhao, Q. Li, S. Li, X.-S. Du, S. Yang, J. Chai and R. Jin, *Angew. Chem., Int. Ed.*, 2019, **58**, 8291–8302.

27 W. Chen and S. Chen, *Angew. Chem., Int. Ed.*, 2009, **48**, 4386–4389.

28 M. Yu and J. Zheng, *ACS Nano*, 2015, **9**, 6655–6674.

29 H. Zhu, J. Li, J. Wang and E. Wang, *ACS Appl. Mater. Interfaces*, 2019, **11**, 36831–36838.

30 L. Shang, J. Xu and G. U. Nienhaus, *Nano Today*, 2019, **28**, 100767.

31 L. Shang, F. Stockmar, N. Azadfar and G. U. Nienhaus, *Angew. Chem., Int. Ed.*, 2013, **52**, 11154–11157.

32 J. Zhang, Y. Fu, C. V. Conroy, Z. Tang, G. Li, R. Y. Zhao and G. Wang, *J. Phys. Chem. C*, 2012, **116**, 26561–26569.

33 B. Du, M. Yu and J. Zheng, *Nat. Rev. Mater.*, 2018, **3**, 358–374.

34 B. Du, X. Jiang, A. Das, Q. Zhou, M. Yu, R. Jin and J. Zheng, *Nat. Nanotechnol.*, 2017, **12**, 1096–1102.

35 K. G. Stamplecoskie and P. V. Kamat, *J. Am. Chem. Soc.*, 2014, **136**, 11093–11099.

36 Y.-S. Chen and P. V. Kamat, *J. Am. Chem. Soc.*, 2014, **136**, 6075–6082.

37 H. Zhang, H. Liu, Z. Tian, D. Lu, Y. Yu, S. Cestellos-Blanco, K. K. Sakimoto and P. Yang, *Nat. Nanotechnol.*, 2018, **13**, 900–905.

38 W. Kurashige, R. Hayashi, K. Wakamatsu, Y. Kataoka, S. Hossain, A. Iwase, A. Kudo, S. Yamazoe and Y. Negishi, *ACS Appl. Energy Mater.*, 2019, **2**, 4175–4187.

39 F. Liu, Y. Liu, Q. Yao, Y. Wang, X. Fang, C. Shen, F. Li, M. Huang, Z. Wang, W. Sand and J. Xie, *Environ. Sci. Technol.*, 2020, **54**, 5913–5921.

40 G. Zhang, R. Wang and G. Li, *Chin. Chem. Lett.*, 2018, **29**, 687–693.

41 C. Liu, X. Ren, F. Lin, X. Fu, X. Lin, T. Li, K. Sun and J. Huang, *Angew. Chem., Int. Ed.*, 2019, **58**, 11335–11339.

42 Y. Yu, Z. Luo, D. M. Chevrier, D. T. Leong, P. Zhang, D.-e. Jiang and J. Xie, *J. Am. Chem. Soc.*, 2014, **136**, 1246–1249.

43 O. Lopez-Acevedo, K. A. Kacprzak, J. Akola and H. Häkkinen, *Nat. Chem.*, 2010, **2**, 329–334.

44 Y. Chen, L. Li, L. Gong, T. Zhou and J. Liu, *Adv. Funct. Mater.*, 2019, **29**, 1806945.

45 Y. Liu, K. Ai, X. Cheng, L. Huo and L. Lu, *Adv. Funct. Mater.*, 2010, **20**, 951–956.

46 J. Xie, Y. Zheng and J. Y. Ying, *Chem. Commun.*, 2010, **46**, 961–963.

47 X. Yuan, T. J. Yeow, Q. Zhang, J. Y. Lee and J. Xie, *Nanoscale*, 2012, **4**, 1968–1971.

48 Z. Luo, V. Nachammai, B. Zhang, N. Yan, D. T. Leong, D.-e. Jiang and J. Xie, *J. Am. Chem. Soc.*, 2014, **136**, 10577–10580.

49 Q. Yao, X. Yuan, V. Fung, Y. Yu, D. T. Leong, D.-e. Jiang and J. Xie, *Nat. Commun.*, 2017, **8**, 927.

50 B. M. Barngrover and C. M. Aikens, *J. Phys. Chem. Lett.*, 2011, **2**, 990–994.

51 T. Chen, V. Fung, Q. Yao, Z. Luo, D.-e. Jiang and J. Xie, *J. Am. Chem. Soc.*, 2018, **140**, 11370–11377.

52 S. Tian, C. Yao, L. Liao, N. Xia and Z. Wu, *Chem. Commun.*, 2015, **51**, 11773–11776.

53 C. Yao, Y.-j. Lin, J. Yuan, L. Liao, M. Zhu, L.-h. Weng, J. Yang and Z. Wu, *J. Am. Chem. Soc.*, 2015, **137**, 15350–15353.

54 M. Rambukwella, L. Sementa, A. Fortunelli and A. Dass, *J. Phys. Chem. C*, 2017, **121**, 14929–14935.

55 T. Higaki, C. Liu, M. Zhou, T.-Y. Luo, N. L. Rosi and R. Jin, *J. Am. Chem. Soc.*, 2017, **139**, 9994–10001.

56 C. Peng, M. Yu and J. Zheng, *Nano Lett.*, 2019, **20**, 1378–1382.

57 S. Knoppe, A. C. Dharmaratne, E. Schreiner, A. Dass and T. Bürgi, *J. Am. Chem. Soc.*, 2010, **132**, 16783–16789.

58 S. Wang, Y. Song, S. Jin, X. Liu, J. Zhang, Y. Pei, X. Meng, M. Chen, P. Li and M. Zhu, *J. Am. Chem. Soc.*, 2015, **137**, 4018–4021.

59 Y. Niihori, S. Hashimoto, Y. Koyama, S. Hossain, W. Kurashige and Y. Negishi, *J. Phys. Chem. C*, 2019, **123**, 13324–13329.

60 Q. Yao, Y. Feng, V. Fung, Y. Yu, D.-e. Jiang, J. Yang and J. Xie, *Nat. Commun.*, 2017, **8**, 1555.

61 Q. Yao, V. Fung, C. Sun, S. Huang, T. Chen, D.-e. Jiang, J. Y. Lee and J. Xie, *Nat. Commun.*, 2018, **9**, 1979.

62 Y. Song, T. Huang and R. W. Murray, *J. Am. Chem. Soc.*, 2003, **125**, 11694–11701.

63 K. R. Krishnadas, A. Baksi, A. Ghosh, G. Natarajan and T. Pradeep, *Nat. Commun.*, 2016, **7**, 13447.

64 K. R. Krishnadas, A. Ghosh, A. Baksi, I. Chakraborty, G. Natarajan and T. Pradeep, *J. Am. Chem. Soc.*, 2016, **138**, 140–148.

65 K. R. Krishnadas, A. Baksi, A. Ghosh, G. Natarajan, A. Som and T. Pradeep, *Acc. Chem. Res.*, 2017, **50**, 1988–1996.

66 C. Zeng, C. Liu, Y. Pei and R. Jin, *ACS Nano*, 2013, **7**, 6138–6145.

67 M. S. Bootharaju, C. P. Joshi, M. J. Alhilaly and O. M. Bakr, *Chem. Mater.*, 2016, **28**, 3292–3297.

68 D. M. Chevrier, B. E. Conn, B. Li, D.-e. Jiang, T. P. Bigioni, A. Chatt and P. Zhang, *ACS Nano*, 2020, **14**, 8433–8441.

69 D. M. Chevrier, L. Raich, C. Rovira, A. Das, Z. Luo, Q. Yao, A. Chatt, J. Xie, R. Jin, J. Akola and P. Zhang, *J. Am. Chem. Soc.*, 2018, **140**, 15430–15436.

70 P. Zhang, *J. Phys. Chem. C*, 2014, **118**, 25291–25299.

71 S. Yamazoe and T. Tsukuda, *Bull. Chem. Soc. Jpn.*, 2019, **92**, 193–204.

72 S. Yamazoe, S. Takano, W. Kurashige, T. Yokoyama, K. Nitta, Y. Negishi and T. Tsukuda, *Nat. Commun.*, 2016, **7**, 10414.

73 M. Brust, M. Walker, D. Bethell, D. J. Schiffrin and R. Whyman, *J. Chem. Soc., Chem. Commun.*, 1994, 801–802.

74 R. H. Terrill, T. A. Postlethwaite, C.-h. Chen, C.-D. Poon, A. Terzis, A. Chen, J. E. Hutchison, M. R. Clark, G. Wignall, J. D. Londono, R. Superfine, M. Falvo, C. S. Johnson Jr, E. T. Samulski and R. W. Murray, *J. Am. Chem. Soc.*, 1995, **117**, 12537–12548.

75 R. S. Ingram, M. J. Hostetler and R. W. Murray, *J. Am. Chem. Soc.*, 1997, **119**, 9175–9178.

76 R. L. Whetten, J. T. Khoury, M. M. Alvarez, S. Murthy, I. Vezmar, Z. L. Wang, P. W. Stephens, C. L. Cleveland, W. D. Luedtke and U. Landman, *Adv. Mater.*, 1996, **8**, 428–433.

77 T. G. Schaaff, M. N. Shafigullin, J. T. Khoury, I. Vezmar, R. L. Whetten, W. G. Cullen, P. N. First, C. Gutiérrez-Wing, J. Ascensio and M. J. Jose-Yacamán, *J. Phys. Chem. B*, 1997, **101**, 7885–7891.

78 M. S. Bootharaju, C. P. Joshi, M. R. Parida, O. F. Mohammed and O. M. Bakr, *Angew. Chem., Int. Ed.*, 2015, **55**, 922–926.

79 C. Kumara, C. M. Aikens and A. Dass, *J. Phys. Chem. Lett.*, 2014, **5**, 461–466.

80 C. Kumara, K. J. Gagnon and A. Dass, *J. Phys. Chem. Lett.*, 2015, **6**, 1223–1228.

81 H. Yang, Y. Wang, J. Yan, X. Chen, X. Zhang, H. Häkkinen and N. Zheng, *J. Am. Chem. Soc.*, 2014, **136**, 7197–7200.

82 S. Tian, L. Liao, J. Yuan, C. Yao, J. Chen, J. Yang and Z. Wu, *Chem. Commun.*, 2016, **52**, 9873–9876.

83 J. Yan, H. Su, H. Yang, S. Malola, S. Lin, H. Häkkinen and N. Zheng, *J. Am. Chem. Soc.*, 2015, **137**, 11880–11883.

84 M. A. Tofanelli, T. W. Ni, B. D. Phillips and C. J. Ackerson, *Inorg. Chem.*, 2016, **55**, 999–1001.

85 L. Liao, S. Zhou, Y. Dai, L. Liu, C. Yao, C. Fu, J. Yang and Z. Wu, *J. Am. Chem. Soc.*, 2015, **137**, 9511–9514.

86 H. Qian, W. T. Eckenhoff, Y. Zhu, T. Pintauer and R. Jin, *J. Am. Chem. Soc.*, 2010, **132**, 8280–8281.

87 T. Higaki, M. Zhou, K. J. Lambright, K. Kirschbaum, M. Y. Sfeir and R. Jin, *J. Am. Chem. Soc.*, 2018, **140**, 5691–5695.

88 N. A. Sakthivel, M. Stener, L. Sementa, A. Fortunelli, G. Ramakrishna and A. Dass, *J. Phys. Chem. Lett.*, 2018, **9**, 1295–1300.

89 D. Crasto, S. Malola, G. Brosofsky, A. Dass and H. Häkkinen, *J. Am. Chem. Soc.*, 2014, **136**, 5000–5005.

90 S. Chen, S. Wang, J. Zhong, Y. Song, J. Zhang, H. Sheng, Y. Pei and M. Zhu, *Angew. Chem., Int. Ed.*, 2015, **54**, 3145–3149.

91 Y. Zhu, Z. Wu, C. Gayathri, H. Qian, R. R. Gil and R. Jin, *J. Catal.*, 2010, **271**, 155–160.

92 Y. Zhu, H. Qian, B. A. Drake and R. Jin, *Angew. Chem., Int. Ed.*, 2010, **49**, 1295–1298.

93 M. Zhu, W. T. Eckenhoff, T. Pintauer and R. Jin, *J. Phys. Chem. C*, 2008, **112**, 14221–14224.

94 C. Liu, Y. Tan, S. Lin, H. Li, X. Wu, L. Li, Y. Pei and X. C. Zeng, *J. Am. Chem. Soc.*, 2013, **135**, 2583–2595.

95 S. Xie, H. Tsunoyama, W. Kurashige, Y. Negishi and T. Tsukuda, *ACS Catal.*, 2012, **2**, 1519–1523.

96 Y. Negishi, K. Igarashi, K. Munakata, W. Ohgake and K. Nobusada, *Chem. Commun.*, 2012, **48**, 660–662.

97 K. Kwak, W. Choi, Q. Tang, M. Kim, Y. Lee, D.-e. Jiang and D. Lee, *Nat. Commun.*, 2017, **8**, 14723.

98 K. Kwak, W. Choi, Q. Tang, D.-e. Jiang and D. Lee, *J. Mater. Chem. A*, 2018, **6**, 19495–19501.

99 Y. Lu, C. Zhang, X. Li, A. R. Frojd, W. Xing, A. Z. Clayborne and W. Chen, *Nano Energy*, 2018, **50**, 316–322.

100 Z. Li, X. Yang, C. Liu, J. Wang and G. Li, *Prog. Nat. Sci.*, 2016, **26**, 477–482.

101 L. Andrews, *Chem. Soc. Rev.*, 2004, **33**, 123–132.

102 C. Mohr, H. Hofmeister, J. Radnik and P. Claus, *J. Am. Chem. Soc.*, 2003, **125**, 1905–1911.

103 G. Li, D.-e. Jiang, C. Liu, C. Yu and R. Jin, *J. Catal.*, 2013, **306**, 177–183.

104 G. Li and R. Jin, *J. Am. Chem. Soc.*, 2014, **136**, 11347–11354.

105 Y. Liu, X. Chai, X. Cai, M. Chen, R. Jin, W. Ding and Y. Zhu, *Angew. Chem., Int. Ed.*, 2018, **57**, 9775–9779.

106 M. De Nardi, S. Antonello, D.-e. Jiang, F. Pan, K. Rissanen, M. Ruzzi, A. Venzo, A. Zoleo and F. Maran, *ACS Nano*, 2014, **8**, 8505–8512.

107 T. W. Ni, M. A. Tofanelli, B. D. Phillips and C. J. Ackerson, *Inorg. Chem.*, 2014, **53**, 6500–6502.

108 Z. Wu, Y. Du, J. Liu, Q. Yao, T. Chen, Y. Cao, H. Zhang and J. Xie, *Angew. Chem., Int. Ed.*, 2019, **58**, 8139–8144.

109 W. Fei, S. Antonello, T. Dainese, A. Dolmella, M. Lahtinen, K. Rissanen, A. Venzo and F. Maran, *J. Am. Chem. Soc.*, 2019, **141**, 16033–16045.

110 D. R. Kauffman, D. Alfonso, C. Matranga, P. Ohodnicki, X. Deng, R. C. Siva, C. Zeng and R. Jin, *Chem. Sci.*, 2014, **5**, 3151–3157.

111 C. Zeng, Y. Chen, A. Das and R. Jin, *J. Phys. Chem. Lett.*, 2015, **6**, 2976–2986.

112 K. R. Krishnadas, G. Natarajan, A. Baksi, A. Ghosh, E. Khatun and T. Pradeep, *Langmuir*, 2019, **35**, 11243–11254.

113 E. Khatun, A. Ghosh, P. Chakraborty, P. Singh, M. Bodiuzzaman, P. Ganesan, G. Natarajan, J. Ghosh, S. K. Pal and T. Pradeep, *Nanoscale*, 2018, **10**, 20033–20042.

114 P. Liu, R. Qin, G. Fu and N. Zheng, *J. Am. Chem. Soc.*, 2017, **139**, 2122–2131.

115 H. Häkkinen, *Nat. Chem.*, 2012, **4**, 443–455.

116 C. L. Heinecke, T. W. Ni, S. Malola, V. Mäkinen, O. A. Wong, H. Häkkinen and C. J. Ackerson, *J. Am. Chem. Soc.*, 2012, **134**, 13316–13322.

117 Y. Niihori, Y. Kikuchi, A. Kato, M. Matsuzaki and Y. Negishi, *ACS Nano*, 2015, **9**, 9347–9356.

118 P. Pengo, C. Bazzo, M. Boccalon and L. Pasquato, *Chem. Commun.*, 2015, **51**, 3204–3207.

119 G. Salassa, A. Sels, F. Mancin and T. Bürgi, *ACS Nano*, 2017, **11**, 12609–12614.

120 A. Baksi, M. S. Bootharaju, P. K. Chhotaray, P. Chakraborty, B. Mondal, S. Bhat, R. Gardas and T. Pradeep, *J. Phys. Chem. C*, 2017, **121**, 26483–26492.

121 C.-A. J. Lin, T.-Y. Yang, C.-H. Lee, S. H. Huang, R. A. Sperling, M. Zanella, J. K. Li, J.-L. Shen, H.-H. Wang, H.-I. Yeh, W. J. Parak and W. H. Chang, *ACS Nano*, 2009, **3**, 395–401.

122 K. Pyo, N. H. Ly, S. Y. Yoon, Y. Shen, S. Y. Choi, S. Y. Lee, S.-W. Joo and D. Lee, *Adv. Healthcare Mater.*, 2017, **6**, 1700203.

123 K. Pyo, V. D. Thanthirige, S. Y. Yoon, G. Ramakrishna and D. Lee, *Nanoscale*, 2016, **8**, 20008–20016.

124 M. A. H. Muhammed, P. K. Verma, S. K. Pal, R. C. A. Kumar, S. Paul, R. V. Omkumar and T. Pradeep, *Chem. Eur. J.*, 2009, **15**, 10110–10120.

125 K. Zheng, M. I. Setyawati, T.-P. Lim, D. T. Leong and J. Xie, *ACS Nano*, 2016, **10**, 7934–7942.

126 K. Zheng, K. Li, T.-H. Chang, J. Xie and P.-Y. Chen, *Adv. Funct. Mater.*, 2019, **29**, 1904603.

127 R. Vankayala, C.-L. Kuo, K. Nuthalapati, C.-S. Chiang and K. C. Hwang, *Adv. Funct. Mater.*, 2015, **25**, 5934–5945.

128 Nonappa, T. Lahtinen, J. S. Haataja, T.-R. Tero, H. Häkkinen and O. Ikkala, *Angew. Chem., Int. Ed.*, 2016, **55**, 16035–16038.

129 Q. Yao, X. Yuan, Y. Yu, Y. Yu, J. Xie and J. Y. Lee, *J. Am. Chem. Soc.*, 2015, **137**, 2128–2136.

130 S. Hossain, Y. Imai, Y. Motohashi, Z. Chen, D. Suzuki, T. Suzuki, Y. Kataoka, M. Hirata, T. Ono, W. Kurashige, T. Kawawaki, T. Yamamoto and Y. Negishi, *Mater. Horizons*, 2020, **7**, 796–803.

131 Z. Wu, J. Liu, Y. Li, Z. Cheng, T. Li, H. Zhang, Z. Lu and B. Yang, *ACS Nano*, 2015, **9**, 6315–6323.

132 D. J. Cram and J. M. Cram, *Science*, 1974, **183**, 803–809.

133 Y. Wu, R. Shi, Y.-L. Wu, J. M. Holcroft, Z. Liu, M. Frasconi, M. R. Wasielewski, H. Li and J. F. Stoddart, *J. Am. Chem. Soc.*, 2015, **137**, 4111–4118.

134 M. A. Moussawi, N. Leclerc-Laronze, S. Floquet, P. A. Abramov, M. N. Sokolov, S. Cordier, A. Ponchel, E. Monflier, H. Bricout, D. Landy, M. Haouas, J. Marrot and E. Cadot, *J. Am. Chem. Soc.*, 2017, **139**, 12793–12803.

135 A. Mathew, G. Natarajan, L. Lehtovaara, H. Häkkinen, R. M. Kumar, V. Subramanian, A. Jaleel and T. Pradeep, *ACS Nano*, 2013, **8**, 139–152.

136 Y. Zhao, S. Zhuang, L. Liao, C. Wang, N. Xia, Z. Gan, W. Gu, J. Li, H. Deng and Z. Wu, *J. Am. Chem. Soc.*, 2019, **142**, 973–977.

137 H. Zhu, N. Goswami, Q. Yao, T. Chen, Y. Liu, Q. Xu, D. Chen, J. Lu and J. Xie, *J. Mater. Chem. A*, 2018, **6**, 1102–1108.

138 P. Chakraborty, A. Nag, A. Chakraborty and T. Pradeep, *Acc. Chem. Res.*, 2019, **52**, 2–11.

139 P. Chakraborty, A. Nag, G. Paramasivam, G. Natarajan and T. Pradeep, *ACS Nano*, 2018, **12**, 2415–2425.

140 P. Chakraborty, A. Nag, B. Mondal, E. Khatun, G. Paramasivam and T. Pradeep, *J. Phys. Chem. C*, 2020, **124**, 14891–14900.

141 P. Chakraborty, A. Nag, K. S. Sugi, T. Ahuja, B. Varghese and T. Pradeep, *ACS Mater. Lett.*, 2019, **1**, 534–540.

142 S. Hossain, Y. Niihori, L. V. Nair, B. Kumar, W. Kurashige and Y. Negishi, *Acc. Chem. Res.*, 2018, **51**, 3114–3124.

143 Y. Yu, X. Chen, Q. Yao, Y. Yu, N. Yan and J. Xie, *Chem. Mater.*, 2013, **25**, 946–952.

144 Y. Yu, Q. Yao, K. Cheng, X. Yuan, Z. Luo and J. Xie, *Part. Part. Syst. Char.*, 2014, **31**, 652–656.

145 P. J. G. Goulet and R. B. Lennox, *J. Am. Chem. Soc.*, 2010, **132**, 9582–9584.

146 Y. Li, O. Zaluzhna, B. Xu, Y. Gao, J. M. Modest and Y. J. Tong, *J. Am. Chem. Soc.*, 2011, **133**, 2092–2095.

147 Y. Li, O. Zaluzhna and Y. J. Tong, *Langmuir*, 2011, **27**, 7366–7370.

148 T. Dainese, S. Antonello, S. Bogialli, W. Fei, A. Venzo and F. Maran, *ACS Nano*, 2018, **12**, 7057–7066.

149 M. Suyama, S. Takano, T. Nakamura and T. Tsukuda, *J. Am. Chem. Soc.*, 2019, **141**, 14048–14051.

150 Y. Zhu, H. Wang, K. Wan, J. Guo, C. He, Y. Yu, L. Zhao, Y. Zhang, J. Lv, L. Shi, R. Jin, X. Zhang, X. Shi and Z. Tang, *Angew. Chem., Int. Ed.*, 2018, **57**, 9059–9063.

151 J. Yan, H.-F. Su, H. Yang, C. Hu, S. Malola, S.-C. Lin, B. K. Teo, H. Häkkinen and N. Zheng, *J. Am. Chem. Soc.*, 2016, **138**, 12751–12754.

152 H. Yao, T. Fukui and K. Kimura, *J. Phys. Chem. C*, 2008, **112**, 16281–16285.

153 S. Knoppe, O. A. Wong, S. Malola, H. Häkkinen, T. Bürgi, T. Verbiest and C. J. Ackerson, *J. Am. Chem. Soc.*, 2014, **136**, 4129–4132.

154 M. van der Linden, A. J. van Bunningen, L. Amidani, M. Bransen, H. Elnaggar, P. Glatzel, A. Meijerink and F. M. F. de Groot, *ACS Nano*, 2018, **12**, 12751–12760.

155 W. Li, C. Liu, H. Abroshan, Q. Ge, X. Yang, H. Xu and G. Li, *J. Phys. Chem. C*, 2016, **120**, 10261–10267.

156 C. Yao, J. Chen, M.-B. Li, L. Liu, J. Yang and Z. Wu, *Nano Lett.*, 2015, **15**, 1281–1287.

157 X. Liu, J. Yuan, J. Chen, J. Yang and Z. Wu, *Part. Part. Syst. Char.*, 2019, **36**, 1900003.

158 J.-P. Choi, C. A. Fields-Zinna, R. L. Stiles, R. Balasubramanian, A. D. Douglas, M. C. Crowe and R. W. Murray, *J. Phys. Chem. C*, 2010, **114**, 15890–15896.

159 S. Zhuang, D. Chen, L. Liao, Y. Zhao, N. Xia, W. Zhang, C. Wang, J. Yang and Z. Wu, *Angew. Chem., Int. Ed.*, 2020, **59**, 3073–3077.

160 X. Dou, X. Yuan, Y. Yu, Z. Luo, Q. Yao, D. T. Leong and J. Xie, *Nanoscale*, 2014, **6**, 157–161.

161 Q. Li, S. Wang, K. Kirschbaum, K. J. Lambright, A. Das and R. Jin, *Chem. Commun.*, 2016, **52**, 5194–5197.

162 M. Zhu, P. Wang, N. Yan, X. Chai, L. He, Y. Zhao, N. Xia, C. Yao, J. Li, H. Deng, Y. Zhu, Y. Pei and Z. Wu, *Angew. Chem., Int. Ed.*, 2018, **57**, 4500–4504.

163 K. Zheng, V. Fung, X. Yuan, D.-e. Jiang and J. Xie, *J. Am. Chem. Soc.*, 2019, **141**, 18977–18983.

164 K. R. Krishnadas, A. Baksi, A. Ghosh, G. Natarajan and T. Pradeep, *ACS Nano*, 2017, **11**, 6015–6023.

165 A. Baksi, E. K. Schneider, P. Weis, K. R. Krishnadas, D. Ghosh, H. Hahn, T. Pradeep and M. M. Kappes, *J. Phys. Chem. C*, 2019, **123**, 28477–28485.

166 P. Chakraborty and T. Pradeep, *NPG Asia Mater.*, 2019, **11**, 48.

167 B. Zhang, G. Salassa and T. Bürgi, *Chem. Commun.*, 2016, **52**, 9205–9207.

168 R. Kazan, U. Müller and T. Bürgi, *Nanoscale*, 2019, **11**, 2938–2945.

169 Z. Gan, N. Xia and Z. Wu, *Acc. Chem. Res.*, 2018, **51**, 2774–2783.

170 A. Ghosh, O. F. Mohammed and O. M. Bakr, *Acc. Chem. Res.*, 2018, **51**, 3094–3103.

171 M. Bootharaju, L. Sinatra and O. M. Bakr, *Nanoscale*, 2016, **8**, 17333–17339.

172 N. Yan, L. Liao, J. Yuan, Y.-j. Lin, L.-h. Weng, J. Yang and Z. Wu, *Chem. Mater.*, 2016, **28**, 8240–8247.

173 S. Sharma, S. Yamazoe, T. Ono, W. Kurashige, Y. Niihori, K. Nobusada, T. Tsukuda and Y. Negishi, *Dalton Trans.*, 2016, **45**, 18064–18068.

174 E. Khatun, P. Chakraborty, B. R. Jacob, G. Paramasivam, M. Bodiuzzaman, W. A. Dar and T. Pradeep, *Chem. Mater.*, 2019, **32**, 611–619.

175 E. S. Shibu, M. A. H. Muhammed, T. Tsukuda and T. Pradeep, *J. Phys. Chem. C*, 2008, **112**, 12168–12176.

176 A. Dass, A. Stevenson, G. R. Dubay, J. B. Tracy and R. W. Murray, *J. Am. Chem. Soc.*, 2008, **130**, 5940–5946.

177 C. A. Fields-Zinna, J. F. Parker and R. W. Murray, *J. Am. Chem. Soc.*, 2010, **132**, 17193–17198.

178 L. G. AbdulHalim, N. Kothalawala, L. Sinatra, A. Dass and O. M. Bakr, *J. Am. Chem. Soc.*, 2014, **136**, 15865–15868.

179 C. Zeng, T. Li, A. Das, N. L. Rosi and R. Jin, *J. Am. Chem. Soc.*, 2013, **135**, 10011–10013.

180 S. K. Eswaramoorthy, N. A. Sakthivel and A. Dass, *J. Phys. Chem. C*, 2019, **123**, 9634–9639.

181 M. S. Bootharaju, V. M. Burlakov, T. M. D. Besong, C. P. Joshi, L. G. AbdulHalim, D. Black, R. Whetten, A. Goriely and O. M. Bakr, *Chem. Mater.*, 2015, **27**, 4289–4297.

182 A. Dass, T. C. Jones, S. Theivendran, L. Sementa and A. Fortunelli, *J. Phys. Chem. C*, 2017, **121**, 14914–14919.

183 Y. Chen, C. Liu, Q. Tang, C. Zeng, T. Higaki, A. Das, D.-e. Jiang, N. L. Rosi and R. Jin, *J. Am. Chem. Soc.*, 2016, **138**, 1482–1485.

184 X. Kang and M. Zhu, *Chem. Mater.*, 2019, **31**, 9939–9969.

185 Y. Niihori, S. Hossain, S. Sharma, B. Kumar, W. Kurashige and Y. Negishi, *Chem. Rec.*, 2017, **17**, 473–484.

186 A. Chakraborty, A. C. Fernandez, A. Som, B. Mondal, G. Natarajan, G. Paramasivam, T. Lahtinen, H. Häkkinen, Nonappa and T. Pradeep, *Angew. Chem., Int. Ed.*, 2018, **57**, 6522–6526.

187 X. Liu, G. Saranya, X. Huang, X. Cheng, R. Wang, M. Chen, C. Zhang, T. Li and Y. Zhu, *Angew. Chem., Int. Ed.*, 2020, **59**, 13941–13946.

188 T. Lahtinen, E. Hulkko, K. Sokolowska, T.-R. Tero, V. Saarnio, J. Lindgren, M. Pettersson, H. Häkkinen and L. Lehtovaara, *Nanoscale*, 2016, **8**, 18665–18674.

189 Nonappa and O. Ikkala, *Adv. Funct. Mater.*, 2017, **28**, 1704328.

190 B. Yoon, W. D. Luedtke, R. N. Barnett, J. Gao, A. Desireddy, B. E. Conn, T. Bigioni and U. Landman, *Nat. Mater.*, 2014, **13**, 807–811.

191 Q. Yao, Y. Yu, X. Yuan, Y. Yu, D. Zhao, J. Xie and J. Y. Lee, *Angew. Chem., Int. Ed.*, 2015, **54**, 184–189.

192 Z. Wu, C. Dong, Y. Li, H. Hao, H. Zhang, Z. Lu and B. Yang, *Angew. Chem., Int. Ed.*, 2013, **52**, 9952–9955.

193 J. V. Rival, Nonappa and E. S. Shibu, *ACS Appl. Mater. Interfaces*, 2020, **12**, 14569–14577.

194 R. J. Macfarlane, B. Lee, M. R. Jones, N. Harris, G. C. Schatz and C. A. Mirkin, *Science*, 2011, **334**, 204–208.

195 S. Y. Park, A. K. R. Lytton-Jean, B. Lee, S. Weigand, G. C. Schatz and C. A. Mirkin, *Nature*, 2008, **451**, 553–556.

196 D. Nykypanchuk, M. M. Maye, D. van der Lelie and O. Gang, *Nature*, 2008, **451**, 549–552.

197 A. Som, I. Chakraborty, T. A. Maark, S. Bhat and T. Pradeep, *Adv. Mater.*, 2016, **28**, 2827–2833.

198 L.-Y. Chen, C.-W. Wang, Z. Yuan and H.-T. Chang, *Anal. Chem.*, 2015, **87**, 216–229.

199 A. Mathew and T. Pradeep, *Part. Part. Syst. Char.*, 2014, **31**, 1017–1053.

200 Z. Wu, M. Wang, J. Yang, X. Zheng, W. Cai, G. Meng, H. Qian, H. Wang and R. Jin, *Small*, 2012, **8**, 2028–2035.

201 L. Shang, L. Yang, F. Stockmar, R. Popescu, V. Trouillet, M. Bruns, D. Gerthsen and G. U. Nienhaus, *Nanoscale*, 2012, **4**, 4155–4160.

202 M. S. Bootharaju and T. Pradeep, *Langmuir*, 2011, **27**, 8134–8143.

203 G. Zhang, Y. Li, J. Xu, C. Zhang, S. Shuang, C. Dong and M. M. F. Choi, *Sens. Actuators B Chem.*, 2013, **183**, 583–588.

204 Y.-T. Su, G.-Y. Lan, W.-Y. Chen and H.-T. Chang, *Anal. Chem.*, 2010, **82**, 8566–8572.

205 E. S. Shibu and T. Pradeep, *Chem. Mater.*, 2011, **23**, 989–999.

206 H. Liu, X. Zhang, X. Wu, L. Jiang, C. Burda and J.-J. Zhu, *Chem. Commun.*, 2011, **47**, 4237–4239.

207 N. Goswami, A. Giri, M. S. Bootharaju, P. L. Xavier, T. Pradeep and S. K. Pal, *Anal. Chem.*, 2011, **83**, 9676–9680.

208 I. Chakraborty, T. Udayabhaskararao and T. Pradeep, *J. Hazard. Mater.*, 2012, **211–212**, 396–403.

209 A. George, E. S. Shibu, S. M. Maliyekkal, M. S. Bootharaju and T. Pradeep, *ACS Appl. Mater. Interfaces*, 2012, **4**, 639–644.

210 Y. Guo, Z. Wang, H. Shao and X. Jiang, *Analyst*, 2012, **137**, 301–304.

211 M. A. Habeeb Muhammed and T. Pradeep, *Chem. Phys. Lett.*, 2007, **449**, 186–190.

212 J. Shen, Z. Wang, D. Sun, C. Xia, S. Yuan, P. Sun and X. Xin, *ACS Appl. Mater. Interfaces*, 2018, **10**, 3955–3963.

213 S. Roy, G. Palui and A. Banerjee, *Nanoscale*, 2012, **4**, 2734–2740.

214 T. Zhou, M. Rong, Z. Cai, C. J. Yang and X. Chen, *Nanoscale*, 2012, **4**, 4103–4106.

215 C.-C. Huang, Z. Yang, K.-H. Lee and H.-T. Chang, *Angew. Chem., Int. Ed.*, 2007, **46**, 6824–6828.

216 X. Yuan, Y. Tay, X. Dou, Z. Luo, D. T. Leong and J. Xie, *Anal. Chem.*, 2012, **85**, 1913–1919.

217 G. Guan, S.-Y. Zhang, Y. Cai, S. Liu, M. S. Bharathi, M. Low, Y. Yu, J. Xie, Y. Zheng, Y.-W. Zhang and M. Han, *Chem. Commun.*, 2014, **50**, 5703–5705.

218 S. Chen, W. Du, C. Qin, D. Liu, L. Tang, Y. Liu, S. Wang and M. Zhu, *Angew. Chem., Int. Ed.*, 2020, **59**, 7542–7547.

219 R.-W. Huang, Y.-S. Wei, X.-Y. Dong, X.-H. Wu, C.-X. Du, S.-Q. Zang and T. C. W. Mak, *Nat. Chem.*, 2017, **9**, 689.

220 X.-H. Wu, P. Luo, Z. Wei, Y.-Y. Li, R.-W. Huang, X.-Y. Dong, K. Li, S.-Q. Zang and B. Z. Tang, *Adv. Sci.*, 2019, **6**, 1801304.

221 M. Cao, R. Pang, Q.-Y. Wang, Z. Han, Z.-Y. Wang, X.-Y. Dong, S.-F. Li, S.-Q. Zang and T. C. W. Mak, *J. Am. Chem. Soc.*, 2019, **141**, 14505–14509.

222 C.-T. Chen, W.-J. Chen, C.-Z. Liu, L.-Y. Chang and Y.-C. Chen, *Chem. Commun.*, 2009, 7515–7517.

223 A. D. Kurdekar, L. A. Avinash Chunduri, C. S. Manohar, M. K. Haleyurgirisetty, I. K. Hewlett and K. Venkataramaniah, *Sci. Adv.*, 2018, **4**, eaar6280.

224 Nonappa, *Beilstein J. Nanotechnol.*, 2020, **11**, 533–546.

225 X. Jiang, B. Du, Y. Huang and J. Zheng, *Nano Today*, 2018, **21**, 106–125.

226 N. Goswami, Z. Luo, X. Yuan, D. T. Leong and J. Xie, *Mater. Horizons*, 2017, **4**, 817–831.

227 K. Zheng, M. I. Setyawati, D. T. Leong and J. Xie, *ACS Nano*, 2017, **11**, 6904–6910.

228 C. Zhang, C. Li, Y. Liu, J. Zhang, C. Bao, S. Liang, Q. Wang, Y. Yang, H. Fu, K. Wang and D. Cui, *Adv. Funct. Mater.*, 2015, **25**, 1314–1325.

229 D. Chen, Z. Luo, N. Li, J. Y. Lee, J. Xie and J. Lu, *Adv. Funct. Mater.*, 2013, **23**, 4324–4331.

230 Y. Li, J. Zhen, Q. Tian, C. Shen, L. Zhang, K. Yang and L. Shang, *J. Colloid Interface Sci.*, 2020, **569**, 235–243.

231 A. Chandrasekar and T. Pradeep, *J. Phys. Chem. C*, 2012, **116**, 14057–14061.

232 Y. Yun, H. Sheng, K. Bao, L. Xu, Y. Zhang, D. Astruc and M. Zhu, *J. Am. Chem. Soc.*, 2020, **142**, 4126–4130.

233 J. Chai, S. Yang, Y. Lv, H. Chong, H. Yu and M. Zhu, *Angew. Chem., Int. Ed.*, 2019, **58**, 15671–15674.

234 J. Zhao, Q. Li, S. Zhuang, Y. Song, D. J. Morris, M. Zhou, Z. Wu, P. Zhang and R. Jin, *J. Phys. Chem. Lett.*, 2018, **9**, 7173–7179.

235 M. Urushizaki, H. Kitazawa, S. Takano, R. Takahata, S. Yamazoe and T. Tsukuda, *J. Phys. Chem. C*, 2015, **119**, 27483–27488.

236 T. Yoskamtorn, S. Yamazoe, R. Takahata, J.-i. Nishigaki, A. Thivasasith, J. Limtrakul and T. Tsukuda, *ACS Catal.*, 2014, **4**, 3696–3700.

237 Z. Li, C. Liu, H. Abroshan, D. R. Kauffman and G. Li, *ACS Catal.*, 2017, **7**, 3368–3374.

238 M. Haruta, T. Kobayashi, H. Sano and N. Yamada, *Chem. Lett.*, 1987, **16**, 405–408.

239 A. Haruta, *Chem. Rec.*, 2003, **3**, 75–87.

240 S. Bhat, R. P. Narayanan, A. Baksi, P. Chakraborty, G. Paramasivam, R. R. J. Methikkalam, A. Nag, G. Natarajan and T. Pradeep, *J. Phys. Chem. C*, 2018, **122**, 19455–19462.

241 Z. Wu, D.-e. Jiang, A. K. P. Mann, D. R. Mullins, Z.-A. Qiao, L. F. Allard, C. Zeng, R. Jin and S. H. Overbury, *J. Am. Chem. Soc.*, 2014, **136**, 6111–6122.

242 Y. Gao, N. Shao, Y. Pei, Z. Chen and X. C. Zeng, *ACS Nano*, 2011, **5**, 7818–7829.

243 X. Nie, H. Qian, Q. Ge, H. Xu and R. Jin, *ACS Nano*, 2012, **6**, 6014–6022.

244 Y. Zhu, H. Qian and R. Jin, *Chem.–Eur. J.*, 2010, **16**, 11455–11462.

245 J. Liu, K. S. Krishna, Y. B. Losovyj, S. Chattopadhyay, N. Lozova, J. T. Miller, J. J. Spivey and C. S. S. R. Kumar, *Chem.–Eur. J.*, 2013, **19**, 10201–10208.

246 S. Lin and Y. Pei, *J. Phys. Chem. C*, 2014, **118**, 20346–20356.

247 J. Chai, H. Chong, S. Wang, S. Yang, M. Wu and M. Zhu, *RSC Adv.*, 2016, **6**, 111399–111405.

248 R. Ouyang and D.-e. Jiang, *ACS Catal.*, 2015, **5**, 6624–6629.

249 G. Li, H. Abroshan, Y. Chen, R. Jin and H. J. Kim, *J. Am. Chem. Soc.*, 2015, **137**, 14295–14304.

250 R. R. Nasaruddin, Q. Yao, T. Chen, M. J. Hülsey, N. Yan and J. Xie, *Nanoscale*, 2018, **10**, 23113–23121.

251 R. R. Nasaruddin, T. Chen, N. Yan and J. Xie, *Coord. Chem. Rev.*, 2018, **368**, 60–79.

252 Y. Zhang, P. Song, T. Chen, X. Liu, T. Chen, Z. Wu, Y. Wang, J. Xie and W. Xu, *Proc. Natl. Acad. Sci.*, 2018, **115**, 10588–10593.

253 G. Li, H. Abroshan, C. Liu, S. Zhuo, Z. Li, Y. Xie, H. J. Kim, N. L. Rosi and R. Jin, *ACS Nano*, 2016, **10**, 7998–8005.

254 H. Abroshan, G. Li, J. Lin, H. J. Kim and R. Jin, *J. Catal.*, 2016, **337**, 72–79.

255 S. Malola and H. Häkkinen, *J. Am. Chem. Soc.*, 2019, **141**, 6006–6012.

256 B. Zhang and T. Bürgi, *J. Phys. Chem. C*, 2016, **120**, 4660–4666.

257 K. Salorinne, S. Malola, O. A. Wong, C. D. Rithner, X. Chen, C. J. Ackerson and H. Häkkinen, *Nat. Commun.*, 2016, **7**, 10401.

258 G. Schmid, R. Pfeil, R. Boese, F. Bandermann, S. Meyer, G. H. M. Calis and J. W. A. van der Velden, *Chem. Ber.*, 1981, **114**, 3634–3642.

259 L. G. AbdulHalim, M. S. Bootharaju, Q. Tang, S. del Gobbo, R. G. AbdulHalim, M. Eddaoudi, D.-e. Jiang and O. M. Bakr, *J. Am. Chem. Soc.*, 2015, **137**, 11970–11975.

260 S.-S. Zhang, L. Feng, R. D. Senanayake, C. M. Aikens, X.-P. Wang, Q.-Q. Zhao, C.-H. Tung and D. Sun, *Chem. Sci.*, 2018, **9**, 1251–1258.

261 S. Takano, S. Hasegawa, M. Suyama and T. Tsukuda, *Acc. Chem. Res.*, 2018, **51**, 3074–3083.

262 S. Takano, S. Ito and T. Tsukuda, *J. Am. Chem. Soc.*, 2019, **141**, 15994–16002.

263 S. Takano, H. Hirai, S. Muramatsu and T. Tsukuda, *J. Am. Chem. Soc.*, 2018, **140**, 12314–12317.

264 Q. Tang, Y. Lee, D.-Y. Li, W. Choi, C. W. Liu, D. Lee and D.-e. Jiang, *J. Am. Chem. Soc.*, 2017, **139**, 9728–9736.

265 Z. Lei, X.-K. Wan, S.-F. Yuan, Z.-J. Guan and Q.-M. Wang, *Acc. Chem. Res.*, 2018, **51**, 2465–2474.

266 X.-S. Han, X. Luan, H.-F. Su, J.-J. Li, S.-F. Yuan, Z. Lei, Y. Pei and Q.-M. Wang, *Angew. Chem., Int. Ed.*, 2020, **59**, 2309–2312.

267 Z.-J. Guan, F. Hu, J.-J. Li, Z.-R. Wen, Y.-M. Lin and Q.-M. Wang, *J. Am. Chem. Soc.*, 2020, **142**, 2995–3001.

268 Y. Wang, X.-K. Wan, L. Ren, H. Su, G. Li, S. Malola, S. Lin, Z. Tang, H. Häkkinen, B. K. Teo, Q.-M. Wang and N. Zheng, *J. Am. Chem. Soc.*, 2016, **138**, 3278–3281.

269 M. R. Narouz, K. M. Osten, P. J. Unsworth, R. W. Y. Man, K. Salorinne, S. Takano, R. Tomihara, S. Kaappa, S. Malola, C.-T. Dinh, J. D. Padmos, K. Ayoo, P. J. Garrett, M. Nambo, J. H. Horton, E. H. Sargent, H. Häkkinen, T. Tsukuda and C. M. Crudden, *Nat. Chem.*, 2019, **11**, 419–425.

270 M. R. Narouz, S. Takano, P. A. Lummis, T. I. Levchenko, A. Nazemi, S. Kaappa, S. Malola, G. Yousefalizadeh, L. A. Calhoun, K. G. Stamplecoskie, H. Häkkinen, T. Tsukuda and C. M. Crudden, *J. Am. Chem. Soc.*, 2019, **141**, 14997–15002.

271 H. Shen, G. Deng, S. Kaappa, T. Tan, Y.-Z. Han, S. Malola, S.-C. Lin, B. K. Teo, H. Häkkinen and N. Zheng, *Angew. Chem., Int. Ed.*, 2019, **58**, 17731–17735.

272 Z. Wang, H.-F. Su, C.-H. Tung, D. Sun and L.-S. Zheng, *Nat. Commun.*, 2018, **9**, 4407.

273 M. J. Alhilaly, R.-W. Huang, R. Naphade, B. Alamer, M. N. Hedhili, A.-H. Emwas, P. Maity, J. Yin, A. Shkurenko, O. F. Mohammed, M. Eddaoudi and O. M. Bakr, *J. Am. Chem. Soc.*, 2019, **141**, 9585–9592.

274 Z. Wang, H.-F. Su, M. Kurmoo, C.-H. Tung, D. Sun and L.-S. Zheng, *Nat. Commun.*, 2018, **9**, 2094.

275 Z.-Y. Wang, M.-Q. Wang, Y.-L. Li, P. Luo, T.-T. Jia, R.-W. Huang, S.-Q. Zang and T. C. W. Mak, *J. Am. Chem. Soc.*, 2018, **140**, 1069–1076.

276 M. A. Boles, M. Engel and D. V. Talapin, *Chem. Rev.*, 2016, **116**, 11220–11289.

277 A. Hernandez-Garcia, D. J. Kraft, F. J. JanssenAnne, H. H. BomansPaul, A. J. M. SommerdijkNico, M. E. Thies-WeesieDominique, M. E. Favretto, R. Brock, F. A. de Wolf, M. W. T. Werten, P. van der Schoot, M. C. Stuart and R. de Vries, *Nat. Nanotechnol.*, 2014, **9**, 698–702.

278 A. Walther and A. H. E. Müller, *Chem. Rev.*, 2013, **113**, 5194–5261.